The importance of what is on the inside: Metastasis from the inside-out and formation of a necrotic core is regulated by a peri-necrotic secreted factor

Ami Yamamoto

A dissertation

submitted in partial fulfillment of the

requirements for the degree of

Doctor of Philosophy

University of Washington

2023

Reading Committee:

Kevin Cheung, Chair

Denise Galloway

Alice Berger

Program Authorized to Offer Degree:

Molecular and Cellular Biology

University of Washington

Abstract

The importance of what is on the inside:
Metastasis from the inside-out and formation of a necrotic core is regulated by a peri-necrotic secreted factor

Ami Yamamoto

Chair of the Supervisory Committee:
Kevin Cheung
Department of Pharmacology

Necrosis in the tumor interior is a common feature of aggressive cancers that is associated with poor clinical prognosis and the development of metastasis. However, how the necrotic core promotes tumor cell dissemination and metastasis remains unclear. Foundational models for cancer metastasis research include mouse, zebrafish, and chick embryo, but identifying tumor cells in transit is painstaking.

In my thesis work, I used a rat model of breast cancer metastasis to increase detection of dissemination events. Owing to the large size and higher blood volume of rats, I collected 10 times more circulating tumor cells (CTCs) than from mice. In this model, tumor dissemination was temporally correlated with the emergence of necrosis in the tumor interior. These findings were corroborated by longitudinal study of CTC

abundance and tissue necrosis markers in blood plasma from patients with metastatic breast cancer. Further, I observed that dilated blood vessels were located next to necrotic regions of the tumor and that their increase was concurrent with the initiation of intratumoral necrosis and increase in CTC abundance.

Bulk RNA sequencing of mouse-to-rat xenograft tumor necrotic core compared to the non-necrotic rim revealed distinct tumor-specific and host-specific transcripts in the necrotic interior. We identified angiopoietin-like 7 (Angptl7) as a tumor-specific factor localized to the peri-necrotic zone. Functional studies showed that Angptl7 loss normalizes central necrosis, decreases peri-necrotic dilated vessels, reduces metastasis, and reduces circulating tumor cell counts to nearly zero.

Taken together, these findings show that breast tumors actively produce factors controlling central necrosis formation and metastatic dissemination from the tumor core. Tumor dissemination events are localized spatially to dilated peri-necrotic vessels in the tumor interior, and tumor dissemination is dependent functionally on the expression of a factor, Angptl7, produced by peri-necrotic tumor cells. These findings provide strong evidence that the factors in the peri-necrotic zone in the center of the tumor regulate tumor cell dissemination and suggest that tumor dissemination originates from the tumor core. My thesis work informs a new perspective on the mechanism of tumor dissemination and reveal a potential therapeutic target to directly disrupt it.

TABLE OF CONTENTS

LIST OF FIGURES

LIST OF TABLES

Chapter 1 Table:

ACKNOWLEDGEMENTS

To the Cheung Lab. First, I want to thank my advisor, Kevin Cheung, for his mentorship and partnership for my dissertation work and beyond. I am thankful for and will always remember our scientific dialogues and your enthusiasm for science. I also want to thank the entire Cheung Lab including former lab members for the great scientific conversations, partnerships, and everything you all have taught me. I especially want to thank Andie Doak for being my grad student buddy in the lab, being such a kind and fun friend and for her constant moral support. I also want to thank Sarah Huang for all of her help in this dissertation work as well as her compassion and friendship through it all. Your scientific rigor bettered my dissertation work, and your sweetness melted my heart even in the toughest of times. I also want to thank Brad Krajina for all of his scientific help and advice and for always being a shoulder I can lean on. Your presence, kindness, humor, and scientific intellect & rigor has made the past three years in the lab so much brighter and more colorful.

To my thesis advisory committee. I would like to thank my committee members, Alice Berger, Barry Gumbiner, Cecilia Moens, Dave Raible, Denise Galloway for all of the advice, feedback, and encouragement they've given me during my time as a graduate student. Thank you so much for being my supporters in and outside of committee meetings.

To my collaborators. A huge thank you to all of the collaborators I've had over the years who added so much value to my dissertation work. It was such a pleasure to work with you, and I appreciated all of the advice and input you provided. I especially want to thank Michael Haffner for his pathology expertise and thoughtful input.

To the MCB program & Fred Hutch Office of Graduate Education. Thank you so much to the MCB program directors and staff as well as the Fred Hutch Office of Graduate Education for the wonderful support you provided over the years. A special thank you to Maia Low for being a warm, safe presence for MCB students to lean on. A huge thank you to Andrea Brocato for being an amazing ally and confidant and for all of the support you've provided me over the years.

To my friends. I want to give a very special thank you to all of my friends who have supported me from close and from afar during my PhD. You all have been my biggest emotional support, and I absolutely could have not done this without you all. I want to thank my friends Eileen Brister, Hersha Guron, and Nick Dalman for supporting me from afar and for their longtime friendship. I want to thank my Seattle friends for being there for me through it all. I want to thank give a special shoutout and thank you to my roommates over the years, my pandemic bubble, and my best friends who experienced me through my best and worst; thank you Maddy Hewitt, Vanessa Montoya, Alyssa Brokaw, Brad Krajina, Amy Spens, Eric Thomas (ET), and Lews Caro for putting up with me, supporting me, and being such wonderful and warm friends. I love and appreciate you all so much. Thank you to Ralph the yeti, Churro the elephant, Cinnamon the dragon, Kiwi the snake, Gus the penguin, Ruby the penguin, Porter the frog, and Honey the bear, for emotional support and cuddles.

To my Hutch United colleagues. A very warm thank you to my Hutch United colleagues. It has been wonderful to work with you over the years on important work to make science and the Hutch a place where everyone can feel they belong. Hutch United gave me such a wonderful sense of community. You have no idea what a huge part of my emotional support system you all have been.

To my family. Last but not least, big thank you to my family for supporting me, not only through my time in graduate school, but also throughout my entire life. I feel so lucky to be a part of this wonderful family and receive so much support from you all. Thank you to my mom for being a warm, safe place I can always come home to, for the long phone calls, and for cooking me my favorite foods when I am back home. Thank you to my dad for being my number one fan and supporter throughout my entire life and especially during grad school. Thank you to my brother, Kenta Yamamoto, for all of his love and support. You're the very best brother I could have ever hoped for. I love and appreciate you so much.

Chapter 1. INTRODUCTION: COLLECTIVE METASTASIS BY TUMOR CELL CLUSTERS

Metastatic dissemination has lethal consequences for cancer patients. Accruing evidence supports the hypothesis that tumor cells can metastasize as clusters of cells while maintaining contacts with one another[1–3]. Collective metastasis enables tumor cells to colonize secondary sites more efficiently, resist cell death, and evade the immune system. On the other hand, tumor cell clusters face unique challenges for dissemination particularly during systemic dissemination. Here, we review recent progress toward understanding how tumor cell clusters overcome these disadvantages as well as mechanisms they utilize to gain advantages throughout the metastatic process. We consider useful models for studying collective metastasis and reflect on how the study of collective metastasis suggests new opportunities for eradicating and preventing metastatic disease.

1.1 INTRODUCTION

Metastasis, the process by which cancer cells disseminate and colonize distant organs, is responsible for the majority of the estimated 9.9 million cancer-associated deaths occurring worldwide every year[4,5]. This complex process involves the orchestration of sequential steps that must all be completed successfully for metastasis to emerge. Tumor cells must detach from the primary tumor and disseminate to a secondary site, in many cases far from the initial site of cancer. Thereafter, disseminated tumor cells (DTCs) must rapidly adapt to a newfound, often hostile, environment. Perhaps most difficult of all, upon arrival, tumor cells must construct a more favorable metastatic niche to survive and

ultimately proliferate. Partly due to heterogeneity in timeline, mechanism, and pattern of spread, metastasis remains a challenge to treat clinically and to study biologically.

Metastatic dissemination has often been thought to be primarily completed by cells traveling alone[1–3]. This is premised on observations that tumor cells become more migratory when they lose cell–cell attachment, that tumor cells in circulation are mostly single cells, and that single DTCs can be found throughout a cancer patient's organs. However, there is evidence that tumor cells can metastasize cohesively as a clump, embolus, or cluster of tumor cells rather than as single cells. In the 1970s, studies independently demonstrated that tumor cell clumps have greater metastatic seeding potential compared with single tumor cells[6,7]. Meanwhile, observations in a host of developmental and cancerous states have firmly established that cells can capably migrate while maintaining cell contacts during morphogenesis and cancer invasion[8]. It has become increasingly clear that tumor cell clusters are found in cancer patients' bloodstreams (and bone marrow) in multiple cancer types and that the presence of circulating tumor cell (CTC) clusters is associated with worse prognosis[9–14]. These studies and others have provided clues to a mode of collective metastasis in which groups of tumor cells execute the metastatic process as clusters of cells.

In this review, we discuss the recent progress toward understanding the molecular mechanisms of collective metastasis and its consequences. We first highlight the weight of clinical and experimental evidence supporting collective metastatic seeding. We discuss the emerging evidence for diverse intercellular interactions within tumor cell clusters, endowing cancer cells with enhanced metastatic aggression. At the same time, clusters may also face unique disadvantages at early steps in metastasis, particularly

while navigating systemic circulation. We highlight how different models have supported collective metastasis research and identify avenues for future technological development. While collective metastasis remains a field in its early stages, we propose that understanding how collectivity arises and how it changes tumor cell behavior during metastasis is essential in the quest to prevent and eradicate metastatic disease.

1.2 EVIDENCE FOR COLLECTIVE METASTASIS

For the purposes of this review, we define collective metastatic seeding as the completion of dissemination, seeding, and outgrowth phases of metastasis by a cluster of at least two tumor cells. As discussed below, there is strong evidence that tumor cell clusters can be found in cancer patient blood and that their presence is associated with worse prognosis. These clusters, despite their low frequency compared with single tumor cells, make large contributions to productive metastases.

1.2.1 *Circulating tumor cell clusters are detected in many cancers, and their presence is associated with poorer patient outcomes*

The ability to isolate and characterize circulating tumor cells provides a window into the properties of disseminating tumor cells in transit. Because blood draws are relatively noninvasive and frequently obtained from cancer patients, CTCs are promising for monitoring therapy response and disease evolution, as reviewed extensively elsewhere[15]. Although studies of CTC abundance vary by tumor type, tumor stage, blood collection site, and isolation strategy, a common conclusion is that the presence of CTCs correlates

with worse progression-free survival (PFS) and overall survival (OS) in most common human cancers[16,17].

Table 1. Percentage of Patients with Single CTCs and CTC Clusters

Citation	Cancer type	% Patients with single CTCs	% Patients with CTC clusters	Number of patients
Jansson et al. 2016[18]	Breast**	NR	27%	52
Wang et al. 2017[11]	Breast**	60.2%	16.4%	128
Larsson et al. 2018[13]	Breast*	52%	20%	156
Paoletti et al. 2019[19]	Breast*	52%	19%	266
Costa et al. 2020[20]	Breast*	57.4	25.9	54
Divella et al. 2014[21]	Colorectal	67%	32%	103
Zheng et al. 2017[22]	Gastric*	43%	26%	81
Hou et al. 2012[9]	Lung (SCLC)*	85%	32%	97
Long et al. 2016[10]	Melanoma*	51%	34%	128
Lee et al. 2017[23]	Ovarian	98.1%	59.2%	54
Chang et al. 2016[24]	PDAC*	81%	81%	19
Okegawa et al. 2018[25]	Prostate*	NR	50%	98
Mu et al. 2015[12]	Breast**	31.30%	17.40%	115
Carlsson 2017[14]	Prostate*	Blood: 33%	NR	141
		Bone Marrow: 23%	NR	

*Baseline analysis of CTC cluster presence

**Longitudinal time-dependent analysis of CTC cluster presence

Beyond individual CTCs, newer technologies and analytical methods have identified CTC clusters in many metastatic cancer types[26–29]. These assays have defined CTC clusters as a group of two or more cohesive cells. Such CTC clusters are consistently rarer than single CTCs. Among studies investigating both single CTCs and CTC clusters, between 1% and 10% of CTC events are clusters[14]. Between 43% and 98% of patients with metastatic disease have detectable single CTCs in their bloodstream, with detection most commonly defined as >5 CTCs per blood draw (see Table 1). In comparison, the same studies found one or more CTC clusters per blood draw in 16–59% of patients (see Table 1). While most of these studies have focused on patients with advanced-stage disease, there is also clinical evidence that CTC clusters can be detected in early-stage cancers, prior to or during definitive surgical resection[30–32].

Patients with CTC clusters detected in their bloodstream have significantly poorer PFS and OS compared with patients with only single CTCs[9–13]. Hazard ratio (HR) is a common way to quantify the difference in risk between groups. For example, if the HR of death is 2.0, this means the rate of death is twice as high in one group than the other. In available studies, the HR for OS for patients with CTC clusters compared with patients with only single CTCs ranged from 2.9–15.1[9,11–13]. However, two limitations should be acknowledged when interpreting these studies. First, CTC clusters tend to occur in patients with the most CTCs, as reflected in one large reanalysis of prospectively collected CTCs using CellSearch in metastatic breast cancer patients[19]. In comparisons between patients with high single CTC counts, the presence of CTC clusters is no longer

independently prognostic. This could indicate that CTC clusters may simply be an indicator of high CTC abundance. Whether underlying cellular biological processes driving CTC and CTC cluster dissemination are shared remains to be tested. Second, the entry point of enrollment for many studies is not uniform. The frequency of CTC clusters varies with disease progression and is most abundant in patients with treatment-resistant and refractory cancers[11,12,19,33]. Whether CTC clusters are a cause or consequence of therapy resistance is incompletely understood, though one recent study has suggested that resistance to endocrine therapy shifts metastatic breast cancer cells toward a clustered phenotype[34]. Despite our incomplete understanding of why CTCs correlate with poor patient outcomes, the presence of CTC clusters can be confidently interpreted as a poor prognostic factor.

At present, the true frequency of CTC clusters remains uncertain, and the optimal approach toward identifying CTC clusters is not yet understood (discussed in the next section). For now, we point out that relying on different qualifications and cell surface markers to define CTCs inherently means that the definitions of CTC clusters vary by study. In addition, it is difficult to tell if CTC clusters are being undersampled because they are breaking apart or becoming trapped during the CTC isolation process. CTC clusters could also be rendered invisible to detection through filtration in a more proximal capillary bed. CTC abundance also varies dynamically and can vary on a circadian level[35]. The ability of CTC clusters to remain intact during isolation is dependent on many factors including the shear stress experienced by CTC clusters during the isolation process. In recent years, various technologies have been designed specifically to maintain and recover clusters from the blood[27,36]. The importance of CTC cluster size (how many cells

are in a CTC cluster) also remains understudied. One label-free technology designed to isolate CTC clusters found that 30–40% of patients with metastatic breast cancer, prostate cancer, or melanoma had CTC clusters and that CTC cluster size ranged from 2 to 19 cells. CTC cluster cell count trended toward exponential distribution, with many more 2-cell clusters than larger clusters[27]. A few studies have suggested that larger CTC cluster sizes could provide advantages beyond 2-cell clusters[11]. In one study of metastatic breast cancer patients, authors found that the OS HR is 14.5 for patients with clusters containing at least 3 cells compared with patients with no CTCs, whereas the OS HR is 7.96 for patients with clusters with 2-cell clusters. Whether larger CTC clusters correlate with worse prognosis will require larger well-powered studies using technologies designed to capture clusters.

1.2.2 *Challenges in circulating tumor cell cluster detection and isolation*

CTCs are rare, dynamic, short-lived entities that occur at frequencies of <1 CTC per 10 million leukocytes and 100 million red blood cells[37]. This makes the enrichment, isolation, and detection of CTCs extremely challenging. At present, only one CTC detection method, CellSearch, is FDA-approved to detect CTCs in breast, prostate,
and colorectal cancer patients to help determine prognosis[15]. CellSearch is one of many surface marker–based methods that relies on the expression of EpCAM to detect CTCs. A known limitation of EpCAM-based detection is its inability to detect CTCs that do not express EpCAM. An extension of this problem germane to CTC clusters is that tumor cells show heterogeneous expression for different markers[10,38]. Further, CTC clusters can occur in complexes with immune cells such as neutrophils[39], which can interfere with CTC cluster isolation by affinity-based methods such as negative depletion of CD45+ immune

cells. One approach that may overcome these challenges is use of label-free methods that select for CTCs and clusters based on size and deformability. Microfluidic devices enable the recovery of heterogeneous CTC populations including clusters and do not rely on surface markers such as EpCAM[27,36,40,41]. The fact that most CTC clusters are doublets and therefore may have size characteristics not much different from single CTCs is a challenge in these methods. Further, microfluidic devices that enforce certain channel size dimensions or impose critical flow rates may induce shearing that disaggregates CTC clusters. Perhaps the simplest approach is red blood cell lysis followed by affixing residual cellular fraction to slides and staining these slides for markers such as cytokeratin and CD45 that can be analyzed by microscopy. This method, however, makes it more difficult to process CTCs for downstream analyses or cultivation[42]. At present, it remains a fundamental challenge that CTC technologies are developed and optimized using simulated CTCs generated via spike-ins of human cancer cells into blood samples. These technologies are then tested in human patient populations where the true properties of CTCs are unknown and depend on tumor type, disease stage, and follow-up time. Such complications make it difficult to determine the most efficient, catchall, unbiased CTC detection and isolation methods. Mouse and other patient-derived xenograft animal models that spontaneously and reproducibly generate CTCs could be valuable for these efforts, but CTCs in these models are even more rare and short-lived due to their small circulating blood volume. Better models that allow for sampling and analysis of large numbers of CTCs collected in an unbiased manner could be pivotal to gain a deeper understanding of CTC and CTC cluster characteristics and variations.

1.2.3 *The outsized potential of tumor cell clusters for metastatic seeding*

Early CTC cluster studies in the 1970s reported that when tumor cells were separated into clusters or single tumor cells and injected intravenously into mice, tumor cell clusters produced between 3- and 25-fold greater lung metastases[7,43].More recent studies have shown similar effects with between a 2- and 500-fold increase in metastasis formation using a variety of cancer models (breast, melanoma, and colon) and delivery routes (intravenous, intracardiac, intraperitoneal, and retroorbital) [2,28,44–49].

These experimental metastasis models support the notion that tumor cell clusters have robust metastatic potential. However, because CTC clusters are rare in patients and in mouse models, it is possible that individual CTCs nonetheless contribute to the majority of metastatic seeding. How then, can we determine the contribution of multicellular seeding? One experimental approach that has proven useful is lineage tracing with multicolor fluorescent labeling of tumor cells in animal models of metastasis including mice, zebrafish, and fruit flies[28,48,50–59]. In these experiments, multicolor primary tumors are generated by transplanting tumor cells into a tissue of origin or through genetic models of metastatic cancer. These primary tumors are composed of two or more tumor clones expressing different fluorescent reporters that are maintained through division. Metastases develop over time and are then examined by microscopy. If metastases arise exclusively from individual clones, then only single-color metastases would be expected. If metastases are multicolored, then at some point in their development they arose from two or more distinct clones. Using this approach, multiple groups have reported that the majority, in some cases more than 90%, of metastatic seeding events are polyclonal. The multicolor labeling approach can be further extended by increasing the number of colors

or by using genomic barcoding[44,53–55,57]. A limitation of these methods at present is the unequal proportion of different clones in primary tumors, a factor that tends to decrease overall clonal diversity and hence the power to detect multicolor metastases. Nonetheless, these studies suggest that only a small number of clones, most commonly two, contribute to polyclonal seeds. Another limitation of using a color mixing approach to lineage tracing is that it cannot rule out the cross-seeding of metastases. For example, it cannot rule out cells traveling between different metastases after each metastasis is seeded by a single cell. However, new barcode lineage tracing and CRISPR-based methods can overcome these limitations and have already started to shed light on new information regarding the lineage of metastases[60,61]. For example, ClonTracer studies have shown most therapy resistant clones are part of small, pre-existing subpopulations which selectively escaped under therapy[60].

1.3 Mechanisms by which tumor cell clustering promotes metastatic seeding

1.3.1 *Benefits of clustering during metastatic seeding and outgrowth*

Tumor cells in circulation are bombarded by multiple insults that act as barriers to survival and metastasis formation[62,63]. These include mechanical insults such as fluid shear stress (FSS), which can shred tumor cells in high-flow vessels. During circulation, some tumor cell clusters experience loss of cell–cell and cell–matrix attachments necessary for tumor cell survival, leading to anoikis and metabolic rewiring[64,65]. Clusters in circulation are also exposed to oxidative stress, which can lead to ferroptosis and other death pathways[66,67]. Further, clusters are vulnerable to immune attack in circulation or immediately thereafter when lodged in the distant organ[54,68,69]. A tumor cell that is able to complete all these

steps is therefore highly unlikely. Emerging studies indicate that tumor cell clusters potently change these odds.

Resisting fluid shear stress.

FSS, induced by liquid flow, is defined as the internal frictional force between moving layers in laminar flow[62]. CTCs experience FSS in transit, of which the magnitude and duration of exposure can affect the chances of CTC survival. CTCs subjected to high FSS can induce mechanical stress, cell fragmentation, and death, while CTC clusters are more resilient to mechanical forces[70–72]. This resilience occurs not only as a function of superior physical integrity through cell–cell adhesion but also because traveling as clusters increases drag force, decreases the speed of CTCs traveling as clusters, and promotes their intravascular arrest[62,70].

Resisting cell–cell and cell–matrix detachment–induced cell death.

Attachment to the extracellular matrix (ECM) is important for cell survival, and upon loss of anchorage to the ECM, cells undergo a form of programmed cell death called anoikis[63]. The formation of tumor cell clusters rescues tumor cells from anoikis through maintenance of cell–cell attachment. Cell– cell attachment can protect cells from additional stressors encountered in circulation via signaling pathways. These include nectin-1/nectin-4 binding in adjacent tumor cells, which drives integrin β4/SHP-2/c-Src activation[67], E-cadherin-dependent reactive oxygen species protection[73], and DNA methylation to induce stemness transcription factors[74]. These studies support a potential for development of therapies that break apart tumor cell clusters to mitigate their metastatic advantages.

Avoiding immune attack.

There is still much that is unknown about CTC avoidance of immune modulation, especially whether there are differences between single cells and clusters. However, there is evidence of CTC cluster-specific mechanisms to avoid immune surveillance from natural killer (NK) cells. Infiltration of NK cells into tumors and high expression of NK cell receptor genes are correlated with better patient prognosis, indicating that NK cells can target tumor cells[75]. Lo et al.[54] recently found that selectively depleting NK cells increased monoclonal but not polyclonal metastases, suggesting that NK cells can effectively kill single tumor cells but not clusters. Tumor cell clusters were revealed to have increased expression of cell–cell adhesion and epithelial genes and decreased expression of NKcell–activating ligand. These studies hint at an existence of cluster-specific immune evasion mechanisms, potentially conferring tumor cell clusters an advantage throughout the metastatic process. There is also increased interest in NK cell
therapy for cancer patients with advanced disease, in which NK cells' ability to kill CTCs and DTCs is exploited for therapy[69,76]. Gaining a deeper understanding of cluster-specific avoidance of NK cell killing could be key to developing such therapies to target tumor cells while in circulation.

Increased metastatic outgrowth.

As stated above, there is a wealth of evidence that circulating clusters are more likely than single cells to seed metastatic lesions that grow out quickly[2]. This concept is mirrored in some 3Dculture models, where PyMT tumor cell clusters survive longer and proliferate

up to five times more quickly than single cells, an effect that increases with the number of cells in the cluster[49]. Several studies have revealed that clusters have several advantages over single cells that have arrived in the distant organ, including increased stemness and

intercellular signaling that stimulates tumor outgrowth, and cooperative polyclonal interactions.

One such signaling mechanism has been described in which minor subclones of breast cancer cells expressing IL11 and FIGF signal to one another as well as stromal and immune cells to promote metastasis[77]. In another case, integrin–ECM adhesion mechanisms were utilized by subclones to increase proliferation. MCF10A PIK3CA mutant subclones upregulate fibronectin, promoting growth of Her2 mutant subclones. Inhibition of integrin–fibronectin binding reduces the proliferative benefits of growing the two clones together[78].

Recently, our lab has found that when breast cancer cells travel throughout the body together as clusters of cells, instead of as individual cells, they are >100 times more likely to form metastases. In this work, we found that one reason tumor cells metastasize better together is because breast cancer cells adhere to one another and form intercellular spaces between their cell–cell adhesions, which we termed nanolumina. We found that these nanolumina act as shared reservoirs for the growth factor epigen. Blocking tumor cell clusters from expressing and sharing epigen greatly reduced their growth in vitro and in vivo, suggesting that nanolumina and the cell–cell signaling they generate play a key role during metastatic outgrowth[49]. In addition, a recent study showed that a single clone isolated from an ovarian tumor sample was the primary population in

metastases. However, when injected alone, this clone was incapable of forming metastatic lesions. It was uncovered that this clone expressed high levels of Her2 and was only able to seed metastases in the presence of a clone expressing high levels of AREG or when exposed to exogenous AREG[79]. Together these studies implicate a role for collective family signaling in tumor seeding and metastatic outgrowth.

Consistent with the model of cooperation between tumor cell clones, other studies also have found scenarios where less-fit subclones can metastasize with more-fit metastatic clusters to form distant polyclonal metastases. For example, in colorectal carcinoma cells, more aggressive metastatic cells traveled with and enabled the seeding of less-fit metastatic cells by priming the niche via fibrosis[59]. Similarly, a melanoma cell line clone that is highly invasive and capable of metastasis can adhere to a more proliferative clone, delivering it to the metastatic site and increasing growth potential[56].

1.3.2 *Composition of tumor cell clusters during metastasis*

There has been significant interest in defining various cell adhesion complexes coupling tumor cells together, enabling cluster-driven metastasis. In addition, there is growing recognition that clusters are composed of phenotypically, and in some cases genotypically, distinct cell types (Figure 1). Understanding how these cells each contribute to collective metastases can uncover mechanisms behind metastatic survival and outgrowth.

Cell-cell adhesion.

The types of cell adhesion complexes present in tumor cell clusters vary by tumor type. The most common cancers are epithelial in origin and accordingly contain adherens junctions, desmosomes, and tight junctions, all vital for maintaining cell–cell contact[8]. In some cases, tumor types such as melanoma can be reliant on adhesion complexes of other types such as neural cell adhesion molecules. Given the rarity of CTC clusters, a systematic understanding of the adhesion complexes most important for CTC cluster integrity and metastasis is necessary.

Nonetheless, a number of studies suggests several common themes important to highlight. The first is that multiple studies in epithelial tumors have implicated the metastasis-promoting role of various components of desmosomes, which strongly anchor cell–cell contacts. Loss of junction plakoglobin, a key intracellular component of the desmosome, reduces CTC clustering and metastatic potential (17). Likewise, expression of desmogleins, desmocollins, and plakophilins (such as DSG1, DSC2, and PKP1) has been shown to support clustering and metastasis formation[72,80]. It therefore stands to reason that desmosomal targeting could have profound effects on CTC cluster integrity and likely on the integrity of micrometastases in distant organs. In addition, disruption of desmosome adhesion could alter the frequency and type of tumor dissemination. For example, in one breast cancer mouse model, loss of DSG2 enhanced single-cell CTC dissemination while its reexpression induced more CTC clusters[80].

The expression of various cell adhesion molecules not only supports clustering but also induces downstream signaling that can affect the survival and outgrowth of tumor cells. E-cadherin contacts are critical for adherens junction formation and play important structural and signaling roles in migrating tumor collectives. Accordingly, constitutive loss

of E-cadherin is accompanied by marked reductions in metastasis formation[73,81]. Nectin-1 (PVRL-1) and nectin-4 (PVRL-4) binding between adjacent tumor cells is a potent inducer of anchorage-independent survival and growth, driving ECM-independent integrin β4/SHP-2/c-Src activation to prevent apoptosis[82]. There is further evidence that α6β4 integrin signaling activation and subsequent GPX4 expression prevents lipid peroxidation and ferroptosis[67].

Cell adhesion confers an additional advantage to tumor cells by reducing the distance needed for productive intercellular communication. Tumor cells can communicate by passing signaling molecules to neighboring cells via gap junctions at cell–cell contacts. Connexins, a major component of gap junctions, have been implicated in many aspects of metastasis, although the specifics of intercellular signaling via gap junctions during collective metastasis need further investigation[83]. In addition, the physical binding of tumor cells to one another can induce intercellular spaces that act as sites of collective intercellular signaling[49]. As described above, breast tumor cell clusters secrete and concentrate growth factor into the spaces, such that, regardless of the microenvironment these clusters find themselves in, collective signaling can be maintained, encouraging survival and growth at the metastatic site[49]. In some cases, the signaling molecules between cells are packaged into exosomes[84] or passed between cells via cytoplasmic transfer[85].

There is evidence that cell adhesion gene expression can be modified under selective pressure. For example, in vitro selection of tumor cells resistant to FSS in a microfluidic system led to a highly metastatic population with increased clustering and expression of desmosomal genes[72]. Likewise, isolation of DTCs in a mouse model of

head and neck squamous cell carcinoma identified clones with enhanced fitness that preferentially generated clusters resistant to anoikis when placed under FSS[86]. In another example, estrogen receptor–positive breast cancers can develop resistance to endocrine therapy via genomic alterations in the estrogen receptor gene ESR1. ESR1-mutant breast cancer cells show increased expression of adhesion genes as well as enhanced clustering and metastasis[34]. More work is needed to understand whether selective pressure during metastatic seeding or during cancer treatment drives the selection for tumor cells with clustering behavior.

Heterogeneous tumor cell populations.

Tumor dissemination is a critical bottleneck that acutely restricts the diversity of tumor cell populations. In the collective cell metastasis, cells maintain the advantage of heterogeneity during invasion, in circulation, and in the metastatic niche. Once growing in the metastatic niche, these cells often give rise to diverse lineages to ensure survival[55,87]. Identification of polyclonal metastases in a variety of experimental models and clinical genomic studies supports the theory that tumor cell clusters are a vehicle for metastasis. Such phenotypic and genotypic heterogeneity is an undoubted contributor to tumor growth and therapy resistance, posing a significant challenge in the clinic (85).

Supportive of this concept, circulating clusters of melanoma tumor cells have variable expression profiles that mark INV (invasive) and PRO (proliferative) clones, which, as described in detail below, exhibit high metastatic behavior in a multiclonal fashion[56]. In another example, metastatic breast cancer CTCs have been shown to express both epithelial and mesenchymal RNAs in situ, indicating that clusters could be

composed of tumor cells varying along the epithelial-to-mesenchymal transition (EMT) spectrum[88]. In these cases, cells within clusters need not commit to a single state and may benefit from all stages of the EMT spectrum. Despite the presence of heterogeneous populations, many cells in CTC clusters show evidence of methylation patterns consistent with increased stem cell factors[74]. In different tumor models, metastasis-initiating cells give rise to metastatic tumors that may share properties with more stem-like or regenerative cell populations[5]. It remains unresolved whether tumor cells in clusters rely more on hybrid EMT or cooperation between epithelial and mesenchymal cells for successful metastasis.

In a more complex example, two breast cancer tumor cell clones expressing either IL11 or FIGF (VEGFD) cooperate with neutrophils to drive polyclonal metastasis. When IL11- and FIGF-expressing cells make up 10% of a primary tumor, metastases increase significantly. These cells signal to stromal cells and neutrophils to increase metastasis, an effect that is lost when neutrophils are depleted[77]. As mentioned above, ovarian tumor cell clones expressing high levels of Her2 (ERBB2) cooperate with another clone that expresses high levels of AREG during metastasis[79]. These reports suggest that heterotypic tumor cell clusters are poised to take advantage of intercellular cooperation to promote seeding and metastasis.

Nontumor cells.

Beyond tumor–tumor cell interactions, tumor cell clusters can be found in association with various stromal cells, immune cells, and blood cell components. When in concert with tumor cells, neutrophils instigate metastasis in a variety of contexts. In one report,

Szczerba et al.[39] showed that while 88% of breast cancer patient CTCs were single cells, 8.5% were homotypic clusters and 3.4% were heterotypic white blood cell (WBC)–CTC clusters. Within the WBC–CTC clusters, roughly 85–91% of WBCs were neutrophils. Neutrophil-associated CTC clusters exhibited high expression of cell-cycle genes and efficient metastasis formation. Detection of neutrophil–CTC clusters was also associated with poor prognosis in metastatic breast cancer patients when compared with patients without these clusters[39,89]. Functional screens identified that VCAM1 mediates neutrophil–CTC interactions and that VCAM1 inhibition prevents neutrophil–CTC cluster formation. This discovery suggests a potential therapy to prevent metastatically efficient neutrophil–CTC cluster formation without depleting non-CTC-associated neutrophils. Other myeloid-derived immune cells such as myeloid-derived suppressor cells (MDSCs) are known to promote neoplastic growth by inhibiting T cell activity and to form clusters with tumor cells in circulation[90]. Like neutrophils, MDSCs
can directly interact with CTCs and promote their dissemination and metastatic potential.

Tumor cell clusters can also be found in association with stromal elements from the primary tumor. There is evidence that the viability of CTCs is higher when they cotravel with cancer-associated fibroblasts (CAFs) as heterotypic clusters[91,92]. Tumor cell clusters in association with CAFs promote early metastatic outgrowth at the secondary site[91]. These findings indicate that tumor cells can bring their own “soil” from the primary tumor with them to secondary sites of metastasis. More work is needed to determine the comparative frequency of this mechanism in tumor cell clusters compared with other modes such as reprogramming the distant tissue microenvironment.

Finally, CTC–platelet clusters promote metastasis in several ways[63,93,94]. Labelle et al.[93] determined that platelets protect CTCs from FSS during circulation by using a viscometer to subject CTCs to prolonged periods of shear stress, modeling in vivo circulation. Egan et al.[95] similarly determined that platelets can provide protection against FSS in experiments using A2780 cells with lactate dehydrogenase release as a proxy to measure membrane damage. Platelets also grant CTCs resistance to anoikis[94]. Ovarian and colorectal cancer cells cultured under anoikis conditions exhibited reduced anoikis when cocultured with platelets in a YAP1-dependent manner, and treatment of tumor-harboring mice with antiplatelet antibody increased tumor cell death[94]. Similar to other immune and stromal cells, platelets can induce epithelial-mesenchymal-like transition in tumor cells[93]. Platelet-tumor contact and transforming growth factor beta (TGFβ) signaling from platelets activate TGFβ/Smad and NF-κB pathways in colon and breast cancer cells. Platelet activation in turn can induce signaling changes by releasing TGFβ[93], ATP[96], or chemokines to induce EMT, transendothelial migration, and recruitment of granulocytes,monocytes, and macrophages (96). This results in an EMT-like transition to an invasive and mesenchymal-like phenotype, increasing metastatic efficiency[93]. A challenge to studying the specifics of CTC–platelet cluster function in circulation, such as the adhesion mechanism, is that platelets cover CTCs so well that they mask these stealth CTCs from being detected by many traditional methods[97]. Despite these limitations, in totality these studies suggest that coagulation activation of platelets generates a protective barrier against FSS and immune surveillance, inducingmetastatic spread and outgrowth through tumor cell signaling and plasticity.

1.4 MECHANISMS OF COLLECTIVE TUMOR CELL DISSEMINATION

Many central questions in collective metastasis revolve around how tumor cell clusters migrate and disseminate into the blood and lymphatic vasculature. Intuitively, this process involves the loss of cell–cell adhesion contacts and gain of cellular motility, as commonly observed in single cell metastasis. Here, however, some cell–cell adhesions are maintained. The migration of clusters introduces new behavioral capabilities but also introduces new challenges faced by tumor cells when orchestrating multicellular motility. As discussed below, a variety of modes have been identified by which tumor cell clusters accomplish intravasation into blood vessels.

1.4.1 *How does a tumor cell cluster dissemination into the vasculature?*

Although both single CTCs and CTC clusters have been found in circulation, it is not yet well understood where, when, and how tumor cells enter blood or lymphatic vessels[98]. In the traditional linear cascade model of metastasis, intravasation is depicted as a step in the metastatic cascade that occurs after local invasion at tumor–stromal borders[4]. However, tumor vessels vary in diameter and permeability, which are both features that could contribute to the success rate of tumor cell dissemination. Corrosion casting of tumor vasculature has shown that blood vessels become more aberrant and less organized as they get close to the core of the tumor[99]. This lack of organization may arise due to rapidly and irregularly formed vessels, resulting in leaky tumor vasculature with impaired barrier function and little lymphatic drainage[98]. Tumor cells may take advantage of vessels with compromised integrity to gain access to circulation[100]. In the mouse mammary tumor MCH66 model, blood vessels have been theorized to engulf nests of tumor cells, instigating metastasis without invasion[101]. Alternatively, gaps in the

endothelial lining, called mosaic vessels, may directly expose tumor cells to vessel flow[98]. One study showed that tumor vasculature may be up to 15% mosaic[102]. Recently, Silvestri and colleagues[103] developed a microvessel coculture model, which demonstrated that breast tumor organoids integrate into the endothelial cell lining and can intravasate as clusters. These findings suggest parallel processes and mechanisms that extend beyond the linear cascade sequence of metastasis. For example, in a chick chorioallantoic membrane mesoderm model, Deryugina & Kiosses[104] showed that intravasation can begin early in tumor progression and proceed in parallel with local stromal invasion. Interestingly, they also showed that most intravasation events occur in the interior region of the primary tumor, not the tumor–stromal border. Likewise, breast tumor xenograft models demonstrate the existence of hypoxic cores that induce intravasation of CTC clusters that were largely hypoxic, whereas individual CTCs were largely normoxic[105]. The development of more realistic and robust models to study tumor cell cluster intravasation events, which are very rare, is needed to better define the mechanisms by which tumor cell clusters into the circulation.

Another possibility is that tumor cells disseminate individually and then aggregate within the local circulation before being detected as CTC clusters. Consistent with this possibility, different breast cancer models have supported early dissemination of individual cancer cells of the Her2+ subtype and implicated involvement of TEK receptor tyrosine kinase (Tie2+) macrophages[106,107]. In these cases, Tie2-high, vascular endothelial growth factor A (VEGFA)-high macrophages induce transient vascular permeability, invadopodia formation, and intravasation of actin-regulatory protein mammalian-enabled (MENA)-high tumor cells into adjacent endothelial cells[108,109].

Furthermore, recent studies have suggested that tumor cells that have undergone intravasation subsequently aggregate in blood vessels via CD44-dependent homophilic adhesion to seed metastasis as polyclonal clusters[48]. It seems likely that the relative proportion of seeding events that are cohesive versus due to aggregation will depend on the local density and spatial proximity of tumor cells, which in turn will depend on the abundance of tumor cell dissemination or the number of tumor cells injected intravenously in the case of experimental metastasis assays. At present, our understanding of the extent to which tumor cell clusters intravasate through a different mechanism or a similar mechanism to single tumor cells remains poorly characterized and will benefit from new experimental models and clinical samples focused on capturing tumor intravasation events. However, as discussed in the next section titled Maneuvering Through Small Vessels, work has been done to show that bulky tumor cell clusters can travel through small vessels together.

1.4.2 *Maneuvering through small vessels*

The time spent in circulation by CTC clusters is shorter than that of individual tumor cells[28], presumably because CTC clusters become trapped in proximal vessels. However, microfluidic demonstrations show that tumor cell clusters display remarkable flexibility. Tumor cell clusters up to 20 cells in number can reversibly reorganize into single-file chains in capillary-sized vessels in microfluidic devices and in zebrafish models[110]. Weakening intercellular adhesions resulted in dissociation of clusters into single cells, while strengthening of intercellular adhesion resulted in occlusion of clusters in the constrictions, indicating that adhesion composition could dictate circulatory arrest. More

work is needed to establish how the interplay of mechanical stress and cell–cell adhesion in CTC clusters impacts their metastatic potential in vivo and in cancer patients.

1.5 CANCER TREATMENT FROM A COLLECTIVE METASTASIS PERSPECTIVE & FUTURE OUTLOOK

The ultimate goal of cancer research is to develop therapies and diagnostic tools that will eradicate and prevent cancer. While the collective metastasis of tumor cell clusters to distant sites remains a field in relative infancy, several major principles emerge, as discussed below.

For multiple phases of metastasis, tumor cells undergo a major boost when they are in physically cohesive clusters. These properties are apparent not only during dissemination (in transit) where tumor cell clusters are better shielded from physical and immunologic insults but also after arrival in the distant organ, supporting advantages for multicellular cohesion in survival, proliferation, and outgrowth into overt metastases. These robust effects are mediated in turn by adhesion systems, signaling molecules, and the spatial architecture of clusters that facilitate cooperation between tumor cells and are further supported by the actions of different assemblies of phenotypically distinct tumor cells and host cells. Despite the revolution in immunologic targeting and targeting of the tumor microenvironment, the core armamentarium of cancer therapy (cytotoxic chemotherapy, biologics, and small molecules) remains directed toward targeting cell-autonomous intracellular processes. Beyond these approaches, collective metastasis suggests the general principle of targeting intercellular tumor interactions as a strategy for anticancer therapy.

1.5.1 *Targeting adhesion*

Targeting tumor cell cluster adhesion has been proposed as a means of antimetastatic therapy. However, targeting adhesions could also be problematic; for example, epithelial cells in the major organs also harbor adhesion complexes including adherens junctions and desmosomes, and therefore greater specificity for tumor cell cluster adhesion will be needed for an adequate therapeutic index. In addition, disrupting cell–cell cohesion could induce counterproductive increases in tumor dissemination or disrupt clusters into smaller aggregates, which could increase rather than decrease metastatic seeding. Thus, the consequences of wholesale targeting of cell adhesion remains unclear. Another approach is to target adhesion and adhesion signaling between tumor cells and nontumor cells in clusters such as neutrophils and platelets. For example, integrin adhesion-targeted therapy against platelets is highly effective for the treatment of acute myocardial infarction. Tumor cell clusters show methylation patterns consistent with greater stemness factor expression[39]. Targeting of stemness factors such as CD44 could reduce tumor cell cluster adhesion as well as impair stem cell–associated signaling involved in early metastasis formation[48].

1.5.2 *Targeting collective signaling*

Another approach is to focus on the collective intercellular signals induced in tumor cell clusters. For example, some clusters utilize intercellular EGFR family receptor signaling in homotypic and heterotypic clusters and blocking these signaling mechanisms can markedly reduce metastasis in animal models[49,79]. Thus, blockade of collective intercellular signaling, and the specific receptor repertoires at intercellular contacts of tumor cell clusters, could offer a means to target micrometastatic disease and therapy-

resistant tumor cells. It is unclear whether cluster-induced signaling is a property only of small clusters, but the evidence of intercellular signaling in macrometastases suggests that these collective intercellular signals persist through development
of overt metastasis. In this case, targeting collective signaling could have benefits for both micrometastatic and macroscopic metastasis.

1.5.3 *Targeting heterogeneity*

A third approach is to target the interacting tumor cells within clusters themselves, which take on distinct cellular roles such as migration and proliferation and express distinct surface repertoires. Heterogeneity of marker expression will reduce the efficacy of cell-specific, cell-targeted antibodies. For example, HER2+ breast cancers that are heterogeneous for HER2 expression show worse responses to HER2-targeted antibody therapy[111], while HER2-antibody drug conjugates that release their cargo both on the target cell as well as neighboring cells have been proposed to more effectively target HER2-low or heterogeneous breast cancers. A challenge is the significant plasticity shown by many tumor cells, leading to interconversion events between different states. Inhibition of plasticity or, alternatively, combinatorial targeting of multiple cell populations could, in principle, yield more durable responses to therapy.

1.5.4 *Summary*

Whether it is targeting clusters for destruction, preventing them from forming, preventing them from entering circulation, or inhibiting their augmented growth, a key challenge is determining which cancer patients would stand to gain from therapies targeting collective interactions between cells. One possibility is that these intercellular interactions are most

important for dissemination and outgrowth but become dispensable beyond a certain point. In this case, anti-cluster therapy will need to be paired with other cytotoxic therapies that do have efficacy in macroscopic disease in the metastatic setting. However, another possibility that we think is likely is that at least some of these intercellular collective interactions persist from the microscopic cluster to the overt metastasis stage. Indeed, therapeutic targeting of cell adhesion molecules expressed on metastases such as Trop2 and nectin-4 has had robust effects in clinical trials in patients with advanced metastatic disease[112,113]. In this case, the study of tumor cell clusters provides a clue for the core dependencies that emerge early in metastasis formation. The prediction here is that collective-metastasis-targeted therapy should shrink macroscopic and microscopic tumors.

An additional consideration while targeting collective metastasis is the importance of host factors that may predispose cancers toward clustered dissemination and collective metastasis. For example, inflammatory breast cancers are prone to forming tumor emboli highly expressing E-cadherin with aggressive metastatic trajectories. Clinical studies collected from larger patient populations will be necessary to design informed therapies targeting collectivity. We know that the presence of CTC clusters in patients' blood is an indicator of poor prognosis compared with patients with only single CTCs. However, there is not much known about predictive markers that anticipate CTC cluster dissemination and collective metastasis. Are there some patients who are more prone to developing collective metastases based on factors such as genetics, environmental factors, and therapy exposure? This is an important area of study that is highly understudied but could

improve therapeutic strategies and outcomes, and there is virtually no information about how patient demographics relate to collective metastasis.

1.6 OUTLOOK

Through recent studies, the salient features of collective metastasis are emerging. Key observations include that CTCs occur both as single cells and as aggregated clusters, that these CTC clusters are potent seeds for new metastases, and that these CTC clusters generate polyclonal metastases in animal models. An attractive hypothesis is that CTC clusters deliver genetically and phenotypically heterogeneous tumor cell (and in some cases stromal) populations that promote metastasis and therapy resistance. At the same time, CTC clusters have now been shown to encompass a variety of properties considered useful for metastasis—including enhanced survival, anoikis resistance, immunoevasion, collective signaling, and outgrowth. We anticipate that as the field grows, a clearer picture may emerge for the major molecular components involved in collective metastatic seeding, providing a road map for cancer therapeutics.

There continues to be debate about what instigates the collective migration of tumor cell clusters and how these clusters disseminate into circulation. At present, there is strong evidence for collective invasion of tumor cells, cooperative interactions between different cell types, social-level behaviors such as resource sharing, and division of roles within the cluster; there is also robust evidence that heterotypic cell populations play important roles in supporting different stages of metastasis. There is significant work showing that partial or hybrid phenotypic EMT states may contribute to tumor dissemination and, because these cells do not lose their epithelial character

completely, show preference for collective migration. Whether cooperative cell populations or cell plasticity toward intermediate states are most important for the initiation of collective migratory behavior is not resolved, and indeed both processes could be operative simultaneously.

Most importantly, the timing and site of dissemination, and whether there are differences between the dissemination of single cells and clusters, are presently unknown. On the one hand, there is a tendency for CTC clusters to co-occur with a high abundance of CTCs. On the other hand, single tumor cells and collectively migrating cells would seem to require distinct cellular programs given their physical constraints. It remains to be tested whether there is a common driver of CTC and CTC cluster dissemination or whether there are favored mechanisms for the aggregation or disaggregation of CTCs into either form. We expect that improvements in technology to identify these rare events and models for collective dissemination will help to answer these questions. Finally, a key challenge is to bridge the gap between these basic studies of collective metastasis and clinical application for therapeutic targeting of metastasis. We suggest that collective interactions between cells, whether of the same or different phenotype and therefore the same or different surface repertoire, are likely to be important at all stages of metastasis. We expect that a concerted effort to define the intercellular interactions driving the collective migration and dissemination of clusters of cells will therefore be highly promising to unveil new paradigms for metastasis research and cancer treatment.

1.7 CHAPTER 1 FIGURES

Figure 1

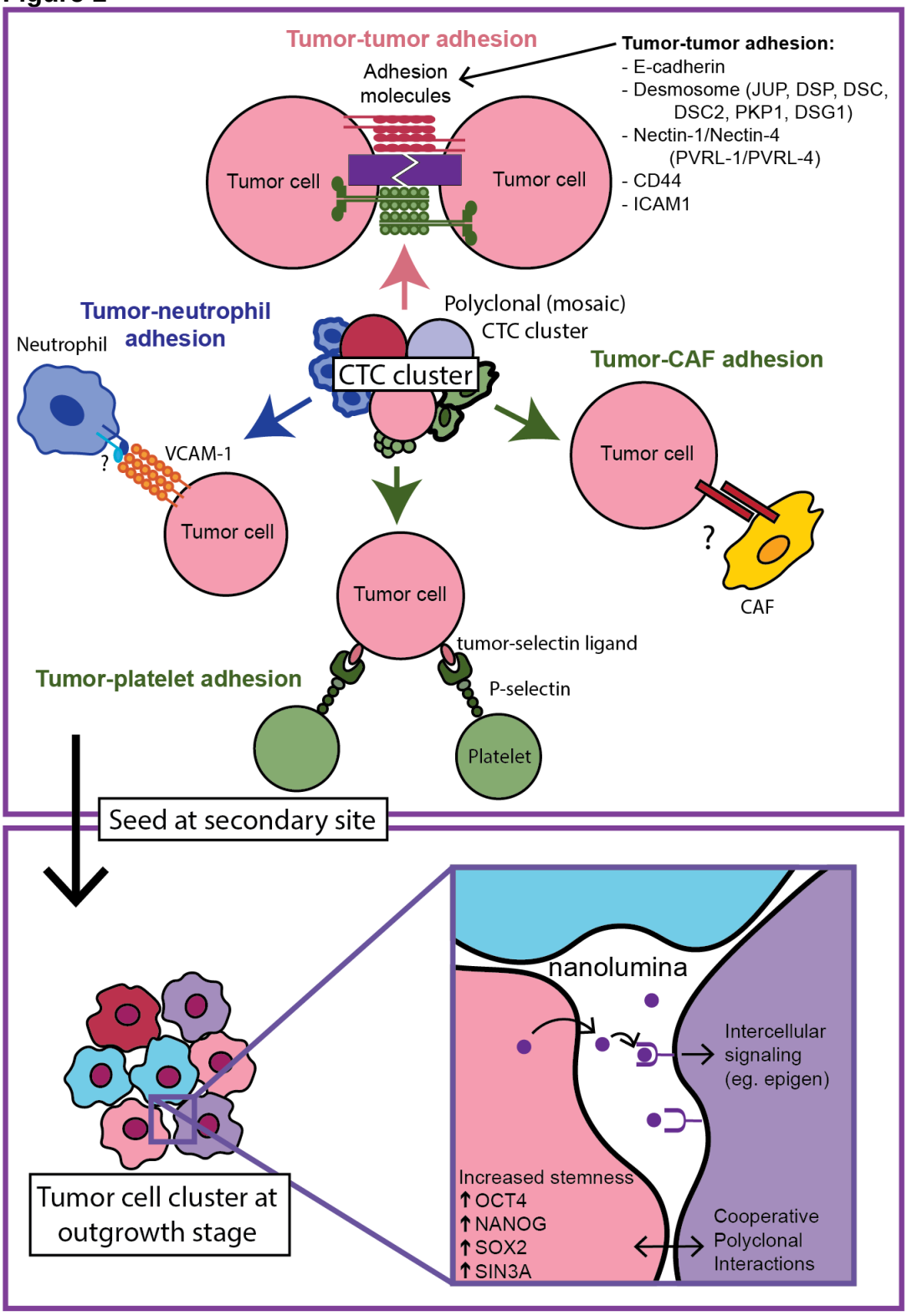

Chapter 1 Figure 1: Homotypic and heterotypic tumor cell clusters

Circulating tumor cells (CTCs) adhere to each other, to neutrophils, to platelets, and/or CAFs to form homotypic or heterotypic clusters through various adhesion mechanisms. Once at the secondary metastatic seeding site, tumor cell clusters can have outgrowth advantages over single cells through increased stemness, intercellular signaling, and cooperative polyclonal interactions. Nanolumina, sealed intercellular cavities between tumor cells, can concentrate soluble signaling molecules for intercellular signaling.

Chapter 2. BREAST CANCER-DERIVED ANGIOPOIETIN-LIKE 7 REGULATES NECROTIC CORE FORMATION AND METASTASIS FROM THE TUMOR INTERIOR

2.1 ABSTRACT

Necrosis in the tumor interior is a common feature of aggressive cancers that is associated with poor clinical prognosis and the development of metastasis. How the necrotic core promotes metastasis remains unclear. Here we report that emergence of necrosis inside the tumor is temporally correlated with increased tumor dissemination in a rat breast cancer model and in human breast cancer patients. By performing spatially focused transcriptional profiling, we identified angiopoietin-like 7 (Angptl7) as a tumor-specific factor localized to the peri-necrotic zone. Functional studies showed that Angptl7 loss normalizes central necrosis, reduces peri-necrotic dilated vessels and metastasis, and reduces circulating tumor cell counts to nearly zero. Mechanistically, Angptl7 promotes vascular permeability and supports vascular remodeling in the peri-necrotic zone. Taken together, these findings show that breast tumors actively produce factors controlling central necrosis formation and metastatic dissemination from the tumor core.

2.2 SIGNIFICANCE STATEMENT

Aggressive tumors often die from the inside out, a process called necrotic cell death. Necrosis is associated with dissemination of cancer cells but how necrosis promotes tumor dissemination is not understood. Here we used rats as a model organism to increase detection of dissemination events compared to mouse models. This uncovered an acute spike in circulating tumor cell (CTC) abundance associated with necrosis and

changes in blood vessels. Spatial dissection of gene expression revealed a tumor-derived gene program involved in shaping the tumor core ecosystem. We demonstrate that necrosis, vascular remodeling and metastatic dissemination are dependent on a tumor-secreted factor Angiopoietin-like 7 (Angptl7). Understanding the molecular factors regulating metastatic dissemination from the necrotic core could unveil new therapeutic strategies to treat and prevent metastatic cancers.

2.3 INTRODUCTION

The development of metastasis is the pivotal determinant of long-term survival in most human cancers[114]. A key step in this process is the dissemination of tumor cells into the systemic circulation[115,116]. A long-standing question is where tumor cells disseminate from. A major focal point of investigation is the tumor-stromal border where cancer cells are directly observed to invade singly or collectively into surrounding tissues and disseminate into local blood vessels[117,118]. Aiding this process are local conditions in the tumor microenvironment, such as hypoxia, acidity and nutrient deficiency, in partnership with immune cells, that promote tumor dissemination[119–122] . Counterintuitively, many of these microenvironmental influences are most prevalent in the tumor core, in regions of disordered tissue and blood vessel microarchitecture, where nutrient and oxygen availability are most limited[123,124]. One way to reconcile these competing observations is that tumor dissemination can also occur in the tumor core. Consistent with this hypothesis, the tumor core harbors abnormal biomechanics, increased interstitial pressure, and vascular leakiness which could be conducive to dissemination[124–126]. Further, tumor cells in the interior are actively migratory and spatially coordinated[127] and

tumor cell intravasation was determined to occur almost exclusively in the tumor core in an avian model system[128]. These observations suggest mechanisms for metastatic dissemination from the tumor core. However, owing to the spatial heterogeneity and cellular complexity of the tumor core ecosystem, the molecular factors regulating dissemination from within and the role of tumor cells, as active drivers or passive participants in this process, are not understood.

In the setting of extreme nutrient limitation and vascular compromise, tumor cells undergo necrotic cell death. Necrosis is a pervasive feature of many aggressive fast-growing tumors, associated with poor prognosis and markedly increased risk of metastasis[129–133]. A challenge of between-tumor/between-patient association studies is that it is not possible to disentangle if necrosis is a regulator of metastasis or a byproduct of other more aggressive features such as tumor grade or tumor subtype[134,135]. In this regard, spatial analyses within regions of the same tumor are suggestive. Spatial analyses of blood vessel invasion in lung cancers, sarcomas, hepatocellular carcinoma and breast cancers have observed that between 25 to 50% of all blood vessel invasion events occur intratumorally in the tumor core[136–139]. Likewise, spatial and temporal multiregional sequencing of primary and metastatic renal cell carcinomas reveal that metastatic subclones preferentially originate from the tumor interior where necrosis and increased copy number alterations predominate[140]. Tumor cells that are dead cannot themselves give rise to metastasis. However, these clinical observations indicate that tumor cells neighboring the most intense regions of necrosis make productive contributions to metastatic dissemination. How the necrotic core promotes metastatic dissemination remains unclear.

In this study, we leveraged a rat transplantation model to uncover a temporal correlation between tumor dissemination and the formation of large contiguous zones of necrosis within the tumor core. These necrotic zones harbored dilated blood vessels and intravascular tumor cells. Importantly, our studies revealed a tumor-cell secreted factor Angiopoietin like-7 (Angptl7) that regulates formation of necrosis. Our studies define a targetable axis of the necrosis ecosystem to suppress metastatic dissemination from the tumor interior.

2.4 RESULTS

2.4.1 *A low to high CTC transition occurs in a rat transplantation model of breast cancer*

Identifying tumor cells in transit is painstaking in foundational models for cancer metastasis research including mouse, zebrafish, and chick embryo[128,141–146]. We hypothesized the use of rats, a larger animal model, would enable more robust detection of dissemination events locally and systemically in the circulation. In this study, we employed **S**CID rats on the Sprague-Dawley background with a double knockout for the **R**ag2 and Il2r**g**amma genes (denoted SRG[147]). SRG rats are deficient in T-cells, B-cells, and NK-cells similar to NOD scid gamma (NSG) mice. To compare the performance of these two transplantation models, we transplanted 4T1 tumor cells, a mouse mammary tumor model of triple-negative breast cancer, transduced with a GFP reporter, into the mammary fat pad of SRG rats or NSG mice and collected all tumors synchronously once maximum tumor size was reached for mice, which was 2cm in our animal facility **(Fig. S1A)**. Altogether, SRG rats produced 3 times larger tumors by weight and by estimated

tumor volume **(Fig. S1B-C)**. 10 times more blood was collected with SRG rats, which in turn yielded 10 times more single CTCs and CTC clusters per animal **(Fig. S1D-G)**. For both CTCs and CTC clusters, morphologic appearance and relative proportions in blood were identical between SRG rats and NSG mice **(Fig. S1E, H)**. Consistent with the increased CTC abundance, lung metastases counted by stereomicroscopy were 4 times more abundant in SRG rats **(Fig. S1I-J)**. Because the same number of 4T1 cells were transplanted in both SRG rats and NSG mice and because tumors were harvested at the same time, our direct comparison showed that the rat transplantation model increases the efficiency of detecting rare tumor dissemination events by 10-fold.

Having identified the rat xenograft model as an efficient system to study CTC dissemination, we next applied this model to determine CTC abundance temporally.

We transplanted GFP-labeled 4T1 cells into the mammary fat pad of SRG rats and sacrificed the animals at four time points after rats developed palpable tumors **(Fig. 1A)**. Blood, lungs and tumors were harvested at days 13, 17, 22, and 27 post-transplantation. In this model, tumor size increased significantly between days 13 and 17 with evidence of growth plateau and significant variance in tumor size between SRG rats by both estimated tumor volume and by tumor weight **(Fig. S2A-B)**. Surprisingly in the same time frame, we observed a pronounced non-linear increase in CTC abundance. Specifically, between days 22 and 27, we identified a ~50-fold increase in CTCs and ~10-fold increase in CTC clusters **(Fig. 1B-C and Fig. S2C-D)**.

2.4.2 *The low to high CTC transition is associated with a necrotic tumor core, dilated vessels, and peri-necrotic tumor cell vascular invasion*

Given the very robust increase in CTC abundance that was uncorrelated with primary tumor burden, we next asked how primary tumors were changing on a cellular level. Hematoxylin and eosin (H&E) staining of tumors revealed tumors that were histologically indistinguishable at the tumor-invasive border over time **(Fig. S2E)**. Instead, H&E revealed robust changes in the tumor core with appearance of confluent zones of central necrosis. Total necrotic area in the primary tumor increased over time with marked elevation between days 22 and 27, whereas total viable area increased early and subsequently plateaued **(Fig 1D-F)**. As a second method, tetrazolium chloride assay, a colorimetric method for determining cell viability, confirmed that total necrotic area, but not total viable area, increased markedly in the late time point **(Fig. S2F-H)**. Likewise, the number of lung metastases per animal was highly correlated with necrotic area, but not tumor volume **(Fig. S2I-K)**.

Extending these results further, we stained tumors for VE-cadherin to mark blood vessels. VE-cadherin staining demonstrated abnormal dilated blood vessels, penetrating the necrotic core, that markedly increased in abundance and density between days 22 and 27 **(Fig 1G-H, S3A-B)**. In contrast, neither total microvascular abundance nor density increased over the same time points **(Fig. S3C-D)**. The number of lung metastases per animal and CTCs per animal were highly correlated with the number of dilated vessels but not nondilated vessels **(Fig. S3E-H)**. Functionally, dilated vessels were less often labeled by fluorescent lectin compared with non-dilated vessels, indicative of differences in blood flow between vessel types **(Fig. S3I-J)**. Strikingly, dilated vessels contained

GFP+ multicellular tumor cell clusters, consistent with vascular invasion **(Fig. 1I-J)**. Together, these data reveal an acute low to high CTC transition that coincides with robust changes in the tumor core, not rim. These tumor core alterations included confluent zones of necrosis and necrosis-adjacent dilated blood vessels containing intravascular tumor cells.

2.4.3 *Transcriptome profiling comparing tumor core and rim reveal that Angptl7 is a tumor-specific, core-enriched factor localized to the peri-necrotic zone.*

We next sought to define the molecular changes defining the necrotic core. To this end, we dissected out tumor core from the rim, and interrogated gene expression originating from tumor or from host cells **(Fig. 2A, Supplementary Table 1)**. In this regard, the properties of the rat transplant model and the use of a mouse-in-rat xenograft were advantageous. At time of harvest, rat tumors were 3 cm diameter or larger and had distinct tissue morphology between the firmer tumor rim and softer, pinker tumor core, that was in some cases also obviously liquified **(Fig. S4A),** enabling us to reliably macrodissect the necrotic core from the non-necrotic rim. Following RNA-sequencing of macrodissected regions, sequence reads were further aligned to a concatenated rat-mouse combined genome, and deconvoluted to obtain tumor-derived gene expression (originating from mouse) vs. host-derived gene expression (originating from rat). This deconvolution algorithm robustly separated mouse and rat RNA transcriptomes and revealed that 76% of reads were mouse-in-origin in tumor rim, and 84% of reads were mouse-in-origin in tumor core **(Fig. S4B),** indicating the majority of reads were tumor-derived.

Gene-ontology analysis further revealed distinct patterns of ontology enrichment between tumor and host, and between rim and core **(Fig. S4C, Supplementary Table 2)**. In the host transcriptome, gene sets typically associated with the invasive border were upregulated in the rim (including extracellular matrix, vascular morphogenesis, and locomotion), while gene sets associated with tissue necrosis were upregulated in the core (including cellular stress response, RNA metabolism, and neutrophil degranulation). Likewise, in the tumor transcriptome, gene sets associated with replicating cells were upregulated in the rim (cell cycle, DNA replication), while gene sets involved in vascular remodeling appeared upregulated in the core (vasculature development/morphogenesis, matrisome, and regulation of cell adhesion).

These gene expression patterns revealed that tumor cells in the interior actively express genes associated with vascular tube morphogenesis. However, these core genes could be expressed in both tumor and host compartments. To illustrate, the top differentially expressed tumor-derived gene was *Camk1d.* However, host-derived *Camk1d* was also expressed in both core and rim; therefore, *Camk1d* is not tumor-specific (**Fig. S4D**). To identify top core-enriched tumor-specific genes, we performed interspecies analysis to discover genes that were specifically mouse tumor-derived and not expressed in the rat host (**Fig. 2B**). The top enriched factor from this analysis was Angiopoietin-like 7 (*Angptl7*), enriched 32-fold in tumor versus host, and over 16-fold in tumor core versus tumor rim **(Fig. 2C)**. The enrichment for Angptl7 in the tumor core was further confirmed by qPCR, western blot, and ELISA specific for mouse Angptl7 **(Fig. 2D, Fig S4E-G)**. In addition, we performed RNA in situ hybridization (ISH) for mouse *Angptl7* **(Fig. 2E, Fig. S4H)**. To quantify spatial enrichment, we calculated the distance of every

spot relative to the nearest tumor-stromal border or tumor-necrotic interface. *Angptl7* was markedly enriched in a peri-necrotic distribution in the tumor core and with close to no expression in the tumor rim. These findings show that Angptl7 is a tumor-derived factor enriched in the core of high-CTC tumors, and spatially localized to the peri-necrotic zone.

2.4.4 *Angptl7 suppression markedly normalizes histologic necrosis in the tumor core and reduces the number of CTCs and metastases.*

ANGPTL7 belongs to a family of secreted proteins structurally related to the angiopoietins and that have been implicated in lipid metabolism, cardiovascular disease, stem cell renewal, and cancer[148–155]. Compared with other ANGPTL proteins, ANGPTL7 is among the least characterized, being predominantly expressed in the human cornea, and elevated in the aqueous humor of the eye in patients with glaucoma, a disease of increased intraocular pressure[156–160]. In the rat model, we observed that the number of Angptl7 RNA detections increased markedly over time and was highly correlated with total necrotic area, dilated vessels, CTCs, and lung metastases **(Fig. S5A-E)**. Given that we observed strong spatial and temporal association between Angptl7 expression and the necrotic core, we next asked whether Angptl7 is required for necrotic core formation and metastatic dissemination. To answer this question, we transduced 4T1 tumor cells with a puromycin selectable membrane-GFP lentiviral vector and a second blasticidin selectable lentivirus encoding for shRNA hairpin and expressing cytoplasmic mCherry to generate stably transduced non-targeting control and Angptl7 knockdown (KD) lines expressing both fluorescent reporters **(Fig. 3A)**. No differences in survival, proliferation, or ability to form clusters were observed between conditions during in vitro culture. Non-targeting control knockdown lines and Angptl7-knockdown (KD1-3) were each

transplanted orthotopically into SRG rats. Because Angptl7 expression was undetectable in vitro **(Fig. S4E)**, but highly induced in vivo, knockdown efficiency was confirmed in harvested tumor. By qPCR, Angptl7 RNA expression was markedly reduced with all three knockdowns KDs **(Fig. 3B)**. Because Angptl7 expression is low in whole tumor lysates, knockdown was confirmed on a protein level by ELISA of tumor interior, and Angptl7 protein expression was significantly reduced in KD1 and KD3 in the tumor interior, where Angptl7 expression is higher than in whole tumor lysates **(Fig. 3C and Fig S6A)**.

Having confirmed knockdown, we next evaluated tumor histology by H&E staining. Strikingly, knockdown of Angptl7 induced between 53 to 77% reduction in area of necrotic cores **(Fig. 3D-E)**. One possibility is that decreasing necrosis could promote tumor growth, a tradeoff observed in prior studies with perturbations improving vascularization[121,161]. However, suppression of Angptl7 did not increase either total viable area, tumor weight, or tumor volume, indicating that Angptl7 suppression does not promote tumor growth **(Fig. 3F-G and Fig. S6B)**.

Given these effects on the histology of the tumor core, we next evaluated the effect of Angptl7 knockdown on CTC abundance and metastasis. Remarkably, we observed drastic reductions in both mCherry+ single CTC and CTC cluster abundance, which reduced from an average of 181 single CTCs down to 1 single CTC, and from 36 CTC clusters down to 0 CTC clusters for the best knockdowns **(Fig. 4A-C and Fig. S6C)**. Likewise, the number of mCherry+ lung metastases was also markedly reduced in Angptl7 knockdown conditions **(Fig. 4D-E)**. For the different knockdowns, the degree of necrosis suppression correlated with degree of CTC dissemination and metastasis suppression. Likewise, we observed reductions in GFP+ CTC, CTC cluster, and lung

metastasis abundance **(Fig. S6D-F)**. Taken together, these data establish that Angptl7, a tumor-specific factor that is specifically expressed in the tumor interior, is necessary for necrosis formation in the tumor core, dissemination of both single and clustered CTCs, and lung metastasis.

2.4.5 *Angptl7 suppression normalizes a subset of tumor core gene expression and regulates blood vessel morphology and vascular permeability.*

Given the marked decrease in intratumoral necrosis, CTC abundance, and metastasis when Angptl7 was suppressed, we next transcriptionally characterized Angptl7 knockdown tumors. Bulk RNA-seq was performed, tumor core and rim were compared, and tumor and host derived transcripts were deconvoluted. We applied tumor core and rim gene sets from our initial xenograft deconvolution experiment **(Fig. 2A)**, evaluated gene set enrichment between conditions, and observed marked depletion of tumor-derived core and host-derived core gene expression in both core and rim of Angptl7 knockdowns **(Fig. S7A, Supplementary Table 3)**. Likewise, we observed marked enrichment for tumor-derived rim and host-derived rim gene expression in both core and rim of Angptl7 knockdowns.

While depletion of core gene expression was in line with the significant reduction in necrosis observed by H&E, this depletion was not complete, with 23% of tumor derived core genes and 35% of host derived core genes increased in Angptl7-knockdowns **(Fig. S7B)**. Gene ontology analysis was performed to stratify the tumor core program into normalized and non-normalized components. Tumor-derived blood vessel morphogenesis genes and host-derived neutrophil degranulation gene sets were depleted in Angptl7-knockdown conditions, while core matrisome (tumor), RNA

translation (host) and TCA transport (host) persisted or increased in Angptl7-knockdown condition compared with non-targeting control **(Fig. S7C)**. Taken together, these transcriptional studies reveal that Angptl7 regulates large-scale remodeling of the tumor core. Angptl7 supports expression of a subprogram of genes expressed in the tumor core that are involved in blood vessel morphogenesis and neutrophil degranulation. However, Angptl7-knockdown does not correct tumor core defects in RNA and nutrient metabolism, indicative of persistent cellular stress in the tumor interior.

Having identified vascular morphogenesis genes as potentially Angptl7 regulated, we next characterized the spatial distribution and expression of blood vessels in the Angptl7 knockdown tumors **(Fig. 5A)**. Total VE-cadherin-positive vessel number and density were similar between Angptl7 knockdown and non-targeting control tumors **(Fig. 5B, S8A-B)**. In contrast, the number and density of VE-cadherin-positive dilated vessels were markedly reduced in Angptl7 knockdown tumors **(Fig. 5C**, **S8C)**. Further, smooth muscle actin staining, indicative of smooth muscle cell or contractile pericyte coverage, was uncommon around dilated vessels in both control and Angptl7 knockdown tumors, and not altered by Angptl7 suppression **(Fig. S8C-G)**. Because Angptl7 is also reported to regulate lymphangiogenesis[151], we also stained lymphatics for podoplanin. In contrast to VE-cadherin, we observed no significant difference in lymphatic vessel density, morphology, or peri-necrotic localization **(Fig. S9A-D)**. Lymphatic vessels were more prominent in viable regions of the tumor, closer to the tumor edge **(Fig. S9C-D)**. Taken together, these data show that Angptl7 is necessary for the peri-necrotic dilated vessel phenotype.

Given the effect of Angptl7 suppression on dilated vessel morphology, we next examined the effect of ANGPTL7 on vascular permeability. Human umbilical endothelial vein cells (HUVECs) plated on 2D were incubated with recombinant human ANGPTL7 from 1ng/mL to 100 µg/mL and measured for changes in vascular permeability using a live-cell impedance assay. Strikingly, HUVECs showed a dose dependent response to ANGPTL7 addition that was most pronounced by 1 hr of treatment which persisted out to 24 hrs at 10 ng/mL and higher recombinant ANGPTL7 concentrations **(Fig. 5D-F)**.To define gene pathways associated with ANGPTL7 induced changes, HUVEC cells were treated with 10 µg/mL ANGPTL7 for 24 hrs and then harvested for RNA-seq. Gene ontology analysis revealed dominant enrichment for cytoplasmic ribosome-encoding genes, weaker enrichment for genes involved in Parkinson disease, neuron projection development, and mitochondrial organization **(Fig. 5F, Supplementary Table 4)**. Further, signaling pathway enrichment was observed for genes involved in SLIT and ROBO signaling (log Q-value -32), previously implicated in endothelial-tumoral crosstalk during metastatic dissemination[162]. Taken together, these data indicate that Angptl7 supports vascular remodeling in vivo, increases vascular permeability, and induces gene expression changes in endothelial cells in vitro.

2.4.6 *ANGPTL7 is highly expressed in high-necrosis triple-negative human breast cancer patient-derived xenografts*

Clinically, necrotic zones are generally avoided during diagnostic tissue sampling due to lower abundance of viable tissue in these regions. To extend the human disease relevance of our findings in rat models, we evaluated *ANGPTL7* mRNA by RNA-ISH from

7 tumor sections from 6 different human breast cancer patient-derived xenografts (PDXs) each derived from high-grade invasive ductal carcinomas, and each triple-negative (ER negative, PR negative, HER2 negative receptor status) by PDX tumor histology **(Fig. 6A)**. Even amongst these high-grade tumors, the percentage of necrosis varied markedly between models. Likewise, *ANGPTL7* expression varied between models and was markedly higher in high necrosis models. For comparison, model J000106527, which had very low necrosis and *ANGPTL7* expression was derived from a patient with T4bN0 high-grade TNBC. This patient developed a second primary breast cancer 4 years later that was resected and then treated with adjuvant endocrine therapy. In contrast, model J000106528, which had the highest necrosis and *ANGPTL7* expression of all models tested, was derived from a patient with T3N2 high-grade TNBC. This patient developed metastatic breast cancer within 2 years from initial diagnosis and tumor resection and progressed rapidly on therapy. Taken together, these clinical observations and experimental studies in PDX models demonstrate that ANGPTL7 is associated with necrotic zones in human TNBC.

2.4.7 *Necrosis markers are associated with CTC dissemination and metastasis in breast cancer patients*

Given the association between necrosis and CTC abundance in our rat model, we hypothesized that necrosis markers are associated with CTC dissemination in human breast cancer patients. To test this hypothesis, we interrogated longitudinal CTC abundance from patients with metastatic breast cancer recruited to an IRB-approved study at the Fred Hutchinson Cancer Center and the University of Washington (FH 8649).

Over a 3-year period, a total of 102 blood samples from 40 patients were longitudinally collected including 35 women with estrogen receptor-positive metastatic tumors and 5 with estrogen receptor status that was negative or unknown **(See Supplementary Table 5 for demographic information)**. For each blood sample, the cellular fraction was separated by density, deposited to slides, and CTCs enumerated for by computer-assisted image analysis using the Rarecyte platform. 29 patients (73%) had at least one CTC at any timepoint, 5 patients (13%) had at least one CTC cluster at any timepoint, and 11 patients (27%) had no CTCs at any timepoints. As expected based on prior studies, patients with CTCs detected at first blood draw had significantly worse overall survival and early death **(Fig. 6B,C)**. Likewise, patients with CTC clusters at first or second blood draw had markedly worse overall survival and early death **(Fig. 6B,D)**.

Among patients with CTCs at any time point, substantial differences in CTC dynamics were observed, and in a subset of cases, extreme elevations in CTC abundance between time points (**Fig. 6E and Fig. S10A-B for case vignette**). 16 blood samples were selected from 8 patients, made up of matched early and late time-points (**Supplementary Table 6**). Blood plasma from all 16 samples were depleted of high-abundance proteins, labeled with tandem-mass-tags, and interrogated by LC-ESI mass spectrometry. Comparison of high CTC samples with all low CTC samples yielded 46 proteins highly associated with high CTC state and passing q-values of 0.1 or less **(Fig. 6F)**. ANGPTL7 was not detected by LC-ESI mass spectrometry precluding its comparison between CTC states. Metascape gene set analysis demonstrated the top enrichment being for gene-sets linked to necrosis **(Fig. 6G)** including: 1) Cori cycle, the major pathway for lactate metabolism, 2) the 20S proteosome which has been associated with

necrosis[163,164], and 3) neutrophil degranulation, which we also identified as a top gene set in our core/rim RNA-seq analyses. To control for inter-patient variation, we further conducted a pair-wise comparison of late versus early time points from 3 patients with low to high CTC transitions. Of the 17 proteins increased 2-fold or more between late and early time points, 13 (76%) were necrosis-associated (**Fig. S10C**). To validate our proteomic observations, we further measured levels of the necrosis associated marker lactate dehydrogenase (LDH) from plasma for 93 blood samples and 39 patients. Consistent with our proteomic enrichments, marked elevations in LDH were associated with a 10 or more increase in CTC abundance between time points, with blood samples with 20 or more CTCs, and with blood samples with CTC clusters **(Fig. S10D-F)**. Taken together, these clinical, biochemical and proteomic studies show that as seen in our rat model experiments, low to high CTC transitions are associated with increasing CTCs and markers of necrosis in patients with metastatic breast cancer.

2.5 DISCUSSION

A key challenge in metastasis research is to discern where and how tumor cells disseminate to distant organs. However, understanding where metastatic dissemination originates from is a formidable challenge. Tumor dissemination is a dynamic process that is difficult to capture[128,141–146] occurring in the context of spatially heterogeneous ecosystems varying in their nutrient availability, perfusion, oxygenation, and host contributions[123,165,166]. Here we developed a rat transplantation model of breast cancer that increases CTC detection 10-fold compared to mouse models and leveraged this model to identify cellular and molecular changes in tumor dissemination. Importantly, we

observed that tumor dissemination was strongly correlated temporally with necrosis in animal models and in human cancer patients, that tumor dissemination was localized spatially to dilated peri-necrotic vessels in the tumor interior, and that tumor dissemination was dependent functionally on the expression of a factor, Angptl7, produced by peri-necrotic tumor cells. Our findings in breast cancer models, in conjunction with recent clinical observations[136,140], provide strong evidence for tumor dissemination from the tumor interior.

Decoding the molecular regulation of dissemination in the tumor interior is a particularly challenging chicken-and-egg problem because the tumor core is composed of regions that are hypoxic, deficient in nutrients, and abnormally perfused[123,165,166], each of which could influence and in turn be influenced by adaptive responses from tumor cells in the core[123]. The very large tumors produced in our rat model enabled us to spatially dissect tumor core from tumor rim for transcriptional profiling and the use of xenograft deconvolution methods further enabled us to discern which genes were expressed specifically in tumor and host. In this regard, the use of a mouse-in-rat xenograft was serendipitous and essential. The limitation of this mouse-in-rat transplantation model is that it requires an immunodeficient host animal model, meaning that there is information lost regarding missing immune cells and their role in the metastatic process. Nonetheless, We suggest that rats are a valuable model organism with unique attributes supporting their use in metastasis research alongside more commonly used in vivo models such as mouse and zebrafish. These studies unmasked a tumor-derived program in the core and identified Angptl7 as the top-ranked secreted factor. Strikingly, Angptl7 suppression normalizes histologic findings of central necrosis and dilated peri-necrotic vasculature.

On a molecular level, Angptl7 depletion resolves vascular morphogenetic, hypoxic, and inflammatory changes associated with the tumor core but not gene programs associated with stress, RNA metabolism and nutrient depletion. These findings suggest that tumor necrosis arises from the sequential activation of stress programs in the core that induce a tumor-cell driven transcriptional response including Angptl7. Thus, Angptl7 is both regulated by the local microenvironment in the tumor interior and a regulator of further central necrosis and metastatic dissemination. Future studies are needed to define the signals and regulatory programs driving the tumor core adaptive response program.

Previous studies have shown that tumor dissemination can depend on macrophage-led migration, vascular mimicry, EMT, and collective migration[167–175]. Our data establish the importance of the necrotic zone in supporting metastatic dissemination and highlight the presence of intravascular tumor emboli within dilated peri-necrotic vessels. We note that both dilated vessels and Angptl7 were on average 2mm away from the nearest tumor border. Given the great distance of the central necrotic zone to the tumor-stromal interface, advances in intravital imaging in deep tissues[176,177] will be essential to evaluate which of these cellular dissemination mechanisms predominates in the necrotic zone. In addition, organotypic culture models have proven useful in modeling invasion in vitro that have morphologic correlates in vivo[172,173,178,179]. Our transcriptional dissection provides a reference point in which to develop organotypic models that more faithfully mimic the necrotic core-associated dissemination program. In particular, the formation of dilated vessels is strongly associated with tumor dissemination and metastasis. At present, how vessels become dilated is unclear. Whether dilated vessels arise from extrinsic compression from proliferating tumor cells, influence of the

extracellular matrix, or reflects occlusion by tumor cell emboli is unclear and could benefit from better organotypic models incorporating vasculature. Finally, previous clinical and experimental studies have shown that tumors can disseminate early preceding the detection of frank invasive cancer[180,181], while at the same time, that very large tumors are more likely to develop metastatic cancer[182,183]. Our data are compatible with these clinical observations. Because tumor necrosis can arise independently of tumor invasion, small fast-growing tumors could undergo necrosis early, while large tumors could undergo necrosis late. Consistent with our experimental observations, comedonecrosis is associated with increased risk of death from in situ, pre-invasive cancers[184].

From a therapeutic standpoint, our data indicate that ANGPTL7 is a fulcrum for eliciting central necrosis and metastatic dissemination. ANGPTL proteins have three conserved domains including an N-terminal coiled-coil domain that mediates homo-oligomerization, a linker peptide, and a C-terminal fibrinogen-like domain[185]. More studies are needed to investigate the functional domains of ANGPTL7 necessary for necrosis and metastatic dissemination. Therapeutic blocking antibodies and anti-sense oligonucleotides targeting ANGPTL3 reduce atherogenic lipoprotein levels and decrease the odds of developing cardiovascular disease in humans[149,150], supporting ANGPTL family of proteins as druggable targets. Necrosis is associated with aggressive tumors and is a common tumor response to many cancer treatments. Given the pronounced effects of Angptl7 depletion in our rat model, we suggest that ANGPTL7 is a target for future drug development for necrosis and metastasis suppression.

2.6 MATERIALS AND METHODS

2.6.1 *Methods*

Experimental Model and Subject Details

Animal models

All mice were maintained under specific-pathogen-free conditions, and experiments conformed to the guidelines as approved by the Institutional Animal Care and Use Committee of Fred Hutchinson Cancer Research Center (FHCC). The SRG OncoRats, **S**CID rats on the Sprague-Dawley background that harbors a double knockout for the **R**ag2 and Il2r**g**amma genes (SRG), were purchased from Hera Biolabs. Similar to NSG mice, SRG rats are a double knockout for the Rag2 and Il2rgamma genes (SD-Rag2tm2hera Il2rgtm1hera) and lack B-cells, T-cells, and NK-cells. For mouse experiments, NSG mice (NOD.Cg-Prkdcscid Il2rgtm1Wjl/SzJ) were used. 8-13 week old female mice and rats were used for all experiments.

Human breast cancer patient samples

Blood from patients were obtained from consenting patients under a Fred Hutch IRB approved study (FH8649) for longitudinal monitoring of circulating tumor cells in metastatic breast cancer patients. CTCs and CTC clusters were enumerated in these fluid samples using a RareCyte assay[186]. For details on the receptor status and pathology of each deidentified human sample used, see **Supplementary Table 1.**

Cell lines

293FT (ThermoFisher Scientific R70007) cell line was grown at 37°C, 5% CO2 in DMEM high glucose, GlutaMAX supplement, pyruvate (GIBCO 10569-010) supplemented with 10% fetal bovine serum (Sigma-Aldrich F0926-500ML) and 1% penicillin/streptomycin

(Sigma-Aldrich P4333). 4T1 (ATCC CRL-2539™) and HCC70 (ATCC CRL2315) cell line was grown at 37°C, 5% CO2 in RPMI, GlutaMAX supplement (GIBCO 61870-127) supplemented with 10% fetal bovine serum (Sigma-Aldrich F0926-500ML) and 1% penicillin/streptomycin (Sigma-Aldrich P4333). For non-adherent culture, cell lines were cultured in complete media + 2% (v/v) Matrigel. All cell lines used were from human females. 4T1 Cells were purchased from American Type Culture Collection (ATCC). 4T1-cyto-eGFP cells were a gift from the Cyrus Ghajar at Fred Hutchinson Cancer Center. 4T1-AcGFP1-mem-9 cells were generated by transducing 4T1 cells from ATCC with the rLV.EF1.AcGFP1-Mem-9 lentiviral particle (MOI=5) (Takara Bio). 4T1-AcGFP1-mem-9 cells were selected with 10ug/ml puromycin for at least 2 weeks.

Methods:

2D Cell Culture:

4T1 cells were cultured 2D on adherent plates in RPMI +10% FBS + 1% Penicillin-Streptomycin solution. 4T1-AcGFP1-mem-9 were cultured with RPMI complete + 10ug/ml puromycin. Angptl7 knockdowns and non-targeting control 4T1 cells were cultured with RPMI complete + 10ug/ml puromycin + 10ug/ml blasticidin.

3D Cell Culture:

2D cultured cells were trypsinized with 0.25% trypsin, then quenched with complete RPMI. Cell suspension was centrifuged at 400g for 5mins, then resuspended in Accumax. Accumax suspension was place in 37°C water bath for 30mins, pipetting up and down every 10 minutes. After centrifuging for 5min at 400g, pellet was resuspended in complete

RPMI + 2% Corning® Matrigel® Growth Factor Reduced (GFR) Basement Membrane Matrix (354230) (Corning). Cells were plated in non-adherent 6 well plates at 150,000 cells/mL with 4mL media per well.

Generating knockdown 4T1 cell lines:

4T1-AcGFP1-mem-9 cells were transduced with lentiviral particles generated with shERWOOD UltramiR Lentiviral Inducible shRNA (TransOMIC) for Angptl7 and selected with 10ug/ml puromycin + 10ug/ml blasticidin for at least 2 weeks.

SRG rats:

The SRG OncoRats, **S**CID rats on the Sprague-Dawley background that harbors a double knockout for the **R**ag2 and Il2r**g**amma genes, were purchased from Hera Biolabs. SRG rats are a double knockout for the Rag2 and Il2rgamma genes (SD-Rag2tm2hera Il2rgtm1hera) and lack B-cells, T-cells, and NK-cells.

Orthotopic transplantation into mammary fat pad of rats and mice:

Cells to be transplanted were cultured 3D for 2 passages before being transplanted. After the second passage, cells were plated in non-adherent 6 well plates at 150k cells/mL with 4mL media per well for the cells to aggregate over 24 hours before being transplanted. Spheroids formed this way were resuspended in 1:1 Matrigel:DMEM/F12 mix, kept on ice. 600,000 cells in 20µl Matrigel DMEM/F12 mix were transplanted into the right T4 mammary fat pad of rats or mice. Estimated tumor volume was calculated based on caliper measurements with the formula: $V = (W^2 \times L)/2$.

Blood collection from rats and mice:

For rats, peripheral blood was collected terminally though the left ventricle of the heart, into CellSearch CellSave tubes (Menarini-Silicon Biosystems) with heparin-coated syringe attached to an 18g needle. Rats were put under deep anesthesia with isoflurane to do this, and rats were euthanized immediately after blood collection. Blood tube was inverted at least 10 times immediately after blood collection, and blood was processed within 4 hours of collection. For mouse blood, peripheral blood of 8 mice were collected into one CellSave tube using a new heparin coated syringe for every mouse.

Density separation of buffy coat (nucleated cells) from blood:

Peripheral blood was diluted 1:1 with D-PBS then layered on top of 8mL of Ficoll (GE Ficoll Paque Plus GE17-1440-02 for human blood and Ficoll Paque Premium GE17-5442-02 for mouse and rat blood) in a 2.5% BSA-coated 50mL conical tube. Tube with Ficoll and diluted blood were centrifuged at 400g for 35mins with 0 acceleration and deceleration. The cloudy, white layer (“buffy coat”) between the clear Ficoll layer and the top plasma layer and the plasma layer were collected into a separate BSA-coated tube. Buffy coat and plasma layer mix were centrifuged at 4°C at 3500g for 30mins to pellet nucleated cells, then resuspended with D-PBS. To visualize Buffy Coat containing CTCs, cell suspension was spun onto slides using a Cytospin (800g for 5mins). After drying slides completely, slides were fixed with 4% PFA for 5 mins, washed with D-PBS 5mins 3 times. Slides were dried completely again before being stored in -80°C. For plasma collection, plasma layer was collected from the plasma layer from the Ficoll density

separation or from a separate blood tube in an AccuCyte Blood collection tube processed by Rarecyte with a 3000g 25 minutes spin at 25°C.

Immunofluorescence staining:

Slides were thawed at room temp for 5 minutes. For OCT tissue sections, slides were washed 5 mins 3x to wash OCT off. Slides were block for 1 hour with blocking solution (2.5% BSA, 5% normal goat serum or normal donkey serum, 0.3% triton in D-PBS). Primary antibody in blocking solution was placed on slides and incubated at room temp for 2 hours. We then washed the slides 5mins 3x with D-PBS before placing the secondary antibody in 5% normal goat serum or normal donkey serum in D-PBS on the slide to incubate for 1 hour. Slide was washed again 5mins 3x with D-PBS. Excess moisture was removed from the slide, and slide was mounted with 30-50µl Prolong Diamond Antifade Mountant and glass coverslip. Slide was cured overnight room temp, then stored at 4°C.

Bulk RNA-seq:

4T1 cells were transplanted into the right #4 mammary fat pad of SRG rats. At day 27 post-transplantation, primary tumors were harvested. Tumor was cut in half to expose the cross section. The inner, necrotic region and the outer, non-necrotic region were separated and snap frozen for RNA-seq and sent to Genewiz-Azenta for RNA extraction, library prep, and sequencing. Qiagen RNeasy kit (Qiagen, Inc 74104) was used for in-house RNA extraction before samples were sent to Genewiz.

Azenta Genewiz RNA-seq:

Sample QC, library preparations, sequencing reactions, and initial bioinformatic analysis were conducted at GENEWIZ, LLC./Azenta US, Inc (South Plainfield, NJ, USA) as follows:

Sample QC:

Total RNA samples were quantified using Qubit 2.0 Fluorometer (Life Technologies, Carlsbad, CA, USA) and RNA integrity was checked with 4200 TapeStation (Agilent Technologies, Palo Alto, CA, USA).

Library Preparation and Sequencing:

Samples were initially treated with TURBO DNase (Thermo Fisher Scientific, Waltham, MA, USA) to remove DNA contaminants. The next steps included performing rRNA depletion using QIAseq® FastSelect™−rRNA HMR kit (Qiagen, Germantown, MD, USA), which was conducted following the manufacturer's protocol. RNA sequencing libraries were constructed with the NEBNext Ultra II RNA Library Preparation Kit for Illumina by following the manufacturer's recommendations. Briefly, enriched RNAs are fragmented for 15 minutes at 94°C. First strand and second strand cDNA are subsequently synthesized. cDNA fragments are end repaired and adenylated at 3'ends, and universal adapters are ligated to cDNA fragments, followed by index addition and library enrichment with limited cycle PCR. Sequencing libraries were validated using the Agilent Tapestation 4200 (Agilent Technologies, Palo Alto, CA, USA), and quantified using Qubit 2.0 Fluorometer (ThermoFisher Scientific, Waltham, MA, USA) as well as by quantitative

PCR (KAPA Biosystems, Wilmington, MA, USA). The sequencing libraries were multiplexed and clustered on one lane of a flowcell. After
clustering, the flowcell was loaded on the Illumina HiSeq 4000 instrument according to manufacturer's instructions. The samples were sequenced using a 2x150 Pair-End (PE) configuration.

Initial Bioinformatics analysis:

Image analysis and base calling were conducted by the HiSeq Control Software (HCS). Raw sequence data (.bcl files) generated from Illumina HiSeq was converted into FASTQ files and de-multiplexed using Illumina's bcl2fastq 2.17 software. One mismatch was allowed for index sequence identification.

RNA-seq computational deconvolution of mouse and rat genomes:

RNA-seq reads in xenograft samples were deconvolved for identification of the species of origin following a method similar to that described by Wingrove et al.[187]. A catenated genome was formed by catenating the Rat (Rnor_6.0) and mouse (GRCmm28) genomes and gene annotations. Prior to alignment, reads were trimmed using Trim Galore and read quality was confirmed using fastQC. Trimmed reads were identified as originating from either rat or mouse by aligning reads against the catenated genome using STAR. Paired reads with both mates aligning uniquely to either the rat or mouse genome were separated by species and counted to gene annotations using featureCounts[188] for downstream differential expression analysis.

Within-species normalization of mapped reads and differential expression analysis were performed using the limma (version 3.50.0)[189] and edgeR (version 3.36.0)[190] packages in R following the procedure described in detail by Law et al.[191]. Prior to differential expression analysis, very low abundance genes were filtered using the filterByExpr function in edgeR using default parameters. Effective library sizes were normalized across conditions using the trimmed mean of M-values (TMM) normalization procedure. Differential expression analysis was performed on the filtered and normalized counts using the limma-voom linear modeling pipeline[192]. For experiments in which samples were paired by animal, animal ID was treated as an additional random effect in the linear model. Empirical Bayes smoothing was applied on both the linear model and fitted contrast coefficients using edgeR. False-discovery rates for differential expression at the gene-level were calculated using the Benjamini-Hochberg correction procedure with the toptable function in limma. Normalized transcript abundances are reported as the TMM-normalized counts-per-million obtained from the voom function in limma.

Gene set enrichment analysis was performed using GSEA software (Broad Institute, v 4.2.3)[193]. Genes were ranked by log-fold change and collapsed to human orthologs using the MDSig ensembl gene id orthologs chip platform (v 7.3). GSEA was performed using a pre-ranked analysis weighted by log-fold change against the C5 gene ontology collection (v 7.5). False-discovery rates were determined using 100,000 permutations.

For differential expression analysis between species (tumor and host), a modified normalization scheme was applied to account for differences in gene lengths and annotation depth between species, in addition to the standard normalization by effective

library size. Our method resembles that described by Oziolor, et al[194]. First, using reads that mapped uniquely to one species of the catenated genome, an intra-species TMM normalization was performed separately for host- and tumor-mapped reads. Length-corrected transcript abundances were calculated as reads per kilobase million (RPKM) in edgeR, and then converted to transcripts per million (TPM). Homolog pairs were obtained by querying the Ensembl database for linked rat (rattus norvegicus Ensembl release 100) and mouse (mus musculus Ensembl release 100) datasets using the getLDS function in biomaRt (v 2.50.3). Next, both gene sets were filtered to only those with rat/mouse homolog pairs, and the rat genes were mapped onto their corresponding mouse homologs. TPM abundances originating from both species were combined into a single data set, treating species of origin as a sample identifier, for all further analysis. To correct for differences in genome annotation depth between species, TPM values were normalized using the TMM method in edgeR. Homolog-wise differential expression analysis was performed between species using TMM-normalized, homolog-mapped TPM values as input into the limma-voom analysis pipeline (as above) in place of library-normalized counts. Prior to identifying top genes that were differentially expressed in the mouse tumor over the rat host, homolog pairs that exhibited zero read counts in the rat homolog for all of the samples were discarded, since these may reflect a limitation of the homolog mapping. Then, genes from mouse-core-mouse-rim were cross referenced with mouse-core-rat-core. Genes that were mouse-core vs. mouse-rim Log Fold Change ≥ 1 and FDR ≤ 0.01 and with detectable rat expression are shown in Fig 4C.

Real Time qPCR:

RNA from tumors and cell pellets were extracted using Qiagen RNeasy kit. RNA was reverse transcribed into cDNA using Superscript™ III First-Strand Synthesis System (Thermo Fisher Scientific Catalog number: 18080051) with equivalent amounts of RNA (1µg). cDNAs were mixed with indicated gene-specific primers listed and PowerUp SYBR Green Master Mix (Thermo Fisher Scientific Catalog number: A25741) and qRT-PCR was performed using an Applied Biosystems QuantStudio5 System.

Immunohistochemistry (IHC):

Tumors were sliced into ~5mm sections immediately after harvest, placed into histology cassettes(#15181701A), and fixed with 10% neutral buffered formalin solution (#HT501128) at room temperature for 5 days. Cassetted tumor sections were paraffin processed, embedded, and cut by Experimental Histopathology Core at Fred Hutchinson Cancer Research Center. Paraffin-embedded tumor slides were warmed in 56°C incubator for 20min in slide holder. Tissue was deparaffinized with Histo-Clear solution (#64111-04) twice for 5min each. Rehydration was performed by immersing the slides through the following solutions twice for 3min each: 100% ethanol, 95% ethanol, 70% ethanol, and deionized water. Heat-induced antigen retrieval was completed by incubating slides in pressure cooker at 6psi (~105°C) for 10-15min with Tris-EDTA (10mM Tris Base, 1mM EDTA, 0.05% Tween20, pH9.0) or sodium citrate (10mM sodium citrate, 0.05% Tween20, pH6.0) buffers. Endogenous peroxidase activity was blocked by 3% H_2O_2 in PBS for 20min. Fc receptor was blocked by Fc Receptor Blocker (#NB309) for 30min. Primary antibodies were diluted with blocking solution (2.5% host serum/1.25%BSA in PBS) and incubated on the slides at room temperature for 1hour.

Species specific ImmPRESS™ secondary antibodies [HRP polymer] from Vector Laboratories were applied directly onto the slides and incubated for 30min at room temperature. Substrate was developed using ImmPACT™ NovaRED™ HRP Substrate Kit (#SK-4805). Mayer's Hematoxylin (#26043-05) was used for counterstaining. Dehydration was performed by dipping the slides 10 times through the following solutions twice: 95% Ethanol and 100% Ethanol, followed by immersing the slides in Histo-clear solution twice for 2min each. CytoSeal 60 (#18006) was used to mount slides, then slides were scanned by Ventana DP 200 slide scanner.

Western Blotting:

Snap frozen tumors were milled into powder and 0.1g was dispensed to make lysate. Lysis buffer was prepared by diluting protease (#87785) and phosphatase (#78420) cocktail inhibitors 1:100 in 1X RIPA buffer (#9806S) and added into tumor powder (1mL of lysis buffer/0.1g of powder). The suspension was sonicated for 6 pulses with a probe sonicator (20%duty cycle, 30% amplitude), incubated at 4°C for 1 hour, and centrifuged at 14,000g for 10min to clear out insoluble substance. Protein concentration was quantified using Pierce BCA Assay Kit (#PI23225). Sample loading solution was prepared by combining tumor lysates (volume for 50ug of protein), 3.3uL of 10X Bolt reducing agent (#B0009), 8.25uL of 4X Bolt LDS buffer (#B0007), and MiliQ water to a final volume of 33uL. A Bolt™ 4-12%, Bis-Tris, 12-well, 1.0 mm Mini Protein Gel, (#NW04122BOX) was loaded with 30uL of sample loading solution per well and run at 100V for 20min and then at 170V for 40min using 1X Bolt MES SDS running buffer (#B0002). The protein transfer sandwich was assembled using Immobilon-FL PVDF Membrane (#IPFL07810) and run

at 15V for 1 hour with 1X Bolt transfer buffer (#BT00061) containing 10% methanol. The PVDF membrane was blocked with 3% BSA in TBS for 1 hour. Primary antibodies were diluted with 0.2% TBST and incubated overnight at 4°C. Species specific LI-COR 680 and 800 secondary antibodies were diluted 1:10,000 with 0.2% TBST plus 0.01% SDS and incubated for 1 hour at room temperature. The PVDF membrane was imaged with LiCor Odyssey CLx.

Angptl7 ELISA:

Sample loading solution was prepared by combining tumor lysate (volume for 300ug of protein) and sample diluent from the Mouse Angptl7 ELISA Kit ((#MBS612413) to a final volume of 400uL. 100uL of sample loading solution was loaded in each well for three replicates. Each well was incubated with biotinylated Anti-Mouse Angptl7 antibody, followed by Avidin-Biotin-Peroxidase Complex, and then Color Developing Reagent followed by Stop Solution per manufacturer instructions. O.D. absorbance was measured using a microplate reader at 450nm.

Angptl7 RNA ISH:

For in situ hybridization (ISH), formalin-fixed paraffin-embedded tissues were sectioned at 4 microns onto positively-charged slides and baked for 1 hour at 60°C. The slides were then dewaxed and stained on a Leica BOND Rx stainer (Leica, Buffalo Grove, IL) using Leica Bond reagents for dewaxing (Dewax Solution), antigen retrieval with Epitope Retrieval Solution 2 for 15 minutes at 95°C, protease digestion at 40C for 15 minutes and rinsing after each step (Bond Wash Solution). All other steps were performed at ambient

temperature. Staining was performed with RNAscope 2.5 LS Reagent Kit – BROWN (Cat. No. 322100) or RNAscope 2.5 LS Reagent Kit – RED (Cat. No. 322150). Species-specific probes were applied and incubated at 42C for 120 minutes. Probes used were as follows: RNAscope 2.5 LS Positive Control Probe Human PPIB (Cat. No. 313908), RNAscope 2.5 LS Positive Control Probe Mouse PPIB (Cat. No. 313918), RNAscope 2.5 LS Negative Control Probe dapB (Cat. No. 312038), RNAscope 2.5 LS Human Angptl7 (Cat. No. 552818), RNAscope 2.5 LS Mouse Angotl7 (Cat. No. 552528). Chromogenic staining was performed using BOND Polymer Refine Detection (Cat. No. DS9800) or BOND Polymer Refine Red Detection (Cat. No. DS9390). After staining, slides were removed from the stainer, dehydrated and coverslipped. Slides stained with the Brown kit were coverslipped with Epredia Cytoseal XYL (Cat. No. 8312-4) and slides stained wit the Red kit were coverslipped with Axell Crystal Mount (Cat. No. BMDM02).

QuPath quantification of RNA ISH:

RNAscope images were opened in QuPath[195]. Thresholds were created to identify tumor area and necrotic area by eye, verified to be accurate in test images, and applied to demarcate necrotic zones. Angptl7-expressing cells were identified using positive cell detection. The distance to annotation 2d feature was used to determine the distance between cells and the nearest necrotic border and cells and nearest tumor border. This process was automated in QuPath for consistent analysis across images.

Necrosis measurements:

Tumor necrosis measurements were determined based on Hematoxylin & Eosin (H&E) or 2,3,5-triphenyltetrazolium chloride (TTC) assay. For H&E staining, tumors were sliced into 2-3 ~5mm slices by scalpel, fixed for 5 days in 10% formalin at 4°C, rocking before being sectioned and stained with hematoxylin and eosin. For the TTC assay, tumors were sliced into 2-3 ~5mm slices and stained with 1g/100ml tetrazolium salt in a 7.4pH buffer with 77.4% NaH_2PO_4 (0.1 M) and 22.6% Na_2HPO_4 (0.1M) mix, at 37°C for 20 mins, rocking. Tumor slices were then fixed with 10% formalin for 20 mins before being visualized. In the TTC assay, the TTC compound is reduced to a red TPF (1,3,5-triphenylformazan) compound in live tissues due to dehydrogenase activity. White areas therefore indicate necrotic tissue, and red areas are viable regions.

Spatial enrichment localization score:

For each spot x, the spatial enrichment score (SES) was computed as Dt/(Dn+Dt) where Dn equals the distance between spot x and the nearest necrotic border and Dt equals the distance between spot x and the nearest tumor border (Dt). Accordingly, SES(x) varies from 0 to 1: equal to 0 for perfect localization to the tumor border, and 1 for perfect localization to the necrotic border. Distances calculated from QuPath were exported to R and analyzed using a custom script. A non-parametric Kruskal-Wallis test was applied to evaluate statistical significance between different SES distributions.

LC/MS plasma proteomics

Sample Preparation: Each plasma sample was depleted of high-abundance proteins by injecting 80 µL of the sample onto a Michrom Bioresources Paradigm HPLC equipped

with an Agilent human MARS-6 depletion column. Unbound material eluting from the column, as observed on a UV detector, was collected and the protein concentration was determined. The volume corresponding to 100 µg of protein was subjected to the reduction of disulfide bonds by adding TCEP (tris(2-carboxyethyl)phosphine to a final concentration of 5 mM and incubating at room temperature with vortexing for 15 min. Protein alkylation was carried out by adding 2-chloroacetamide to a final concentration of 10 mM and incubating at room temperature for 30 min. The volume of each sample was reduced to approximately 100 µL by vacuum centrifugation and methanol/chloroform precipitation was carried out. Protein pellets were washed with methanol and resuspended in 50 mM HEPES pH 8.7. Proteolytic digestion was initiated with the addition of 1 µg of Lys-C and incubating at room temperature with low vortexing for 2 hours, followed by the addition of 1 µg of trypsin and incubating overnight at 37 °C on an orbital shaker set at 700 rpm.

TMT Labeling: ThermoScientific TMTpro-16plex reagent was brought to room temperature and resuspended in 20 µL of anhydrous acetonitrile and vortexed for 15 min. Labeling was carried out by adding 20 µL of each TMT reagent to its assigned sample and vortexing the samples occasionally at room temperature for 1 hour. A “label check” was performed by combining 2 µL from each labeled sample into one tube, removing the acetonitrile by vacuum centrifugation, desalting the sample on a Harvard Apparatus C18 ultra-micro spin column, and analyzing the desalted TMT-labeled peptides by LC-ESI-MS/MS. After data analysis (see below), the peptide to spectrum match (PSM) results were analyzed and labeling efficiency was determined to be greater than 98%. After this labeling check, hydroxlyamine was added to each labeled sample to a concentration of

0.5% in order to fully quench the labeling reaction. All samples were combined equally by correcting for the total protein abundances measured for each sample in the labeling check analysis. The equalized pool was subjected to vacuum centrifugation to remove acetonitrile and then desalted on a Waters SepPack C18 (3cc, 200 mg) cartridge. The desalted elution was split into equal fractions and taken to dryness. One of the fractions was injected onto a ThermoScientific Vanquish HPLC equipped with an Agilent 2.1 mm x 150 mm C18 Extend column and fractionated into a 96-well plate using basic reverse-phase conditions. The 96 fractions were concatenated into 24 pools (pool 1: fractions 1, 25, 49, 73; pool 2: fractions 2, 26, 50, 74; etc.) that were taken to dryness and each pool was analyzed by LC-ESI-MS/MS.

LC-ESI-MS/MS: The generated basic reverse phase fractions were brought up in 20 µL of 2% acetonitrile in 0.1% formic acid and 5 µL was analyzed by LC/ESI MS/MS with a Thermo Scientific Easy1200 nLC (Thermo Scientific, Waltham, MA) coupled to a tribrid Orbitrap Eclipse with FAIMS (field asymmetric ion mobility spectrometry) mass spectrometer (Thermo Scientific, Waltham, MA). In-line de-salting was accomplished using a reversed-phase trap column (100 µm × 20 mm) packed with Magic C_{18}AQ (5-µm, 200 Å resin; Michrom Bioresources, Auburn, CA) followed by peptide separations on a reversed-phase column (75 µm × 270 mm) packed with ReproSil-Pur C_{18}AQ (3-µm, 120 Å resin; Dr. Maisch, Baden-Würtemburg, Germany) directly mounted on the electrospray ion source. A 120-minute gradient from 4% to 44% B (80% acetonitrile in 0.1% formic acid) at a flow rate of 300 nL/minute was used for chromatographic separations. A spray voltage of 2300 V was applied to the electrospray tip and the FAIMS source used varied compensation voltages of -40, -60, -80 while the Orbitrap Eclipse instrument was

operated in the data-dependent mode. MS survey scans were in the Orbitrap (Normalized AGC target value 300%, resolution 120,000, and max injection time 50 ms) with a 3 sec cycle time and MS/MS spectra acquisition were detected in the Orbitrap (Normalized AGC target value of 250%, resolution 50,000 and max injection time 100 ms) using HCD activation with a normalized collision energy of 35%. Selected ions were dynamically excluded for 60 seconds after a repeat count of 1.

Data Analysis**:** Data analysis was performed using Proteome Discoverer 2.4 (Thermo Scientific, San Jose, CA). The data were searched against a Uniprot Human database (UP000005640, Dec 1, 2019) that included common contaminants (cRAPome 2015). Searches were performed with settings for the proteolytic enzyme trypsin. Maximum missed cleavages were set to 2. The precursor ion tolerance was set to 10 ppm and the fragment ion tolerance was set to 0.6 Da. Dynamic peptide modifications included oxidation (+15.995 Da on M). Dynamic modifications on the protein terminus included acetyl (+42.-11 Da on N-terminus), Met-loss (-131.040 Da on M) and Met-loss+Acetyl (-89.030 Da on M) and static modifications TMTpro (+304.207 on N-terminus and K), carbamidomethyl (+57.021 on C). Sequest HT was used for database searching. All search results were run through Percolator for peptide validation and results were filter to a 1% false discovery rate. To delineate differential expression proteins, both pairwise two-sample *t* tests and Wilcoxon rank-sum test were conducted (R package).

Quantification and Statistical Analysis

Bars are presented as mean ± standard deviation. Graphs were created and statistical tests conducted in GraphPad Prism 8. Non-parametric tests were used when data were

not normally distributed or when the median was a better representation of the sample than the mean. For animal experiments, each animal was considered a biological replicate. For in vitro experiments, experiments using cell lines on different days were considered biological replicates. P-values denoted as follows: * < 0.05, ** < 0.01, *** < 0.001, **** < 0.0001.

2.6.2 *Key resource table*

Regent or Resource	**Source**	**Identifier**
Antibodies		
Goat Angiopoietin-like 7 (Mouse)	R&D Systems	AF4960
Rabbit VE-Cadherin	Abcam	ab205336
Mouse α-Smooth Muscle Actin	Sigma	A5228
Syrian hamster Podoplanin	ThermoFisher	14-5381-82
Mouse Pan-Keratin (C11) (Mouse) (Alexa Fluor® 647 Conjugate)	Cell Signaling Technology	4528S
Mouse GAPDH	ProteinTech	60004
Mouse Beta Actin	Abcam	ab6276
Chemicals, Peptides, and Recombinant Proteins		
RNAscope® 2.5 LS Probe - Mm-Angptl7	ACD Bio-Techne	552828
RNAscope 2.5 LS Probe - Hs-ANGPTL7	ACD Bio-Techne	552818
Critical Commercial Assays		

Mouse ANGPTL7 ELISA Kit	MyBioSource	MBS1752641
Experimental Models: Cell lines		
Human: 293FT	ThermoFisher Scientific	R70007
Mouse: 4T1	ATCC	CRL-2539
Mouse: 4T1-cyto-GFP	Gift from Cyrus Ghajar	N/A
Experimental Models: Organisms/Strains		
Mouse: FVB/NJ	The Jackson Laboratory	001800
Mouse: NOD.Cg-Prkdcscid Il2rgtm1Wjl/SzJ	The Jackson Laboratory	005557
Rat: SRG Oncorat	Charles River	SRG Strain 007
Oligonucleotides		
PsPax2	A gift from Didier Trono	Addgene #12260
MD2.G	A gift from Didier Trono	Addgene #12259
shCtrl Non-targeting #4 pZIP-mCMV-mCherry-Blast (non-targeting control)	transOMIC	TLMSU1451
pZIP-mCMV-mCherry-Blasticidin-Mouse-shAngptl7 (Angptl7 knockdown 1)	transOMIC	Ultra-3367559
pZIP-mCMV-mCherry-Blasticidin-Mouse-	transOMIC	Ultra-3367561

shAngptl7 (Angptl7 knockdown 2)		
pZIP-mCMV-mCherry-Blasticidin-Mouse-shAngptl7 (Angptl7 knockdown 3)	transOMIC	Ultra-344221
rLV.EF1.AcGFP1-Mem-9	Takara BIO INC.	0019VCT
Software		
GraphPad Prism 9	Graphpad Software	https://www.graphpad.com/scientific-software/prism/
FIJI v2.0.0-rc-69/1.52p	Schindelin et al., 2012[196]	https://fiji.sc/
R v3.6.1	R Core Team	https://www.r-project.org/
Metascape	Zhou et al., 2019[197]	https://metascape.org/
R v 4.1.1	R Core Team	https://www.r-project.org/
STAR v. 2.7.3	Dobin, et al., 2013[198]	https://github.com/alexdobin/STAR
limma v. 3.5	Ritchie, et al., 2015[189]	https://bioconductor.org/packages/release/bioc/html/limma.html
edgeR v 3.36.0	Robinson, et al. 2010[190]	https://bioconductor.org/packages/release/bioc/html/edgeR.html
biomaRt v. 2.50.3	Durinck, et al. 2009[199]	https://bioconductor.org/packages/release/bioc/html/biomaRt.html
Rsubread v. 2.4.3	Liao, et al., 2019[200]	https://bioconductor.org/packages/release/bioc/html/Rsubread.html
FastQC v. 0.11.9	Babraham Bioinformatics	https://www.bioinformatics.babraham.ac.uk/projects/fastqc/
Trim Galore v. 0.6.5	Babraham Bioinformatics	https://www.bioinformatics.babraham.ac.uk/projects/trim_galore/
SAMtools v. 1.11	Danececk, et al., 2021[201]	https://github.com/samtools/samtools
GSEA v. 4.2.3	Broad Institute	https://www.gsea-msigdb.org/gsea/index.jsp

2.7 CHAPTER 2 FIGURES

Figure 1

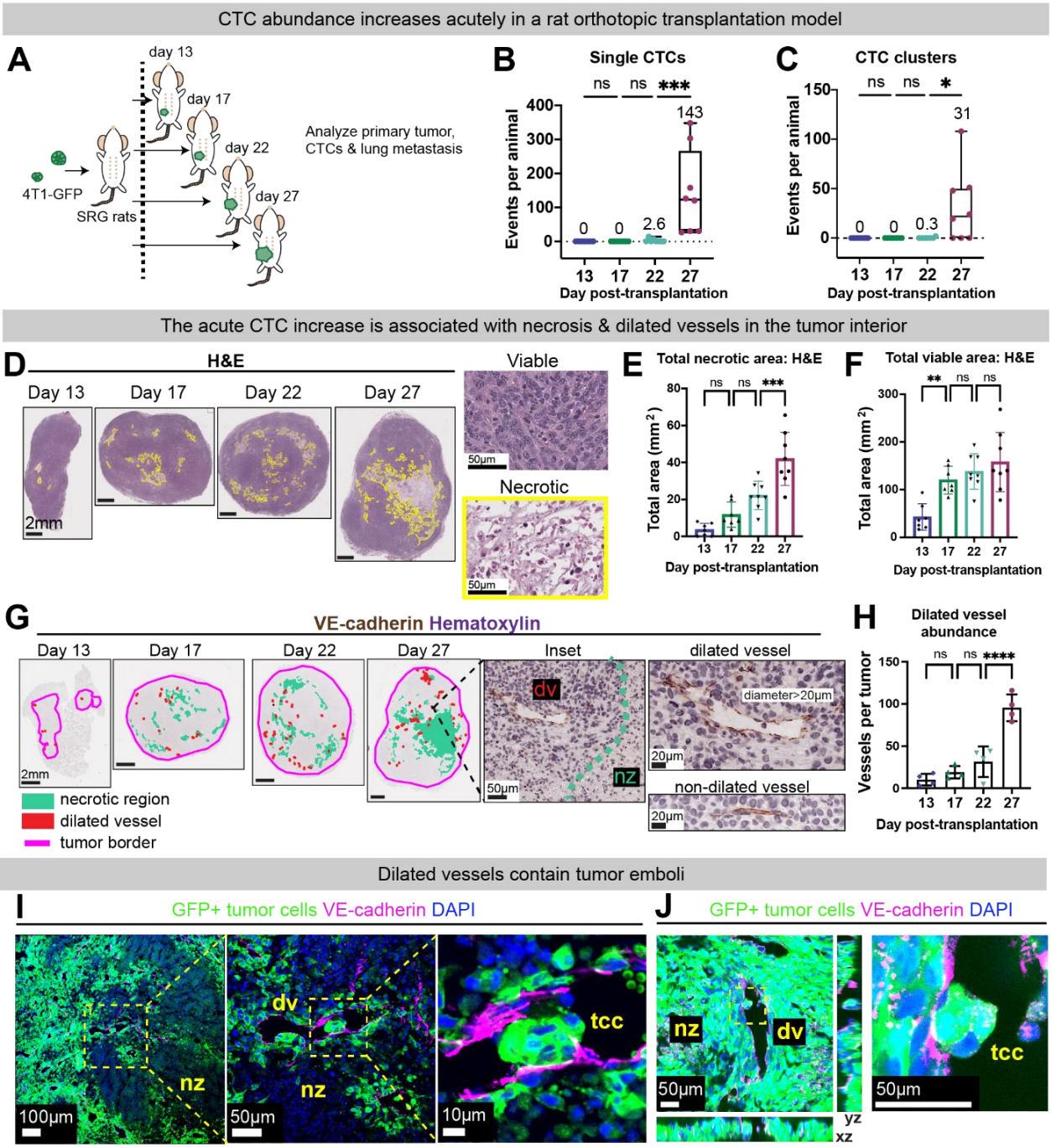

Figure 1: CTC transition is temporally associated with tumor necrosis, dilated vessels, and peri-necrotic intravascular emboli.

1A) Experimental schema. 4T1 mouse mammary tumor cells labeled with cytoplasmic GFP (4T1-GFP) were orthotopically transplanted into a single #4 mammary fat pad of SRG rats. Animals were sacrificed at day 13 (n=7), 17 (n=7), 22 (n=8), and 27 (n=8) post-transplantation.

1B-C) Single CTC and CTC clusters per animal. Box plots shown with mean values labeled.

1D) Representative hematoxylin and eosin (H&E) stains of day 13 to 27 rat tumors. Left: Necrotic region indicated with yellow border. Right: Insets of necrotic and non-necrotic regions from a day 27 tumor.

1E-F) Total necrotic area and total viable area were determined by H&E. Mean ±SD.

1G) Representative day 13 to day 27 rat tumors stained for VE-cadherin (DAB) and counterstained with hematoxylin. Left: low power views. Necrotic regions shown in turquoise, dilated vessels in red, and tumor border in magenta. Right: example of a dilated and non-dilated vessel. Dv= dilated vessel. Nz= necrotic zone.

1H) Number of VE-cadherin+ dilated blood vessels. Mean ±SD.

1I-J) Representative immunofluorescent images of GFP+ tumor emboli inside VE-cadherin+ blood vessel from thin (10μm) and thick (30μm) tumor sections. I) Left: low power image of peri-necrotic zone. i and ii: insets showing higher magnification of tumor cell cluster (tcc) within a dilated vessel (dv). J) Confocal images from z-stack showing tumor cell cluster (tcc) within dilated vessel (dv). Xy, xz, and yz cross-sections shown.

Magenta: VE-cadherin; Red: 594 conjugated lectin; Blue: DAPI; Green: tumor cells expressing GFP (membrane GFP in I & cytoplasmic GFP in J). nz = necrosis.

P-values for B-C, E-F, and H determined by one-way ANOVA.

Figure 2

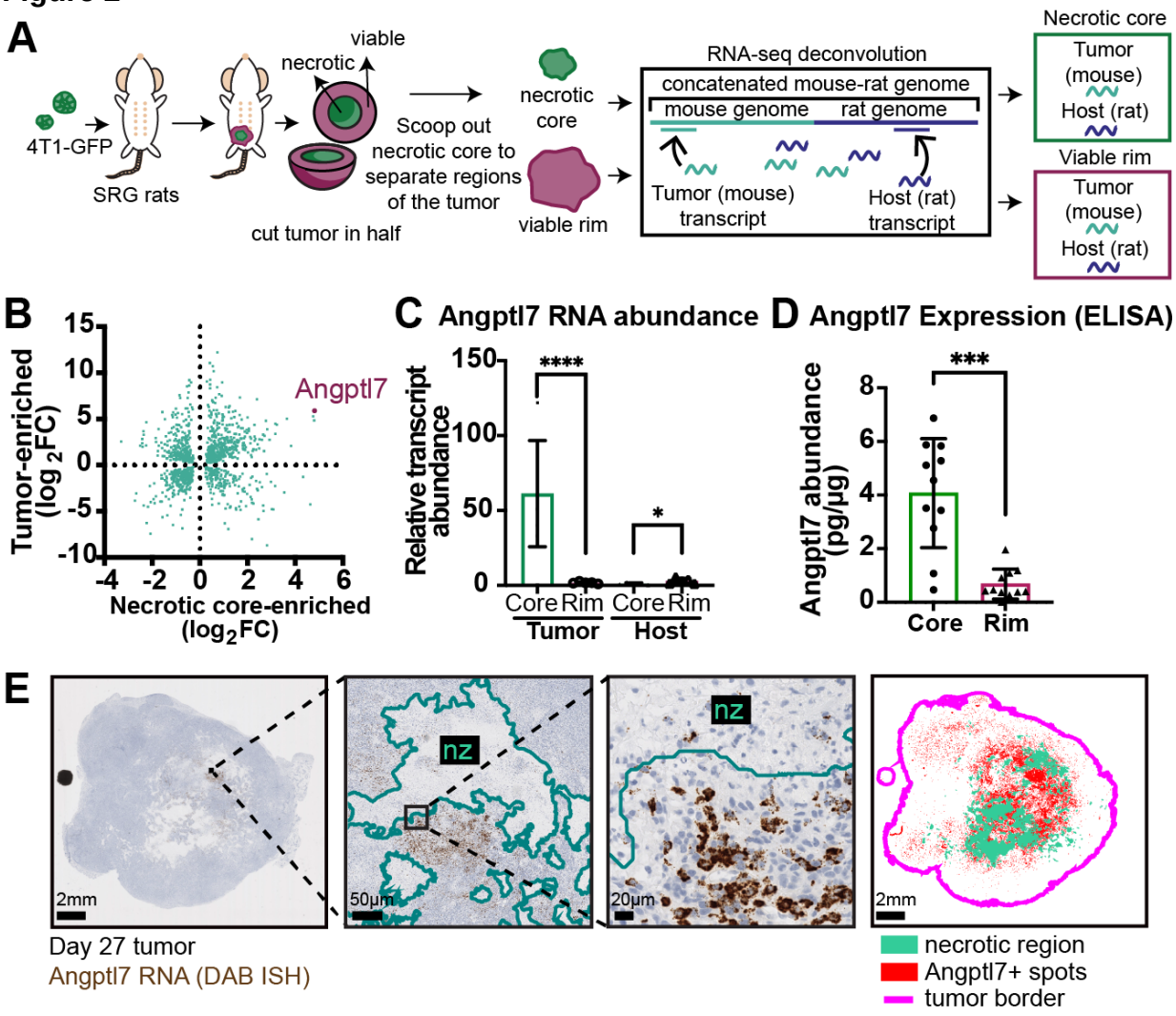
A
4T1-GFP
SRG rats
viable
necrotic
cut tumor in half
Scoop out necrotic core to separate regions of the tumor
necrotic core
viable rim
RNA-seq deconvolution
concatenated mouse-rat genome
mouse genome
rat genome
Tumor (mouse) transcript
Host (rat) transcript
Necrotic core
Tumor (mouse)
Host (rat)
Viable rim
Tumor (mouse)
Host (rat)
B
Angptl7
Tumor-enriched (log2FC)
Necrotic core-enriched (log2FC)
C Angptl7 RNA abundance
Relative transcript abundance
****
*
Core Rim Core Rim
Tumor
Host
D Angptl7 Expression (ELISA)
Angptl7 abundance (pg/µg)
***
Core
Rim
E
nz
nz
2mm
50µm
20µm
2mm
Day 27 tumor
Angptl7 RNA (DAB ISH)
necrotic region
Angptl7+ spots
tumor border

Figure 2: Angptl7 is a tumor-derived, necrotic core-enriched transcript localized to the peri-necrotic region of breast tumor.

2A) Experimental schema. 4T1-GFP tumor cells were orthotopically transplanted into a single fat pad of SRG rats and collected between day 27 to day 30 (n=5 animals). The harvested tumors were cut in half, and macrodissected to separate the necrotic core region from the non-necrotic rim of the primary tumors. RNA was extracted and subjected to next-generation sequencing. Sequences were aligned to concatenated rat-mouse combined genome, and mouse and rat genes were deconvoluted from each other.

2B) Mouse orthologs were identified for all rat genes and the relative RNA abundance per gene between tumor and host compartments was determined. The plot shows all genes with both differential enrichment for core:rim and for tumor:host with FDR ≤ 0.01.

2C) Relative RNA abundance of *Angptl7* based on RNA-seq. Average expression and q-value (FDR) from multiple comparisons indicated on the graph.

2D) ELISA quantification of Angptl7 protein abundance of the necrotic core and non-necrotic rim regions of 4T1 tumors. Student t-test. Mean ±SD.

2E) Representative image of Angptl7 RNA in situ hybridization (ISH) of day 27 4T1 tumors. Left: raw Angptl7 RNA ISH (brown). Right: Detection by QuPath. Red: positive detection of Angptl7+ cells, turquoise: necrotic region, pink: tumor border.

Figure 3

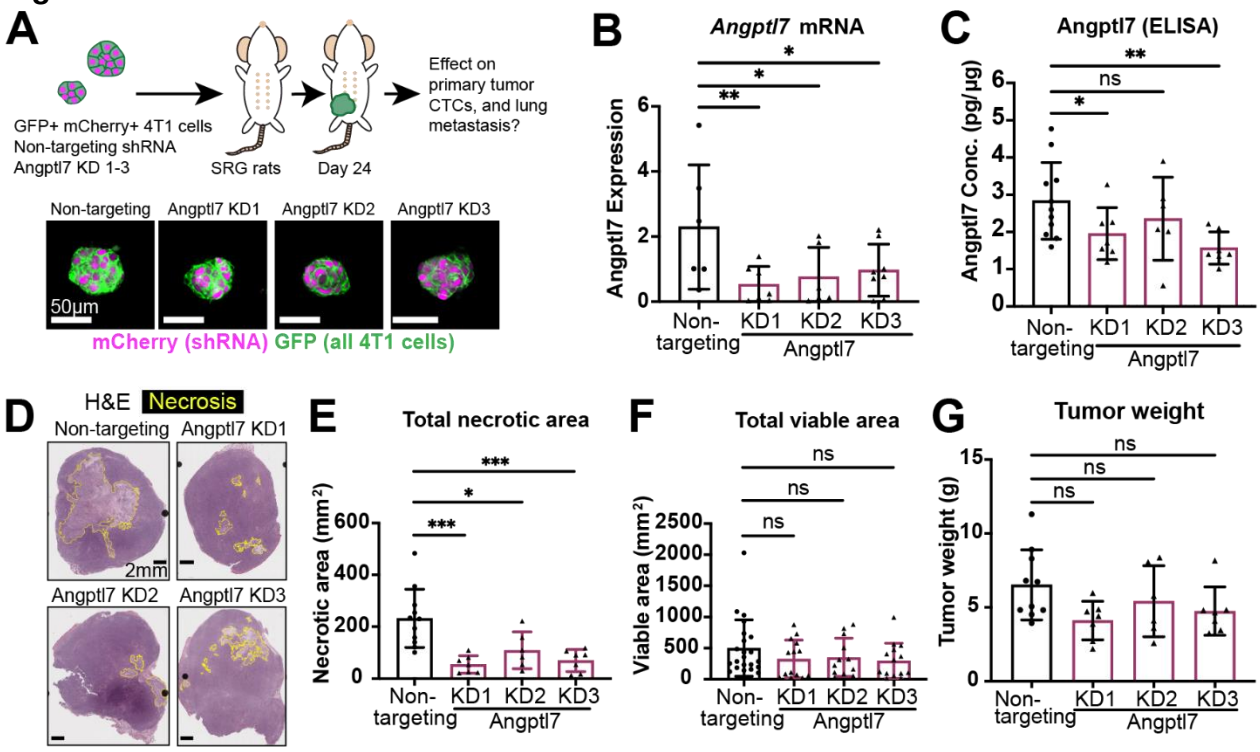
A
GFP+ mCherry+ 4T1 cells
Non-targeting shRNA
Angptl7 KD 1-3
SRG rats
Day 24
Effect on primary tumor CTCs, and lung metastasis?
Non-targeting
Angptl7 KD1
Angptl7 KD2
Angptl7 KD3
50μm
mCherry (shRNA) GFP (all 4T1 cells)
B
Angptl7 mRNA
Angptl7 Expression
Non-targeting
KD1
KD2
KD3
Angptl7
C
Angptl7 (ELISA)
Angptl7 Conc. (pg/μg)
ns
D
H&E
Necrosis
2mm
E
Total necrotic area
Necrotic area (mm²)
F
Total viable area
Viable area (mm²)
G
Tumor weight
Tumor weight (g)

Figure 3: Suppression of Angptl7 normalizes tumor necrosis.

3A) Experimental schema. 4T1 tumor cells labeled with membrane GFP and transduced with Angplt7 shRNA or non-targeting control were orthotopically transplanted into a single mammary fat pad of SRG rats. shRNA contained an mCherry tag, so cells expressing shRNA have cytoplasmic mCherry label. Blood, tumor, and lungs were collected. Non-targeting control (n=11), Angptl7 knockdown KD1 (n=7), Angptl7 KD2 (n=6), Angptl7 KD3 (n=7).

3B) In vivo knockdown confirmation by qPCR based on tumor core.

3C) ELISA confirmation by in vivo knockdown. Lysates were made from tumor necrotic core from Angptl7 knockdown and non-targeting control tumor cell transplantation experiments.

3D) Representative hematoxylin and eosin (H&E) staining of primary tumors for Angptl7 knock down tumors and non-targeting control. Yellow borders indicate the necrotic regions.

3E-F) Total necrotic area and total viable area based on H&E staining of Angptl7 KD and non-targeting control tumor.

3G) Tumor weight of Angptl7 KD and non-targeting control tumor.

All graphs shown display mean ±SD. Mean values shown on graphs. P-values for B-C determined by Mann-Whitney test; for E-G determined by ANOVA.

Figure 4

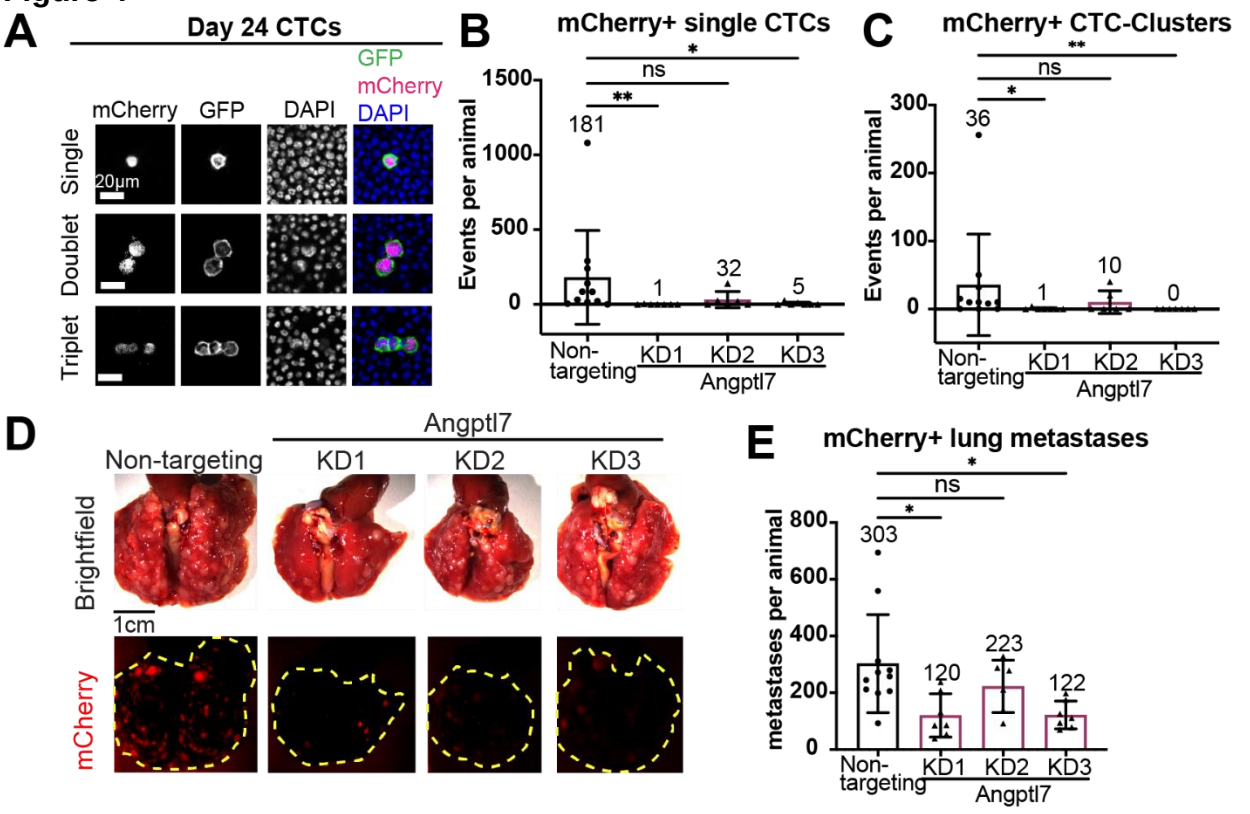
A
Day 24 CTCs
GFP
mCherry
DAPI
mCherry
GFP
DAPI
Single
Doublet
Triplet
20μm
B
mCherry+ single CTCs
Events per animal
1500
1000
500
0
*
ns
**
181
1
32
5
Non-targeting
KD1
KD2
KD3
Angptl7
C
mCherry+ CTC-Clusters
Events per animal
300
200
100
0
**
ns
*
36
1
10
0
Non-targeting
KD1
KD2
KD3
Angptl7
D
Angptl7
Non-targeting
KD1
KD2
KD3
Brightfield
1cm
mCherry
E
mCherry+ lung metastases
metastases per animal
800
600
400
200
0
*
ns
*
303
120
223
122
Non-targeting
KD1
KD2
KD3
Angptl7

Figure 4: Suppression of Angptl7 reduces CTC abundance and distant lung metastases.

4A) Representative images of single CTCs and CTC clusters from non-targeting control. Cells are mCherry-positive if they express shRNAs. 4T1 cells are labeled by membrane GFP. DAPI marks nuclei.

4B-C) mCherry-positive single CTC and CTC cluster abundance in Angptl7 knockdown and non-targeting control.

4D) Representative images of lung metastases from Angptl7 knockdown or non-targeting control transplantation (4T1 cells). Cells expressing the shRNAs express mCherry.

4E) mCherry-positive lung metastasis count for Angptl7 knockdown and non-targeting control. Mean ±SD.

All graphs shown display mean ±SD. Mean values shown on graphs. P-values for B-C, E determined by ANOVA.

Figure 5

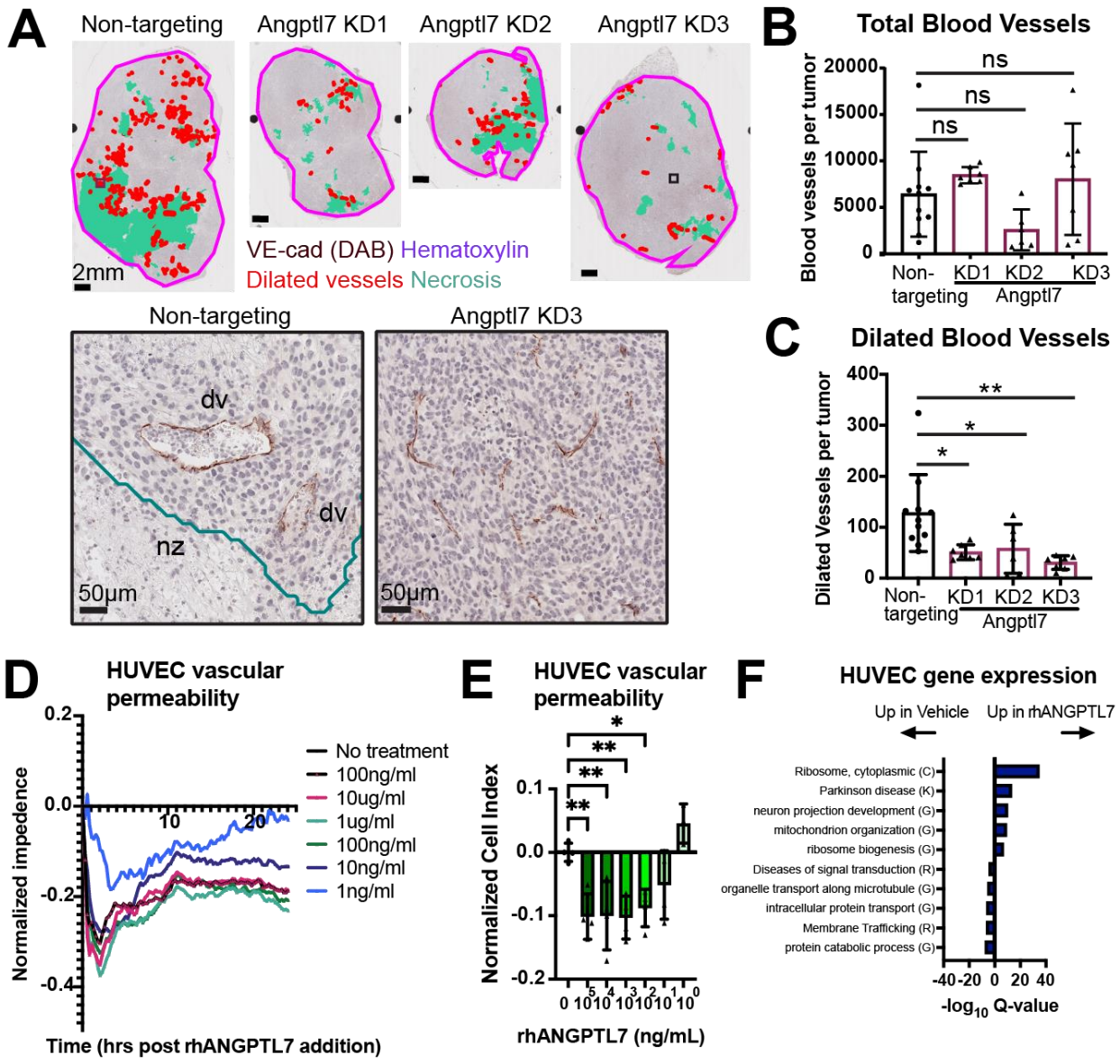
A
Non-targeting
Angptl7 KD1
Angptl7 KD2
Angptl7 KD3
2mm
VE-cad (DAB) Hematoxylin
Dilated vessels Necrosis
Non-targeting
Angptl7 KD3
dv
dv
nz
50μm
50μm
B
Total Blood Vessels
Blood vessels per tumor
20000
15000
10000
5000
0
ns
ns
ns
Non-targeting
KD1
KD2
KD3
Angptl7
C
Dilated Blood Vessels
Dilated Vessels per tumor
400
300
200
100
0
**
*
*
Non-targeting
KD1
KD2
KD3
Angptl7
D
HUVEC vascular permeability
Normalized impedence
0.2
0.0
-0.2
-0.4
10
20
No treatment
100ng/ml
10ug/ml
1ug/ml
100ng/ml
10ng/ml
1ng/ml
Time (hrs post rhANGPTL7 addition)
E
HUVEC vascular permeability
Normalized Cell Index
0.1
0.0
-0.1
-0.2
*
**
**
**
0 10^5 10^4 10^3 10^2 10^1 10^0
rhANGPTL7 (ng/mL)
F
HUVEC gene expression
Up in Vehicle
Up in rhANGPTL7
Ribosome, cytoplasmic (C)
Parkinson disease (K)
neuron projection development (G)
mitochondrion organization (G)
ribosome biogenesis (G)
Diseases of signal transduction (R)
organelle transport along microtubule (G)
intracellular protein transport (G)
Membrane Trafficking (R)
protein catabolic process (G)
-40 -20 0 20 40
-log10 Q-value

Figure 5: Angptl7 regulates blood vessel morphology and vascular permeability.

5A) Representative images of dilated VE-cadherin+ blood vessels Angptl7 knockdown and non-targeting control tumors. Immunohistochemistry for VE-cadherin (DAB) (brown) counterstained with hematoxylin. Red: dilated vessels, turquoise: necrotic region, pink: tumor border. Insets: vessel morphology in non-targeting control and Angptl7 knockdown.

5B) Number of total VE-cadherin+ blood vessels in the Angptl7 knockdown and non-targeting control tumors. Mean ±S D.

5C) Number of dilated VE-cadherin+ blood vessels in the Angptl7 knockdown and non-targeting control tumors. Mean ±S D.

5D-E) Human endothelial cell (HUVEC) vascular permeability in response to ANGPTL7 recombinant protein (rhANGPTL7). Vascular permeability was measured as normalized impedance over time. n=4 biological replicates. Shown is mean temporal response (D) and normalized cell index at 1 hr (E).

5F) Metascape analysis of gene enrichment. HUVEC cells were treated with rhANGPTL7 for 24 hrs. RNA-seq identified 741 upregulated genes and 500 genes downregulated with rhANGPTL7 treatment with p-value cutoff ≤ 0.01. Enrichments reported as -log Q-values.

All P-values determined by one-way ANOVA.

Figure 6

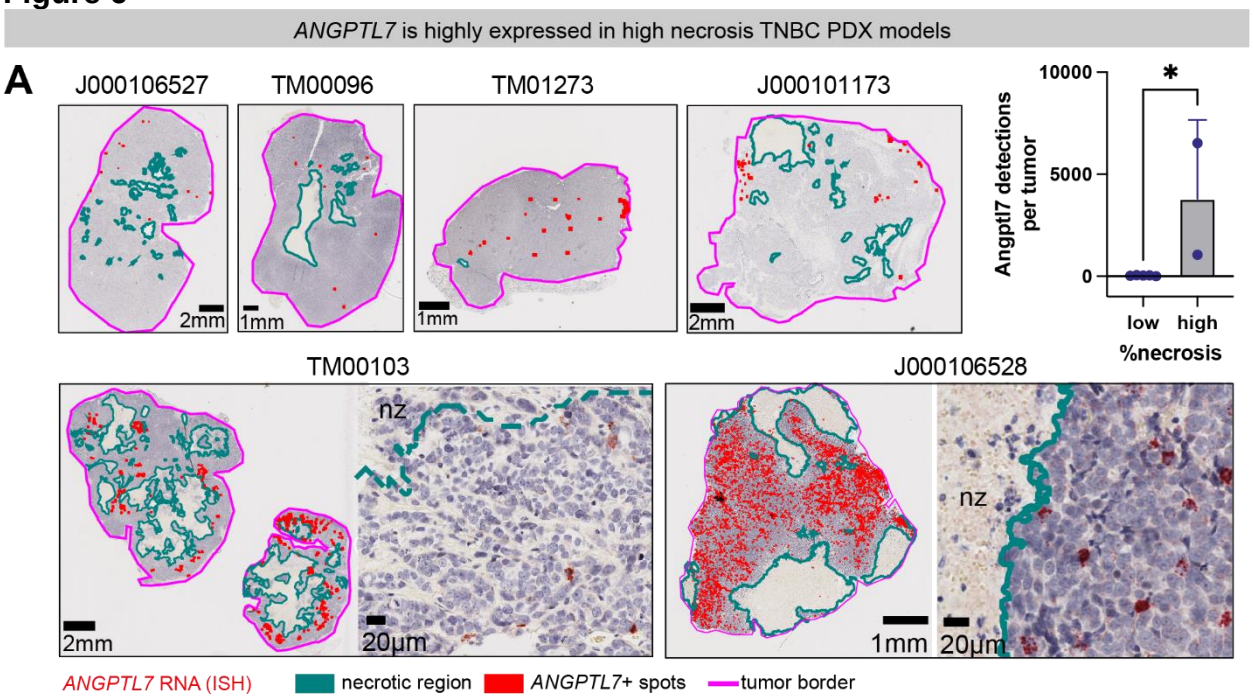
ANGPTL7 is highly expressed in high necrosis TNBC PDX models
A
J000106527
TM00096
TM01273
J000101173
2mm
1mm
1mm
2mm
Angptl7 detections per tumor
10000
5000
0
*
low
high
%necrosis
TM00103
J000106528
nz
nz
2mm
20µm
1mm
20µm
ANGPTL7 RNA (ISH)
necrotic region
ANGPTL7+ spots
tumor border

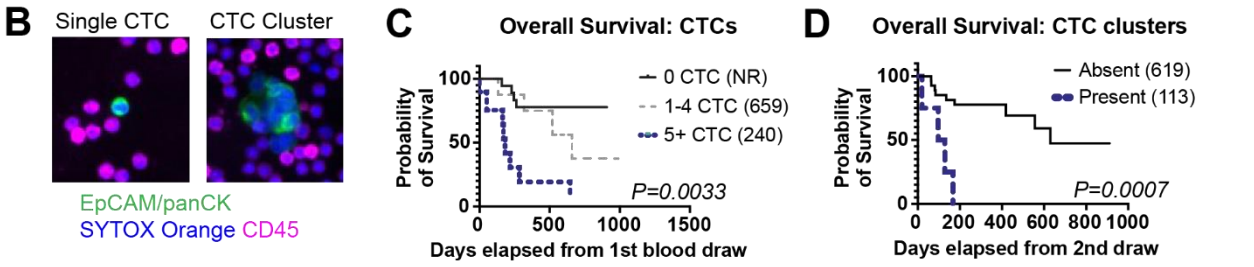
Markers of necrosis are associated with high CTC counts in patients with metastatic breast cancer
B
Single CTC
CTC Cluster
EpCAM/panCK
SYTOX Orange CD45
C
Overall Survival: CTCs
Probability of Survival
100
50
0
0 CTC (NR)
1-4 CTC (659)
5+ CTC (240)
P=0.0033
0
500
1000
1500
Days elapsed from 1st blood draw
D
Overall Survival: CTC clusters
Probability of Survival
100
50
0
Absent (619)
Present (113)
P=0.0007
0
200
400
600
800
1000
Days elapsed from 2nd draw

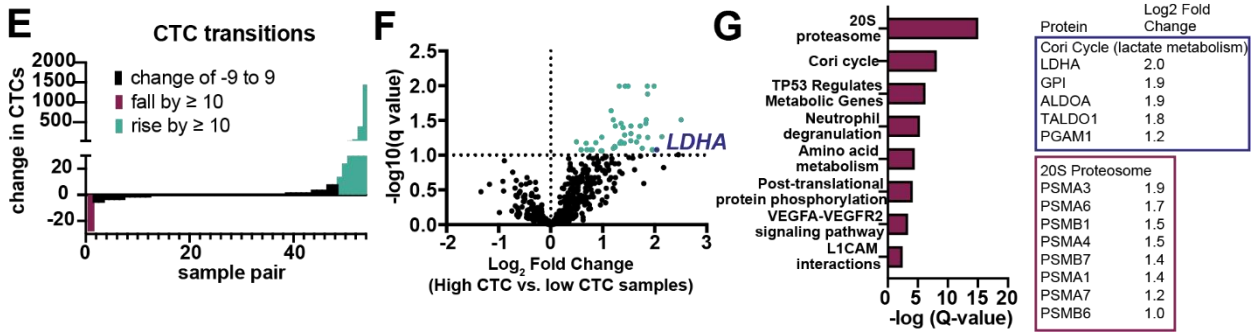
E
CTC transitions
change in CTCs
2000
1500
1000
500
20
0
-20
change of -9 to 9
fall by ≥ 10
rise by ≥ 10
0
20
40
sample pair
F
-log10(q value)
2.5
2.0
1.5
1.0
0.5
0.0
-2
-1
0
1
2
3
LDHA
Log2 Fold Change
(High CTC vs. low CTC samples)
G
20S proteasome
Cori cycle
TP53 Regulates Metabolic Genes
Neutrophil degranulation
Amino acid metabolism
Post-translational protein phosphorylation
VEGFA-VEGFR2 signaling pathway
L1CAM interactions
0
5
10
15
20
-log (Q-value)
Protein
Log2 Fold Change
Cori Cycle (lactate metabolism)
LDHA 2.0
GPI 1.9
ALDOA 1.9
TALDO1 1.8
PGAM1 1.2
20S Proteosome
PSMA3 1.9
PSMA6 1.7
PSMB1 1.5
PSMA4 1.5
PSMB7 1.4
PSMA1 1.4
PSMA7 1.2
PSMB6 1.0

Figure 6: *ANGPTL7* is expressed in high necrosis human triple-negative breast cancers and necrosis markers correlate with CTC dissemination in breast cancer patients.

6A) *ANGPTL7* RNA ISH performed on tumor sections from human breast PDX tumors transplanted into NSG mice. All tumor models were invasive ductal carcinomas and confirmed triple-negative for ER, PR and HER2 on PDX tumor sections. Qupath detections shown. Turquoise: necrotic region, red: positive *ANGPTL7* positive detections, pink: tumor border. Insets show raw *ANGPTL7* RNA ISH in red. Right: bar graph comparing tumors with low necrosis (5 sections from 4 models) and high necrosis (2 sections from 2 models). High necrosis defined as >15% necrosis by area. P-value determined by unpaired t-test.

6B) Representative single CTC and CTC cluster from clinical vignette in Fig. S6. EpCAM/pan-CK, epithelial cells; CD45, immune cells; SYTOX Orange, nucleic acid stain.

6C) Overall survival according to CTC enumeration at baseline. Median overall survival reported in parentheses. NR = not reached. P-value determined by Mantel-Cox log-rank test.

6D) Overall survival according to presence or absence of CTC clusters. Landmark analysis from 2nd blood draw was performed. Median overall survival reported in parentheses. P-value determined by Mantel-Cox log-rank test.

6E) Waterfall plot showing changes in CTC abundance between time points, sorted by magnitude.

6F) Tandem-mass tag mass spectrometry of high vs. low CTC samples. Volcano plot shows the 46 plasma proteins enriched in 3 high CTC samples compared with 13 low CTC samples. Proteins with Q-values less than 10%. False discovery rate determined by two-stage set-up method by Benjamini, Krieger, and Yekutieli.

6G) Metascape analysis of CTC-associated proteins reported by -log Q-value. Right: Proteins with fold-enrichment that make up core enrichments for Cori Cycle and 20S proteasome.

Supplementary Figure 1

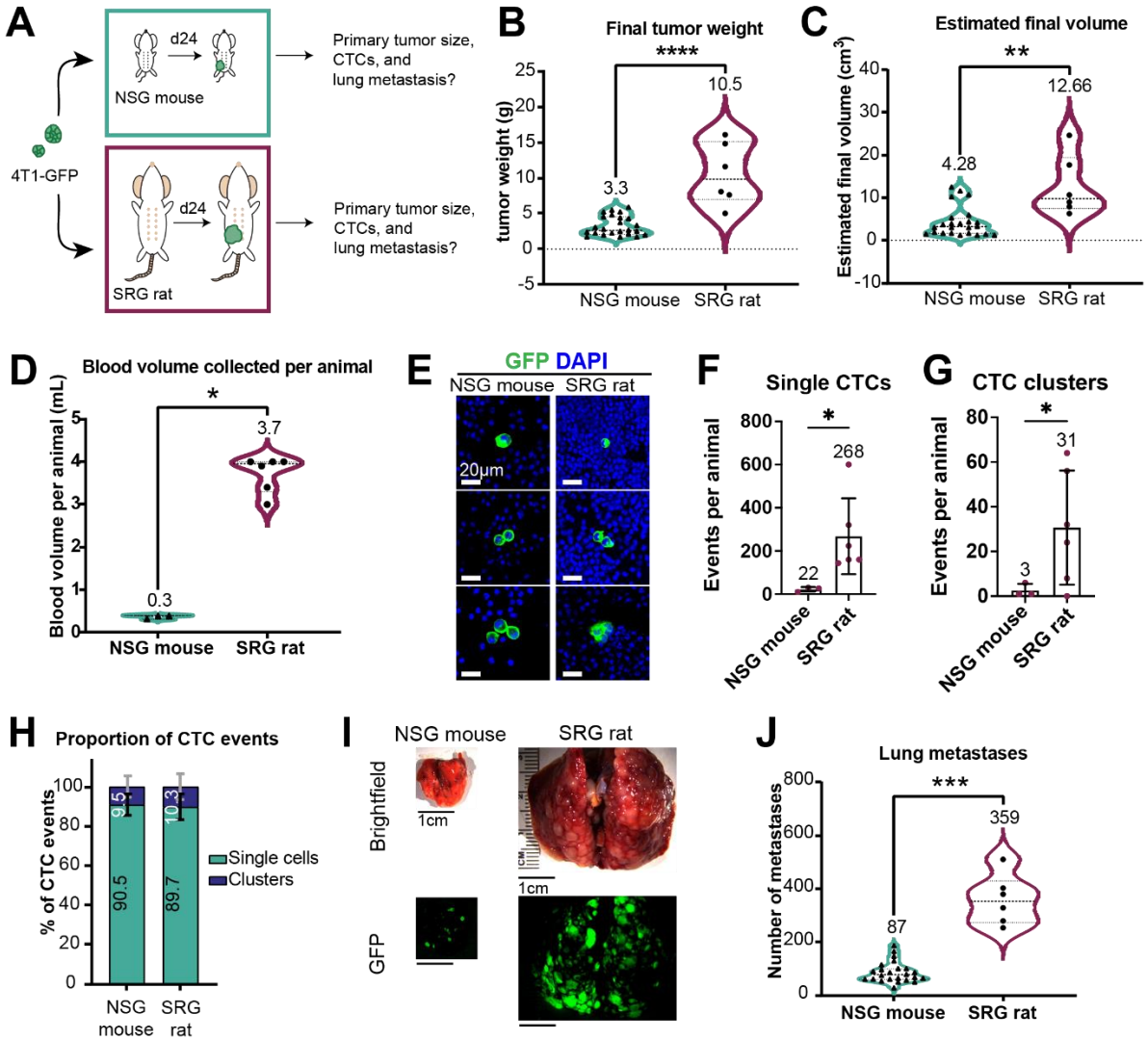

Supplemental Figure S1: Orthotopic transplantation into rats produce 3x larger tumors, 10x more CTCs, and 4x more lung metastases than into mice.

S1A) Experimental schema. 4T1 mouse mammary tumor cells labeled with membrane GFP (4T1-GFP) were orthotopically transplanted into a single #4 mammary fat pad of SRG rats (n=6) or NSG mice (n=24). Animals were sacrificed at 24 days post-transplantation.

S1B-C) Final tumor weight and estimated final tumor volume per animal.

S1D) Blood volume collected per animal.

S1E) Representative micrographs of single CTCs and CTCs clusters from 4T1-GFP transplanted SRG rats. GFP denoted in green. DAPI in blue.

S1F-G) Single CTC and CTC cluster abundance per animal. Individual blood samples from 8 mice were pooled into one tube for a total of n=3 samples. Events per individual animal are reported.

S1H) Percentage of CTC events that were single CTCs or CTC clusters. Mean ± SD.

S1I) Representative stereomicroscope images of lung metastases from NSG mice and SRG rats.

S1J) The number of lung metastases determined by stereomicroscopy in transplanted SRG rats and NSG mice.

Mean values shown on graphs. All P-values determined by Welch’s t-test.

Supplementary Figure 2

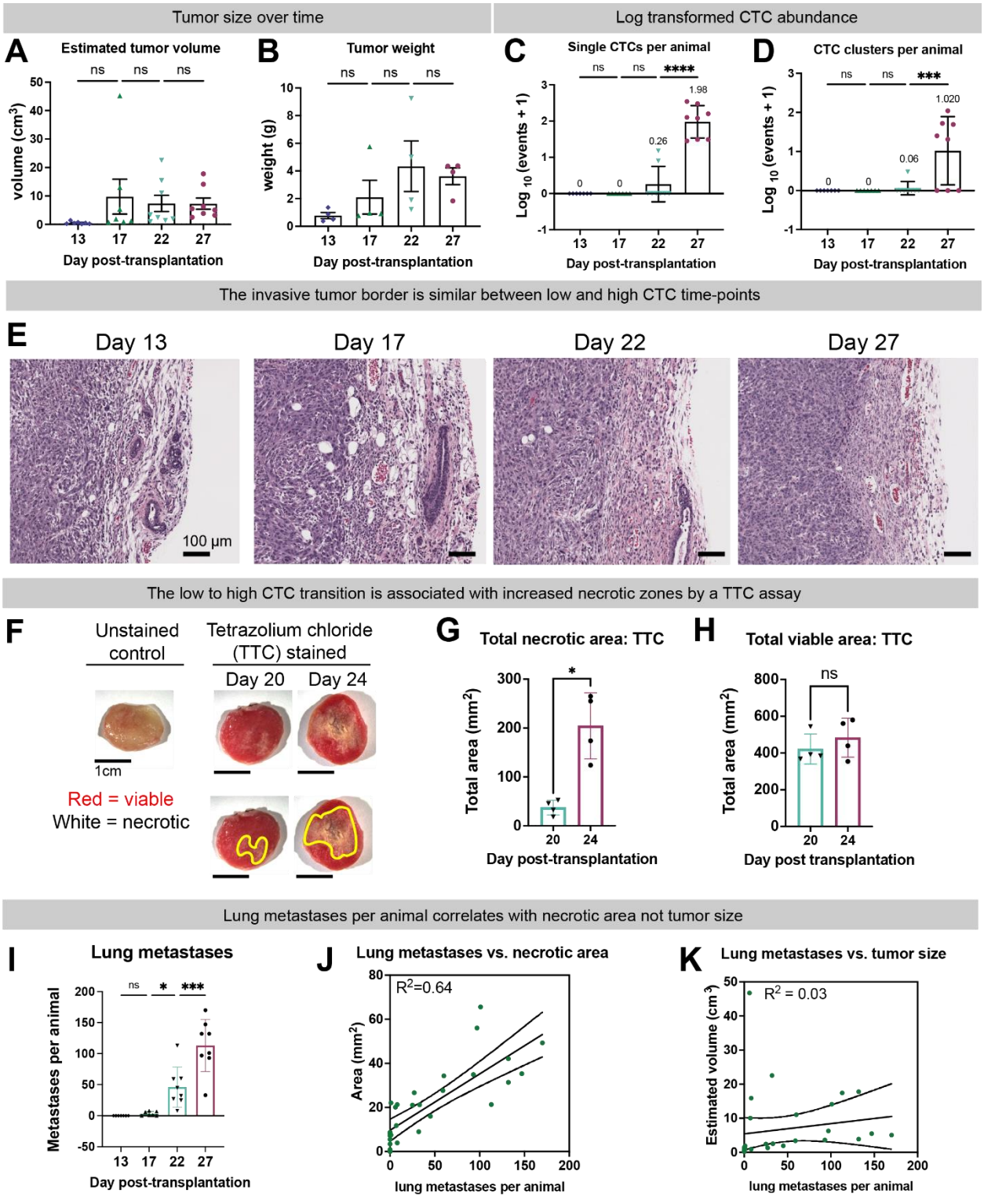

Supplemental Figure S2: Additional morphometric parameters and their correlation with low to high CTC transition

S2A-B) Estimated tumor volume and final tumor weight determined from animals collected as in Fig. 1A. Mean ± SD.

S2C-D) Single CTC and CTC clusters per animal plotted on log scale. Mean ± SD.

S2E) Representative H&E images of the invasive tumor border.

S2F) Representative images of TTC stained tumors. Red areas are viable tissue while white areas are necrotic tissue. Unstained control is provided. Yellow borders indicate necrotic region.

S2G-H) Total area of necrosis and viable area determined from the TTC assay. n=4 animals per time point; 2 to 3 slices per tumor. Mean ± SD.

S2I) Lung metastases per animal. Mean ± SD.

S2J-K) Correlation between lung metastases and necrotic area (J) and lung metastases and tumor size (K). Pearson R. Linear trend lines shown with 95% confidence intervals.

P-values for A-D and I determined by one-way ANOVA. P-Values for G-H determined by Welch’s t-test.

Supplementary Figure 3

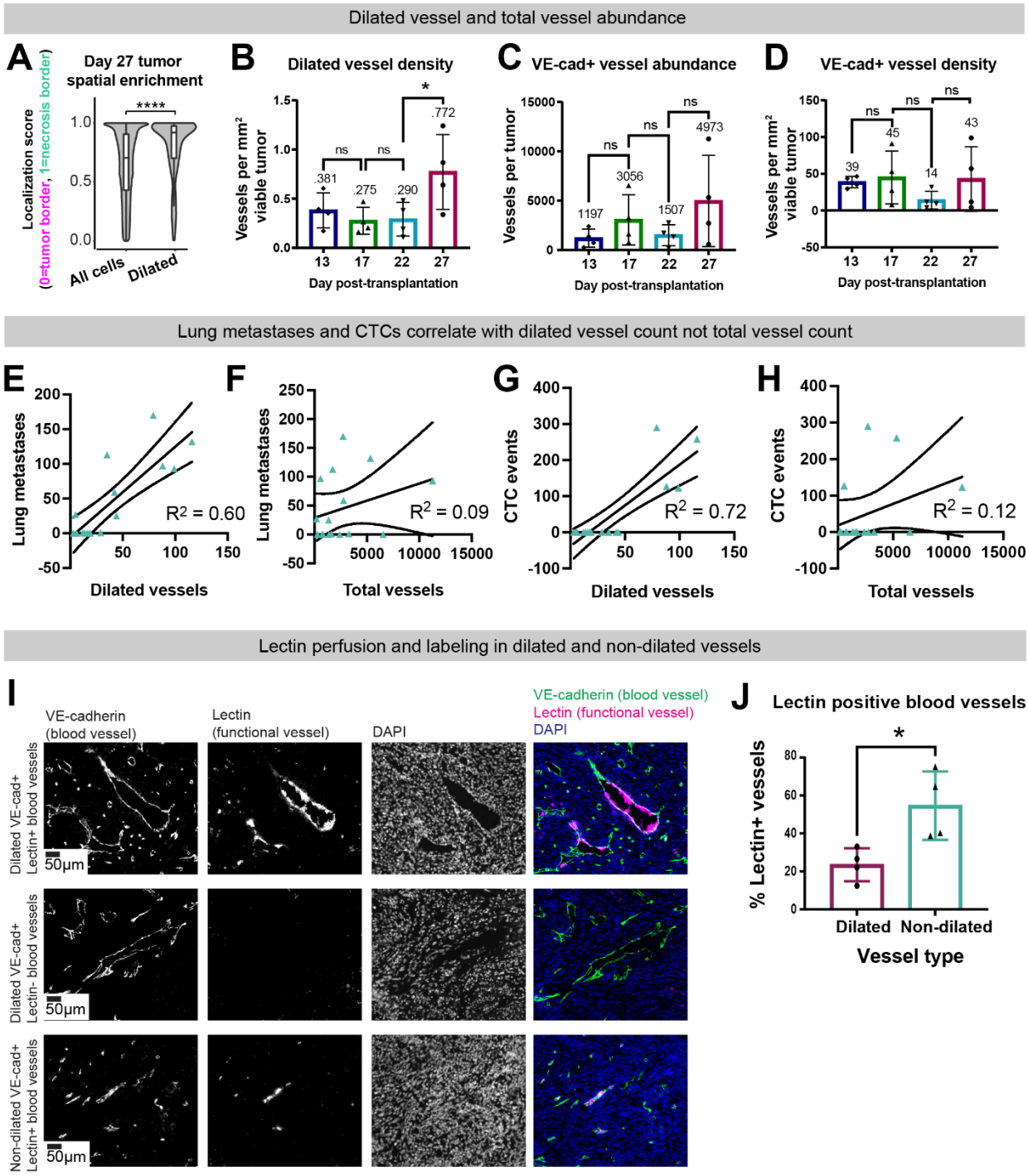

Supplemental Figure S3: Additional information on characteristics of blood vessels.

S3A) Dilated blood vessel spatial localization. Distance of VE-cadherin-positive dilated vessels to necrosis or tumor border was measured then normalized to a spatial proximity score of 0 to 1, where 0 means a spot is on the tumor border, and 1 means a spot is in a necrotic region. Spatial localization of all cells were plotted as a control. P-value determined by Kruskal-wallis test.

S3B) Dilated VE-cadherin vessel density per mm^2 viable tumor area determined per animal. Mean ± SD.

S3C) Total VE-cadherin abundance determined per animal. Mean ± SD.

S3D) Total VE-cadherin vessel density per mm^2 viable tumor area determined per animal. Mean ± SD.

S3E-H) Correlation between lung metastasis or CTC events with dilated vessels (E) and total vessels (F). Correlation between CTC events and dilated vessels (G) and total vessels (H). Pearson R. Linear trend lines shown with 95% confidence intervals.

S3I) Representative immunofluorescence images of dilated and non-dilated blood vessels in 4T1 tumors perfused with lectin-594 and stained for VE-cadherin.

S3J) Percent lectin-positive VE-cadherin-positive blood vessels in 4T1 transplant tumors. Mean ± SD.

P-values for B-D determined by one-way ANOVA; J by paired t-test.

Supplementary Figure 4

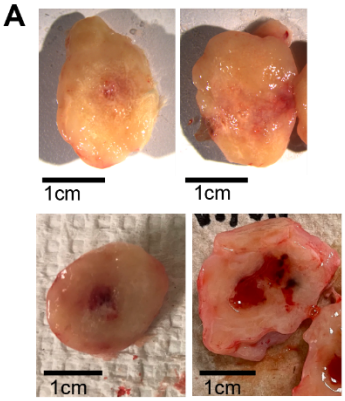

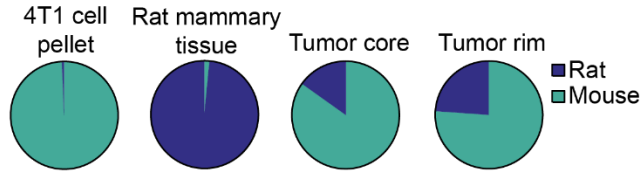

Sample Type	% mapped to mouse genome	% mapped to rat genome
4T1 cell pellet (n=1)	99.41%	0.59%
Rat mammary tissue (n=2)	1.53% ± 0.0002%	98.47% ± 0.0002%
Tumor core (n=5)	84.84% ± 1.35%	15.16% ± 1.35%
Tumor rim (n=5)	76.12% ± 5.96%	23.88% ± 5.96%

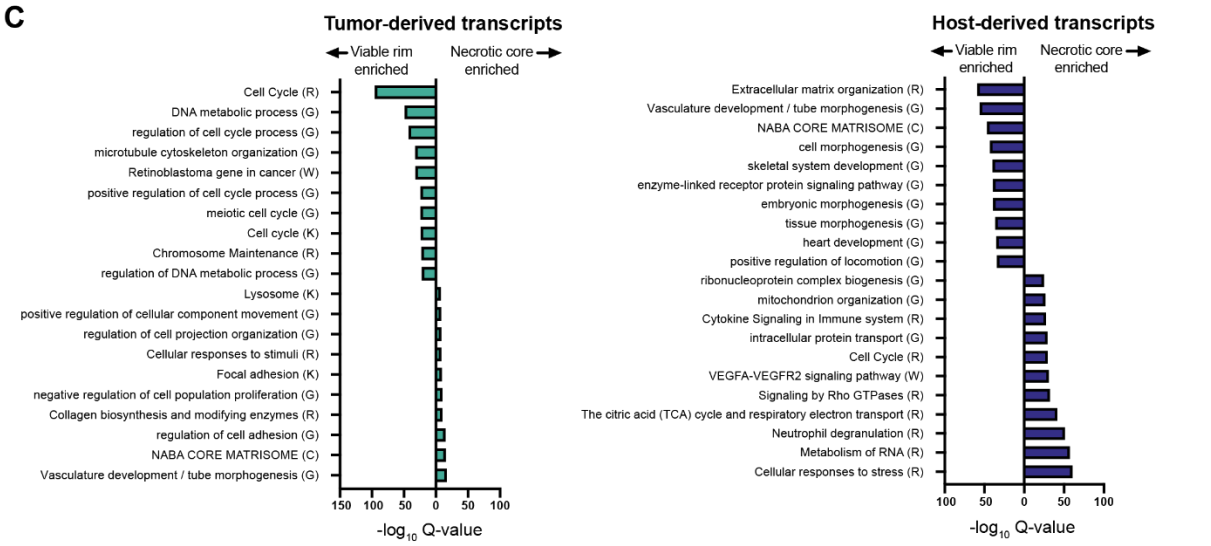

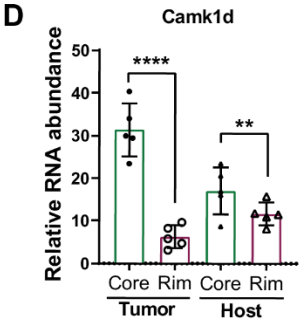

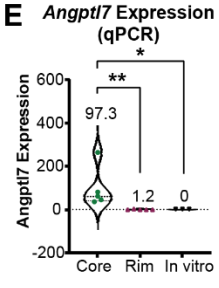

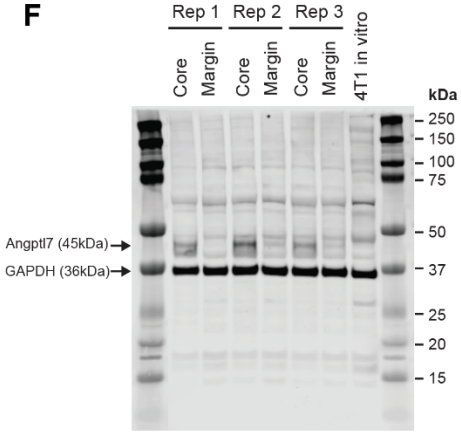

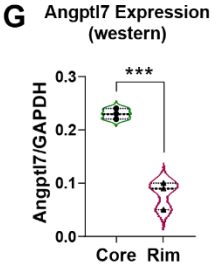

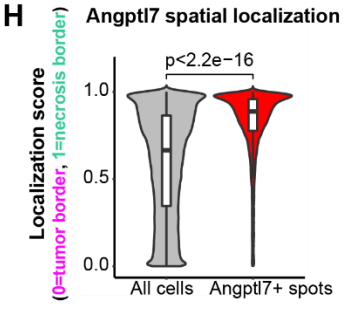

Supplemental Figure S4: Additional information on tumor core transcriptional profiling.

S4A) Representative images of necrotic cores of primary tumors used for bulk RNA-seq.

S4B) Percent of transcripts which mapped to the mouse or rat genome. 4T1 cell pellets served as control for mouse-only samples, and rat mammary tissue was used as rat-only samples. Average percentage and standard deviations are shown in the table.

S4C) Top tumor or host-derived gene sets enriched in the tumor core and rim, based on Metascape analysis. Q-value (FDR- False discovery rate) ≤ 0.01 was used as the cut-off for the gene list. R= reactome, W= WikiPathways, G= GO ontology, K= KEGG C= Canonical Pathways.

S4D) Relative RNA abundance of tumor or host-derived Camk1d expression in the tumor core or rim. Camk1d is the #1 most enriched tumor-derived gene in the tumor core. Camk1d is also expressed by the host and is not tumor specific. Average expression and q-value (FDR) from multiple comparisons indicated on the graph.

S4E) Angptl7 expression in 4T1 tumor core, 4T1 tumor rim, and 2D culture 4T1 cells based on qPCR. Mann-Whitney. Average values shown.

S4F) Western blot of necrotic core and non-necrotic rim regions of 4T1 tumors to assess protein-level differential expression of Angptl7. Angptl7 is highly expressed in necrotic region of the tumor but not the non-necrotic region. GAPDH was used as loading control. 4T1 cells in vitro do not express Angptl7 and was used as the negative control. N=3 rat tumors.

S4G) Quantification of protein-level expression of Angptl7 from S3F. P-value determined by paired t-test.

S4H) Angptl7 spatial localization. Distance of Angptl7+ spots to either necrosis or tumor border was measured then normalized to a spatial proximity score of 0 to 1, where 0 means a spot is on the tumor border, and 1 means a spot is in a necrotic region. Spatial localization of all cells are plotted as a control. P-value determined by Kruskal-wallis test.

Supplementary Figure 5

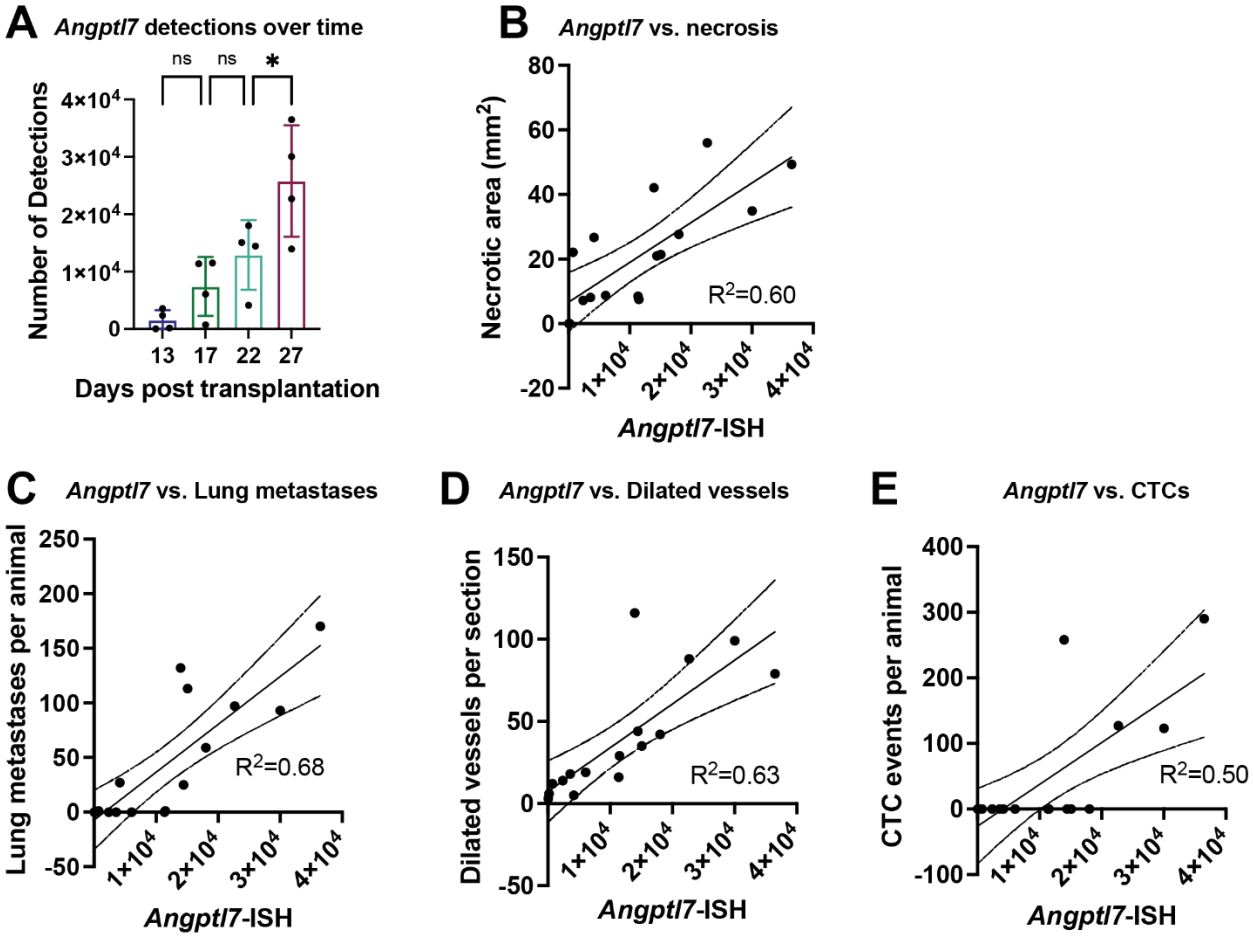

Supplemental Figure S5: *Angptl7* expression increase with day post-transplantation, correlates with necrotic area, lung metastases, and dilated vessels.

S5A) *Angptl7* detections from day 13 to day 27 post-transplantation based on RNA ISH. P-values determined by one-way ANOVA.

S5B-E) Correlation between Angptl7 detections per tumor and necrotic area, lung metastases, dilated blood vessels, or CTC events. Pearson R. Linear trend lines shown with 95% confidence intervals.

Supplementary Figure 6

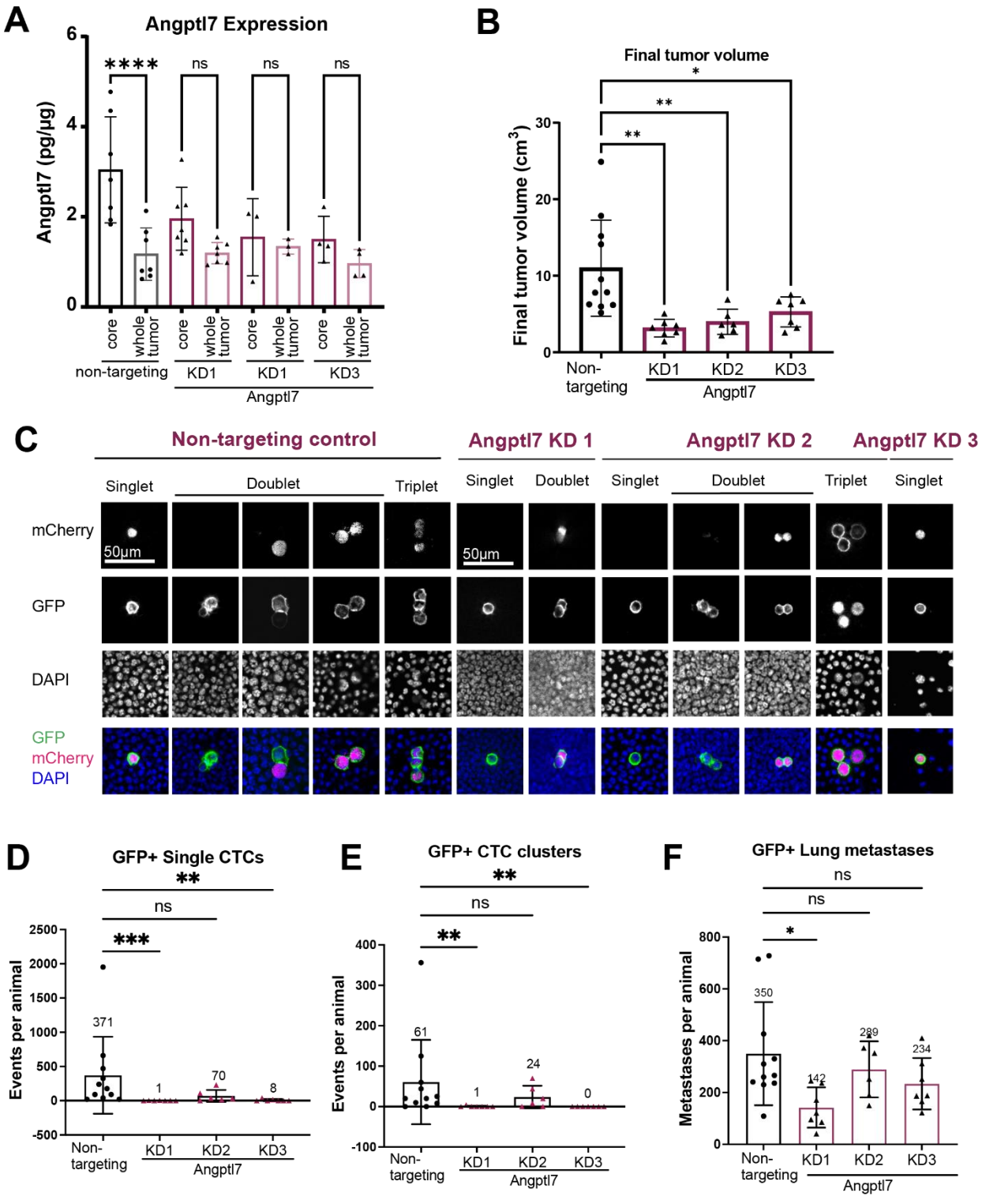

Supplemental Figure S6: Additional information on in vivo effects of Angptl7 suppression.

S6A) Quantification of ELISA of necrotic core and whole 4T1 tumors for Angptl7. Angptl7 is highly expressed in necrotic region of the tumor. Non-targeting control (n=7), KD1 (n=7), KD2 (n=3), and KD3 (n=4). Paired t-test.

S6B) Estimated final tumor volume of non-targeting and Angptl7 KD tumors.

S6C) Representative images of single CTCs and CTC clusters from Angptl7 knockdown or non-targeting control transplantation into SRG rats. Cells are mCherry-positive if they express shRNAs. 4T1 cells are labeled by membrane GFP. DAPI marks nuclei.

S6D-E) GFP-positive single CTC and CTC cluster abundance in Angptl7 knockdown and non-targeting control

S6F) GFP+ lung metastases.

All graphs reported as mean ± SD and p-values determined by one-way ANOVA.

Supplementary Figure 7

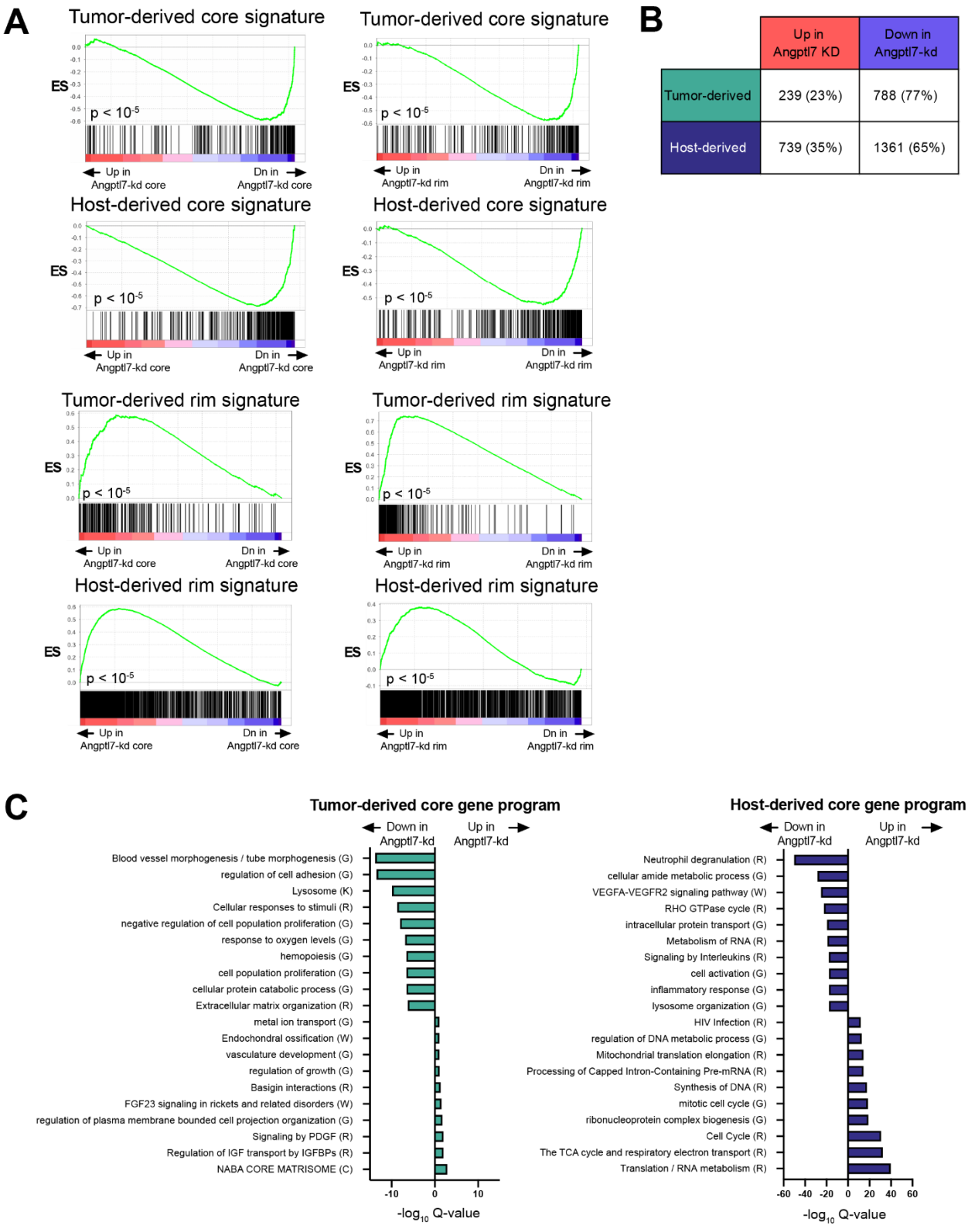

Supplemental Figure S7: Additional information on in vivo effect of Angptl7 suppression on gene expression.

S7A) Gene sets were generated composed of tumor-derived and host-derived core and rim genes with fold change ≥ 2 and FDR ≤ 0.001. The relative enrichment of these 4 gene sets was determined for tumor core or rim from Angptl7 knockdown and non-targeting control.

S7B) Genes within tumor-derived and host-derived necrotic core gene sets with FDR ≤ 0.01 were stratified by t-statistic and divided into genes up or down in Angptl7-kd conditions.

S7C) Metascape analysis of tumor and host-derived tumor core gene program stratified by their change in expression with Angptl7 suppression. Gene set enrichment reported as log Q-value.

Supplementary Figure 8

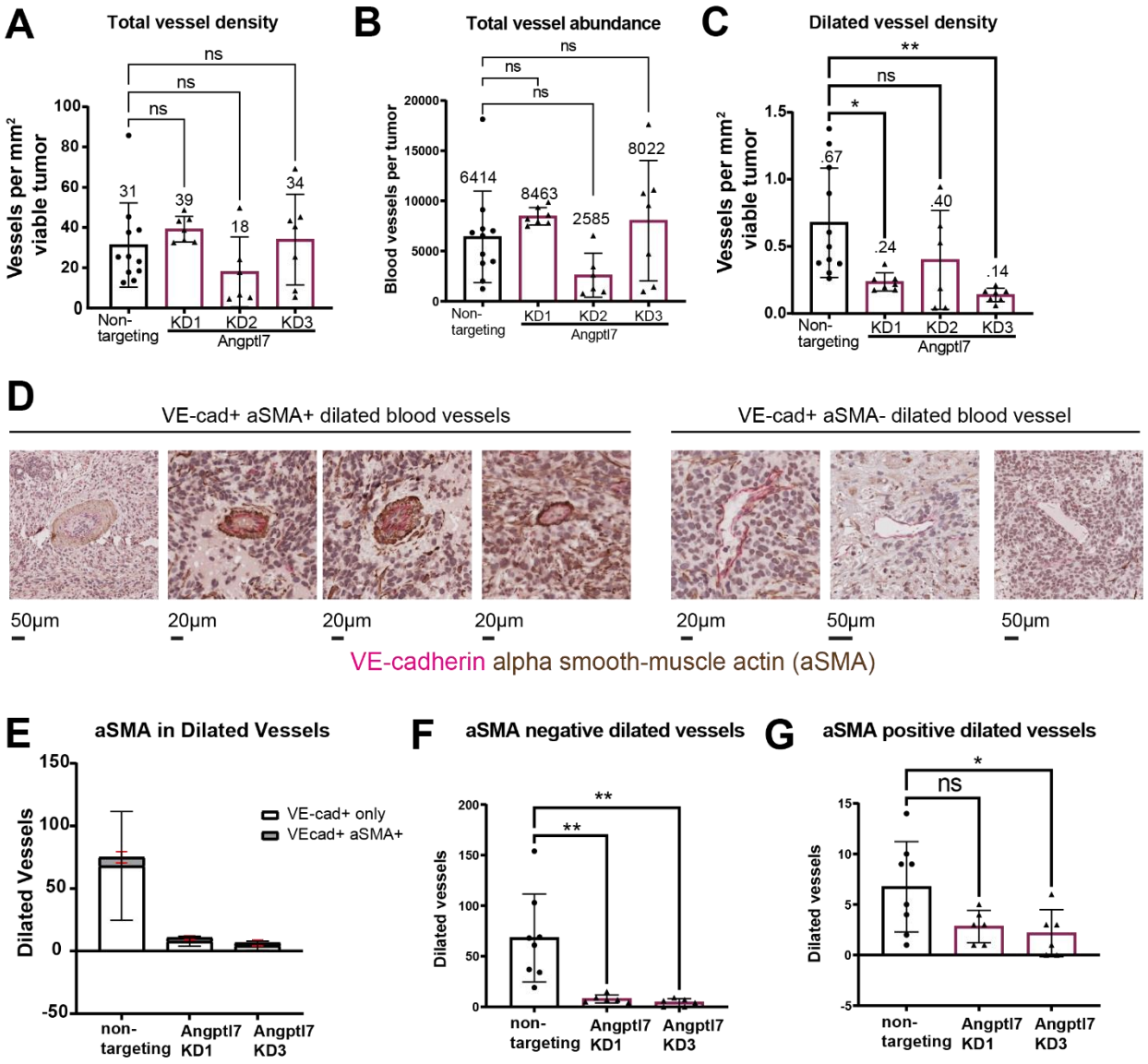

Supplemental Figure S8: Additional information on in vivo effect of Angptl7 suppression on blood vessels.

S8A) Total VE-cad+ blood vessel density per mm^2 viable tumor area per animal for Angptl7 KD and non-targeting control tumors.

S8B) Total VE-cad+ blood vessel count per tumor for Angptl7 KD and non-targeting control tumors.

S8C) Dilated VE-cad+ blood vessel density per mm^2 viable tumor area per animal for Angptl7 KD and non-targeting control tumors.

S8D) Representative imaged of alpha smooth actin immunohistochemistry. VE-cadherin in vector red (pink), alpha smooth actin in NOVA Red (brown), counterstained with hematoxylin (purple).

S8E) Alpha smooth actin-positive (aSMA) coverage on VE-cadherin positive dilated vessels in non-targeting control and Angptl7 KD tumors.

S8F) Number of VE-cadherin positive blood vessels with no aSMA coverage in non-targeting control and Angptl7 KD tumors.

S8G) Number of VE-cadherin positive blood vessels with aSMA coverage in non-targeting control and Angptl7 KD tumors.

All graphs shown as mean ± SD. P-values determined by one-way ANOVA.

Supplementary Figure 9

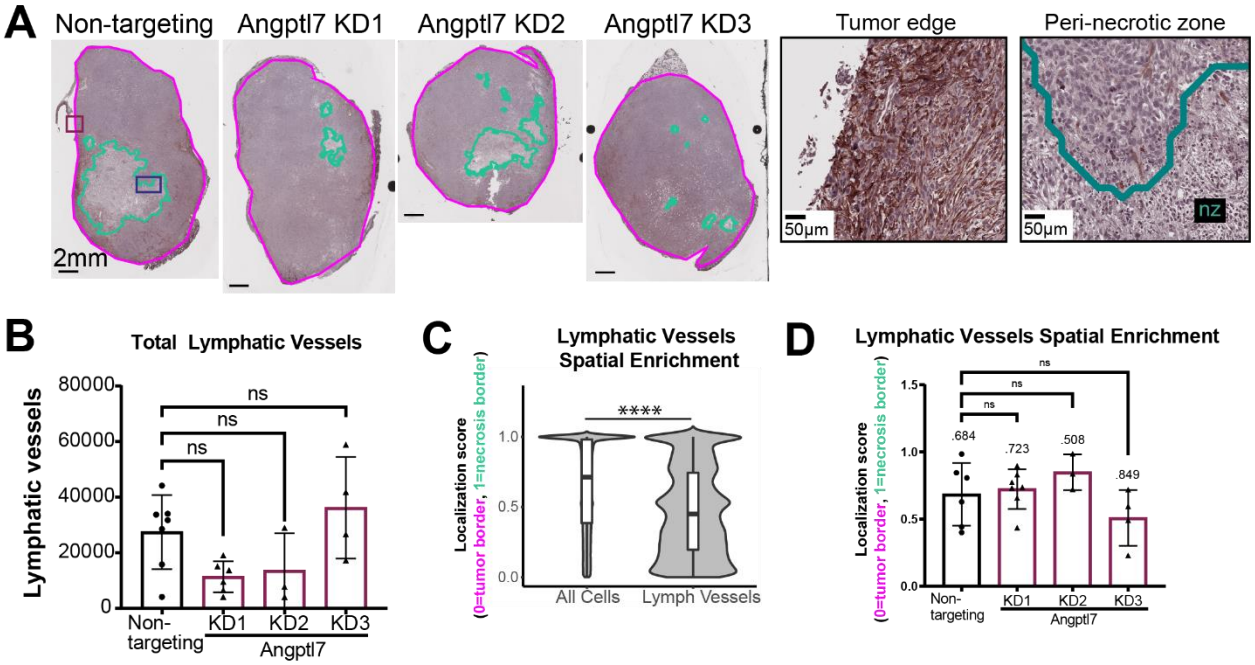

Supplemental Figure S9: In vivo effect of Angptl7 suppression on lymphatic vessels.

S9A) Representative images podoplanin+ lymphatic vessels in Angptl7 knockdown and non-targeting control tumors. Immunohistochemistry for podoplanin (DAB) (brown) counterstained with hematoxylin. Turquoise: necrotic region, pink: tumor border. Navy border inset is an example of the tumor edge. Magenta border inset is an example of a peri-necrotic region.

S9B) Number of podoplanin+ lymphatic vessels in the Angptl7 knockdown and non-targeting control tumors. Mean ±SD. One-way ANOVA.

S9C) Spatial enrichment of non-targeting control tumors comparing all cells (control distribution) with all podoplanin+ lymphatic vessels. P-value determined by Kruskal-wallis test.

S9D) Spatial enrichment of podoplanin+ lymphatic vessels in Angptl7 KD and non-targeting control tumors. Mean ±SD. One-way ANOVA.

Supplementary Figure 10

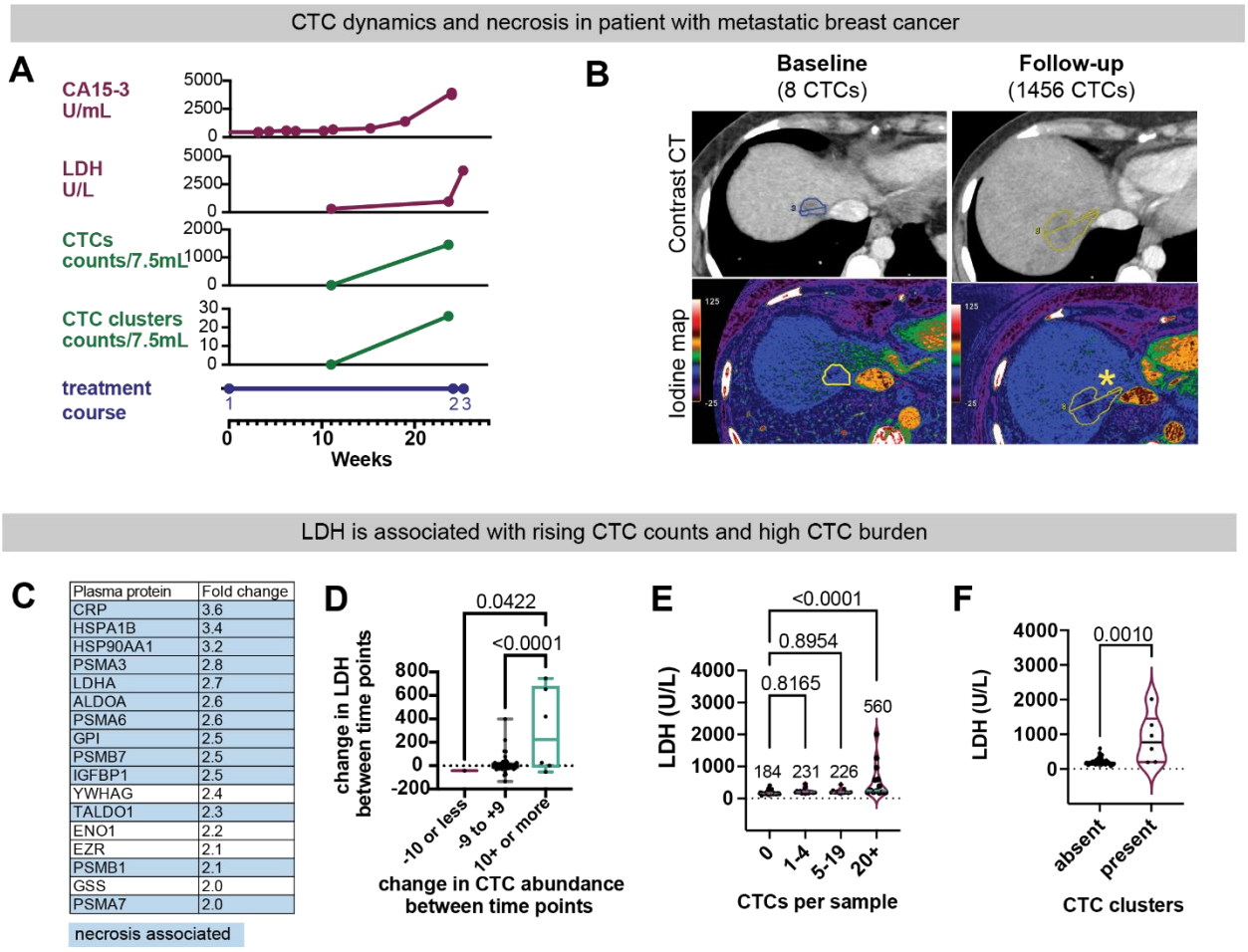

Plasma protein	Fold change
CRP	3.6
HSPA1B	3.4
HSP90AA1	3.2
PSMA3	2.8
LDHA	2.7
ALDOA	2.6
PSMA6	2.6
GPI	2.5
PSMB7	2.5
IGFBP1	2.5
YWHAG	2.4
TALDO1	2.3
ENO1	2.2
EZR	2.1
PSMB1	2.1
GSS	2.0
PSMA7	2.0

necrosis associated

Supplemental Figure S10: Supplementary information on correlation of CTC and necrosis in breast cancer patients with metastatic disease.

S10A) Clinical vignette of patient with metastatic breast cancer and acute CTC elevation.This was a patient with **d**e novo stage IV ER+PR+HER2- metastatic breast cancer involving the right breast, lymph node, bones, liver and lung. Despite initial response to endocrine therapy in combination with the CDK4/6 inhibitor palbociclib, the patient progressed and was switched to capecitabine monotherapy. Over a 30-week period, the patient demonstrated increasing blood levels of tumor marker CA15-3, indicating progressive resistance to therapy. At week 4, an initial CTC determination yielded a CTC count of 8 per 7.5 mL and no CTC clusters. At week 24, a repeat CTC determination showed a CTC count of 1456 per 7.5 mL and 26 CTC clusters per 7.5 mL. Strikingly, lactate dehydrogenase (LDH), a marker of tissue necrosis, also increased over the same period: 309 at week 4 to 963 at week 24 and 3727 U/L at week 26, during inpatient admission for workup of abdominal pain, liver injury, and tumor lysis. Treatment course: (1) capecitabine, (2) in patient admission for liver injury and tumor lysis, (3) death. CA15.3, cancer antigen 15-3; LDH, serum lactate dehydrogenase.

S10B) Dual energy scanning contrast tomography. Baseline scan obtained 1 month prior to first draw (CTC=8 per 7.5 mL). Follow-up scan obtained 1 week after second draw (CTC=1456 per 7.5 mL) during in hospital admission. Upper panels: contrast enhanced CT. Lower panels: iodine distribution. The right lobe liver metastasis (yellow outline) measured 3.1 cm at baseline with a maximum iodine concentration of 38 µg/cm3 and an average of 19.2 µg/cm3 which grew to 4.7 cm on follow up 3 months

later and the maximum iodine concentration decreased to 32 µg/cm3 and the average to 14.2 µg/cm3. Lower iodine concentration is indicative of decreased perfusion and increased necrosis.

S10C) Tandem-mass tag mass spectrometry of late versus early time points for low-to-high CTC transitions (n=3 patient sample pairs). Volcano plot shows the plasma proteins enriched in high CTC samples with P-values less than 0.1. Metascape analysis of proteins reported by -log Q-value. Listed are proteins with 2-or-more fold-enrichment in high CTC samples. Necrosis-associated proteins highlighted in blue.

S10D) Change in LDH between time points according to change in CTC abundance between time points. P-values determined by one-way ANOVA comparing against 10+ or more CTCs.

S10E) Serum LDH in relation to CTCs per sample. N=39 patients, 93 blood samples. P-values determined by one-way ANOVA comparing against 20+ CTCs.

S10F) Serum LDH in relation to presence or absence of CTC clusters. N=39 patients, 93 blood samples. P-values determined by Mann-Whitney test.

Chapter 3. RAT MODEL PROTOCOLS FOR BREAST CANCER METASTASIS RESEARCH

3.1 ABSTRACT

In vivo modeling using rodents is critical to study cancer metastasis. Although mice are a common tool to use to this end, when there is a need for large amount of blood or tissue, a larger rodent such as rats may be better suited. Rats can generate ten times more blood and three times more tumor tissue than mice. In addition, transplanting mouse tumor cells into rat host enables RNA-seq deconvolution to identify which transcripts were derived by tumor and which were derived by host. However, due to the large size of rats and the tumors they generate, there are considerations that need to be made when working with rats as model organisms. Here, we detail the orthotopic mammary fat pad transplantation method in rats as well as well as downstream tissue processing for RNA, DNA, and protein level analysis of these tissues. The orthotopic transplantation protocol in rats is adapted from the protocol for mice. Modifications include need of larger anesthesia chamber and nose cone, longer anesthesia time and isoflurane flow rate, larger incision, larger surgical site closer with a combination of staples and skin glue. In addition, handling of rats for tumor measurements and other post-surgery procedures may require two handlers. We also detail how to fix or snap freeze tissues for downstream applications such as immunohistochemistry, immunofluorescence, protein lysate (for western blots, ELISAs, or proteomics), and RNA extraction (for RT-qPCR or RNA-seq). Rat husbandry and care is a requirement to use this protocol.

3.2 INTRODUCTION

Rodent models are a key tool to study breast cancer metastasis and identify potential therapeutics. Mouse models including genetically engineered mouse models (GEMMs) and transplantation models are common and essential tools to understand how breast tumors metastasize in live animals[202–205]. There are many advantages to using mouse models such as ease of handling, abundant resources, well-characterized GEMMs and breast tumor cell lines, and many research institutions having facilities and equipment for mouse care and procedures. However, there are certain disadvantages to mice as models for cancer metastasis including their small size. Some steps in the metastatic process such as intravasation and dissemination are rare, dynamic events which are difficult to capture[206–211]. One barrier to study circulating tumor cell (CTC) dissemination is the rarity of CTCs in model organisms which can be experimentally perturbed. For this reason, in Yamamoto et al. 2023, we used rats as a model system to study CTCs and cancer metastasis[212]. We found that about ten times more blood and over three times more tissue can be collected terminally from rats compared to mice[212]. In addition, transplanting mouse tumor cells into rats allows for xenograft deconvolution in which tumor derived transcripts can be differentiated from host derived transcripts, making it possible to understand which genes and being transcribed in the tumor or host stroma. For our purposes, these were major advantages to using rats to study breast cancer metastasis.

However, mice and rats have key differences which are important for the context of studying breast cancer and mammary gland biology. For example, mice have mammary chains with five pairs of glands (three pairs in the cervicothoracic region and

two pairs in the inguinoabdominal regions) whereas rats have six (three in each region)[213]. In addition, the mammary ductal tree in adult non-lactating mice ends in blunt ductules and develops into terminal ductal lobular units (TDLUs) only during pregnancy. In rats, the ductal tree ends in TLDUs with alveolar development without pregnancy[213,214]. Further, the mammary stroma is mostly made up of adipose tissue with very little connective tissue in mice. In rats, there is an abundance of connective tissue along with adipose tissue around the TDLUs[214]. It is also worth mentioning that in these ways, rat mammary glands are more similar to human mammary glands. In humans, female ductal trees terminate in TLDUs with alveolar development at sexual maturity, not only during pregnancy and lactation. Humans also have mammary stroma containing both collagenous connective tissue and adipose tissue, similar to rats.

Therefore, rats should not be thought of simply as larger mice; they are, after all, completely different species. However, this is not to say that the larger size of rats compared to mice does not play a significant role in experimental methods. Because of the larger size of the rat and the tissues generated in rat models, there are some alterations that should be made to mammary fat pad transplantations into rats as well as downstream blood and tissue processing. These differences should be carefully considered when adapting protocols to use rat models. Here, we detail important considerations and tips for using rats as transplantation models for breast cancer metastasis.

3.3 MAMMARY FAT PAD TRANSPLANTATION OF CELLS INTO RATS

All rodent procedures and experiments must be approved by and performed in accordance to the institution-approved IACUC protocols and AAALAC guidelines and ethical regulations.

Animals:

For transplantation of mouse breast tumor cells into rats, we used the Sprague–Dawley Rag2/Il2rg double knockout (SRG) immunodeficient rat model developed by Hera Biolabs and available from Charles River (Strain #707). Like NSG mice, these rats lack T-cells, B-cells, and functional NK-cells. SRG rats have been demonstrated to have good take rates for patient derived xenograft (PDX) models as well as cancer cell lines including Vcap prostate cancer cell line[215,216]. In Yamamoto et al. 2023, we used the SRG rat model to transplant fluorescently labeled 4T1 mouse triple negative breast caner cell line with shRNA knockdowns[212].

Materials:

Equipment:

- Isoflurane chamber (larger size for rats)
- Nose cone for rats
- Bead sterilizer to sterilize surgical tools between animals
- Heating pad for animal recovery

Supplies & Reagents:

- Surgical tools: both small and larger tweezers + surgical scissors (small for mice, larger for rats)
- PBS (-Ca^{2+}, -Mg^{2+}) in 50 mL conical
- 70% Ethanol in 50 mL conical
- Empty 50 mL conical for waste
- Rack for holding 50 ml size tubes
- Bupivicaine (or other analgesic on protocol)
- 1mL syringes and needles (to withdraw bupivicaine)
- Isoflurane
- Surgical anesthesia forms (one per animal)
- Ear tagger and tags
- P200 Pipet to mix sample periodically
- P200 pipet tips
- 2.5% BSA to coat pipet before pipetting up and down
- Lots of sterile cotton swabs
- Hamilton syringe 702RN (7636-01), with custom needles 1” long and 26 gauge
- Electric shaver and/or Nair (hair removal cream)
- 3M wound tape
- Wax surgery pads + pins
- Sterile disposable surgery pads (1 per animal)
- Triple antibiotic cream
- Surgical stapler and surgical staples
- 3M Vetbond skin glue (3M 1469c)

Procedure:

*Reference **Figure 1** for this protocol.*

Adapted from Cheung et al. Cell 2013; Cheung et al. PNAS 2016[44,217]

1. Animal should be anesthetized by isoflurane inhalation (2.5% for mice) (up to 3.5% for rats)
2. Place the mouse in the induction chamber for several minutes until it stops moving. To check for responsiveness, shake the chamber slightly. If the mouse moves, then wait longer.
3. Transfer the animal to a surgical board with the snout in a nose cone connected to the isoflurane. Pinch the animal's foot; if it doesn't flinch, proceed.
4. First tape (use 3M wound tape) the animal's arms vertically upward rather than out to the side in order to maximize airflow. Tape the legs down. Be careful not to overextend limbs. Continue to monitor breathing to ensure it is steady but not forced.
5. Shave the fur on the abdomen to remove excess fur.
6. Clean surgical field

   2a. Clean surgical area with 70% ethanol using a sterile swab in a circular motion, starting in the center. Do not go over the same area twice with the same swab.

   2b. Repeat 2a but with 2% chlorhexidine.

   2c. Repeat 2a-b twice more for a total of three times.
7. Make 5-10mm vertical incision with sterile surgical scissors (blunt side down) at the midline between T4 and T5 nipple. Do NOT penetrate into the abdominal cavity. You should be in the subcutaneous space.

8. Insert sterile cotton swab into incision to separate skin from the peritoneum. Do this only on the side if you are transplanting on one side. Repeat on the other side if transplanting both sides.
9. Extend incision upward along the midline 2cm and at a 120-degree angle from the midline, between the T4 and T5 nipple (1cm).
10. Pull skin back to expose T4 mammary gland and use a curved pin to pin skin back. Take care to pin away from the gland and to not puncture the peritoneum. Use sterile cotton swab to further separate skin from peritoneum if necessary.
11. Use sterile tweezers to pull up on mammary fat pad and use a 20ul Hamilton Syringe (702RN) with 3 inch 26 gauge needle to inject 20ul cell suspension (in 1:1 matrigel : DMEM/F12) into T4 mammary fat pad, bevel side up. Do not puncture through the mammary fat pad (tip of syringe should be inside fat pad during injection), and you should see a small dome of fluid you injected in the fat pad.
12. Drop 2-3 drops (50-100µl) of 0.25% bupivacaine at injection site before closing.
13. Close incision

    9a. Use surgical staples to close incision.

    9b. Use skin glue in areas that are difficult to staple. Take care not to glue the staples, as this will make it difficult to remove later. Wait at least 30 seconds for skin glue to dry.

    9c. Apply triple antibiotic ointment at incision using sterile cotton swab.
14. Allow animals to recover in recovery cage on heating pad.
15. Monitor animals according to your IACUC protocol.

Timing:

This protocol will take about 20-30 minutes to set up, 10-20 minutes per rat for surgical procedure, and 20-30 mins for animal monitoring and cleanup.

3.4 HARVEST INCLUDING TERMINAL CARDIAC BLOOD DRAW:

As with cardiac blood draws in mice, terminal cardiac blood draws can be performed immediately after the animal has been euthanized or while the animal is under terminal, deep anesthesia, depending on your IACUC protocol and institution policies. We will note though that it is much easier and consistent to draw blood using deep anesthesia.

The only big differences between cardiac blood draws in rats compared to mice are 1) the volume of blood that can be collected and 2) the needle and syringe to use.

1. Whereas only 200 to 500µl of blood can be collected on a typical terminal cardiac puncture blood draw in mice, 3 to 10ml of blood can be collected from rats.
2. Because of the larger blood volume, we recommend using a 10ml syringe to collect blood. We typically use a 20G needle on the 10ml syringe. Then, we transfer the blood to an appropriate blood collection tube (eg: EDTA tube, CellSave tubes, etc).

Also note that although this harvest can be performed with one handler, it is much easier and efficient with an assistant.

Timing:

End point of the transplantation experiment varies depending on cells transplanted, host rat strain, and the experiment. For transplanting 4T1 cells as small clusters of cells into immunocompromised SRG rats, the end point is around 24-27 days post-transplantation. For slower growing cell lines, it may take longer for tumors to grow and for metastases to seed and grow out.

Procedure:

All rodent procedures and experiments must be approved by and performed in accordance to the institution-approved IACUC protocols and AAALAS guidelines and ethical regulations.

Equipment:

- Isoflurane chamber (larger size for rats)
- Nose cone for rats

Supplies & Reagents:

- 1000 U/mL Heparin
- 10mL syringe with removable 20G 1in needle (BD 309644)
- Surgical tools (scissors and two forceps) (bring extra forceps for assistant)
- Blood collection tubes (Cellsave tubes for CTC collection (Menarini Silicon Biosystems 84000016)) or EDTA tubes for ctDNA
- Wax dissection tray and pins
- Disposable surgical pads
- 3M wound tape

- Container with 10% NBF (neutralized formalin buffer) (Must fix in 10-20x tissue volume)
- Container with 4% PFA (paraformaldehyde) (made fresh)
- Cassettes (you need 1-5 per half tumor) for NBF fixation
- Pencil to label cassettes
- 1.5 ml tubes if snap freezing samples
- Liquid nitrogen if snap freezing samples
- Calipers
- Scalpels
- Isoflurane
- Conical tubes for lungs
- PBS for lungs
- Sharpie
- Stands for blood tubes, conical tubes, etc.
- Paper and pen

Protocol:

1. Set up:
    a. Blue absorbent pad, wax dissection tray, and disposable surgical pad/sheet per animal.
    b. Surgical tools (does not need to be sterile) but cleaned with 70% ethanol then dried.

   c. Heparin coated 10ml syringes. To coat, draw up 10ml of heparin from glass vial, allow heparin to coat syringe, and eject heparin back into vial. When you do this, if there is no pressure and the syringe is not drawing liquid up even though needle is firmly attached to the syringe, dispose of the syringe. It is rare, but about 1 in 50 or 1 in 100 syringes is bad and does not draw up fluid well. This means the syringe will not be good for blood draw either.
   d. Blood collection tubes with caps opened once and lid ajar (to make it easier to remove cap one-handed). Label blood tubes with rat IDs.

2. Set up isoflurane chamber the same way from transplantation. Isoflurane should be around 3.5% for rats. Make sure rats are under deep anesthesia and that they never wake up from the anesthesia if performing a terminal blood draw using this method.
3. Move rat to surgical board. Pinch toes to make sure they are asleep. Tape limbs down with 3M wound tape. Rat's breathing should be slow, indicating rat is under deep anesthesia.
   a. Move precisely but quickly once rat is down so that rat is complete under deep anesthesia but is not under anesthesia for too long before blood draw as being under anesthesia for far too long may decrease yield of blood.
4. Spray 70% ethanol on rat upper abdomen and rub into fur so fur stays down.
5. Make an incision with surgical scissors right below the rib cage.
6. Cut into the abdominal cavity.

7. Extend the incision 1.5cm or so (end to end) to the left and right of the initial incision. You will either see the diaphragm or the liver at this point. If you see liver, gently move it down so you see the diaphragm.
8. Cut into the diaphragm and expose the lungs.
    a. MOVE VERY QUICKY BUT PRECISELY FROM THIS POINT ON.
9. Carefully but quickly cut out rib cage, enough to expose the lungs and heart.
10. Take a heparin coated 10ml syringe with 20G needle attached.
11. With plunger almost all the way in, insert needle into the left ventricle of the heart.
    a. Be very careful not to puncture all the way through the heart.
12. Draw up SLOWLY on the syringe to collect blood.
13. If desired, you can take the needle out and put blood into the collection tube. Invert blood tube several times immediately after capping.
    a. If desired, go back into the heart to try to draw more blood
    b. If desired, puncture the right ventricle of the heart and repeat.
    c. Act quickly. As the animal's blood pressure drops, it will be more difficult to draw blood.
    d. DO NOT puncture through the heart, and especially DO NOT allow needle to touch the lungs as the needle brushing up against metastasis can collect tumor cells into the blood (which are not circulating tumor cells).
    e. Invert blood tube several times after adding more blood to tube (have assistant invert tube)
14. While rat is still under deep anesthesia, flip rat over to have back side up.

15. Swiftly but firmly perform cervical dislocation using sturdy forceps or scissors against the neck with one hand and pulling at the base of the tail with the other hand.
16. After euthanasia by cervical dislocation is complete, you can turn the isoflurane open for the chamber and off for the nose cone.
17. If collecting lungs and tumor, follow step 17.
    a. For lung, cut out and place in conical with PBS to image with stereoscope, or collect into fixative if there is no need for imaging before fixation.
        i. Fix Lungs with 10% NBF for 5 days at room temp, changing fixative out every day (for FFPE) OR fix in 4% PFA at 4°C for 24 hours (for OCT frozen blocks).
    b. For tumor, measure tumor with caliper before cutting it out, if desired.
    c. Cut tumor out using scissors and forceps.
        i. Measure weight of tumor (assistant can do)
        ii. Slice tumor in half if using for two different applications.
        iii. For FFPE: Slide into 5mm slices with scalpel along cross section from cutting in half, place in cassettes labeled with PENCIL, close, and place into container with 10% NBF. (Assistant can do this step)
        iv. For OCT, slice tumor if desired, place in cassettes labeled with pencil, close, and place into container with 4% PFA. You can put in PBS instead if you want to image tumors with stereoscope first, but you need to be FAST. If you have a lot of samples, we don’t recommend trying to image tumors with stereoscope. If you don’t

want to slice the tumors, place tissue directly into 50ml conical tubes with 4% PFA.

v. Separating core and rim and snap freezing: scoop out inside mushy part with scissors, cut up into pieces and place into 2-3 separate 1.5ml tubes (labeled) and put in liquid nitrogen. Repeat with rim after cleaning scissors with 70% ethanol. Try to cut into as small of pieces as possible while being quick so it's easier to take out and take smaller pieces later. Place small chunks of tumor into 1.5mL tube, cap the tube, and snap freeze with liquid nitrogen.

18. Place animal carcass into carcass disposal bag.
19. Repeat with other animals if needed.
20. Clean up.

Recommendations for blood draw:

- We also highly recommend CellSave tubes for CTC visualization; however, CellSave tubes include a fixative which is not ideal for downstream RNA applications.
- If using Ficoll separation for CTC enrichment, we recommend using Ficoll-Paque PLUS (density 1.077 g/mL) (Cytiva 17144003) for rat blood.

3.5 LYSATES FOR DOWNSTREAM APPLICATION

Because of intra-tumor heterogeneity, especially in large rat tumors, taking small portions of the tumor from one area for downstream analysis (sequencing, western blotting, etc.)

could lead to vastly different result every time. Therefore, it is important to homogenize the tumor samples before extracting RNA, DNA, or protein for downstream application. For snap frozen samples, this can be achieved by pulverizing tissues while maintaining samples in contact with liquid nitrogen.

Method 1: 1.5mL tube as the mortar

We used the SP Bel-Art Scienceware® Liquid Nitrogen Cooled Mini Mortar & Pestle Set (Thomas Scientific: 1220W95). The apparatus has a groove to fit a 1.5mL tube into (containing your snap frozen tissue) and space to pour liquid nitrogen into beneath it. It also includes a stainless-steel pestle which fits into 1.5mL tubes to pulverize the tissue.

Materials:

Equipment:

- SP Bel-Art Scienceware® Liquid Nitrogen Cooled Mini Mortar & Pestle Set (Thomas Scientific: 1220W95)

Supplies & Reagents:

- Liquid nitrogen
- Standard 1.5mL tubes (NOT round bottom)
- 70% ethanol for cleaning
- Forceps for picking up tissue
- Scissors or scalpel
- Dry ice

Protocol:

1. Keep all samples on dry ice or liquid nitrogen at all times.
2. Pour liquid nitrogen into the bottom, part of the Liquid Nitrogen Cooled Mini Mortar Pestle apparatus to the fill line.
3. Place labeled 1.5mL tube into the slot for the 1.5mL tube in the center of the top part of the apparatus.
4. Allow top part of the apparatus and 1.5mL tube to cool down with liquid nitrogen
5. Take out a small piece (50-100mg) of tissue to pulverize (still frozen) and into the 1.5mL tube cooling in the apparatus.
6. Place 1.5mL tube with sample into the liquid nitrogen for at least a few seconds to cool it down as much as possible.
7. In the meantime, also dip the pestle into the liquid nitrogen for at least a few seconds to cool it down, take it out of liquid nitrogen, spray 70% ethanol, and wipe down with clean Kim wipe to clean pestle quickly (before it warms back up).
8. Fit pestle into the 1.5mL tube with sample. Push and twist the pestle to grind the sample up. The sample is small, so there may not be very much resistance. Be careful not to exert too much force, as this could result in the 1.5mL tube cracking.
    a. If sample was snap frozen in too big of pieces when initially frozen, cut the sample into smaller pieces before pulverizing. If tissue is too hard to cut, allow sample to slightly thaw on ice until soft enough to cut with scalpel or scissors.
9. Cap the 1.5mL tube and put in liquid nitrogen again.
10. Repeat if necessary.

a. If wanted, cool down in liquid nitrogen then invert one tube and tap in powdered tissue into another tube to combine tubes. Make sure pulverized tissue is very cold in liquid nitrogen (not just dry ice), as if tissue is too warm, it will not come out of the inverted tube.
b. When repeating, make sure everything is chilled in liquid nitrogen.
c. Make sure to refill the bottom of the apparatus with liquid nitrogen to maintain temperature.

11. Clean pestle with 70% ethanol before moving onto next sample.

Recommendations when using this method:

- Pulverize small amounts of tissue that only fills the tip of the 1.5mL tube (approximately 50-100mg). Over filling the tube will make it difficult to pulverize the tissue. Over exerting pressure will crack the tube, resulting in losing tissue.
- Make sure the liquid nitrogen compartment is filled to keep tissues cold at all times.
- Dip pestle into liquid nitrogen to cool it to prevent tissue from melting and sticking to the pestle.
- Keep all tissue in liquid nitrogen or dry ice while on queue.

<u>Alternative method:</u>

The advantage of using a system in which tissue can be pulverized directly inside a 1.5mL tube is that it reduced tissue loss in the grinding process. However, it is possible to use a traditional mortar and pestle by pouring a small amount of liquid nitrogen into the mortar,

adding the tissue, grinding, then pouring the ground up tissue in liquid nitrogen into a tube.

Recommendations when using this method:

- If using a traditional mortar and pestle method, be careful not to cap the tube before the liquid nitrogen evaporates.

3.6 Formalin fixation for formalin-fixed paraffin-embedded (FFPE) Blocks

Because tumors generated with a rat host can get up to 4cm in diameter, extra precautions need to be taken when fixing tissue to embed in paraffin to not under-fix the tissue. Under-fixing tissue before embedding can cause tissue to fall apart when sectioning.

Materials:

Supplies & Reagents:

- 10% Neutral Buffered Formalin (NBF)
- Embedding cassette (Fisherbrand™ Histosette™ II Tissue Processing/Embedding Cassettes with Combination Lid and Base 15-182-701A)
- Plastic or glass container

Protocol:

1. Slice tumors into 5-8mm thick sections with a scalpel before placing into an embedding cassette.
2. Place sliced tissue into embedding cassette, close cassette, and place into 10% Neutral Buffered Formalin (NBF).

   a. It is recommended that you use 10-20 times the volume of 10% NBF as the volume of tissue you are trying to fix.
   b. When fixing many samples at once, we place NBF in a large plastic or glass container and place FFPE embedding cassettes with tissue inside.
   c. Remember to label your cassettes with pencil or ethanol resistant label as you will be putting these tissues in 70% ethanol after fixation.
3. For a rat or mouse mammary tumor 2-4cm in diameter sliced to 5-8mm thick, we recommend fixing for a total of 5 days in 4°C while rocking gently.
4. We highly recommend changing out the NBF to fresh 10% NBF after 6 hours after start of fixation, again in ~18 hours, then every 24 hours after that.
   a. This gives the most consistent fixation for large tumor slices.
   b. Fixation conditions are different for different tissue/organs, so this may need to be adjusted depending on the tissue you are working with.
5. After fixation, wash with 70% ethanol twice and leave in ethanol for up to 48 hours before proceeding with paraffin embedding.

3.7 Bonus Protocol- Ultrasound-guided intracardiac injection in rats

Intracardiac injections of tumor cells into the left ventricle of the heart can be a useful way to determine whether tumor cells are capable of seeding and growing out in organs other than lungs. While intracardiac injections of tumor cells into mice have been used for this reason, mice are small rodents. When studying tumor cell clusters, using small rodent model organisms like mice may risk health risks for the animals if clusters of cells clog capillaries. For this reason, a larger rodents model like rats are safer. Here, we describe an intracardiac injection method adapted for rats.

Materials:

Equipment:

- FUJIFILM Vevo 2100 Ultrasound machine & MX250S probe
- Heating pad for animal recovery

Reagents &Supplies

- Isoflurane
- Nair (or other hair removal product)
- Applicator swab
- Gauze
- EasyTouch 27 gauge insulin syringe (Health Warehouse: EasyTouch Insulin Syringe 27 Gauge, .5cc, 1/2" - 100ct; MH827555)
- Ultrasound gel in room
- Tape
- Cells for injection, on ice
- Pipet and tips
- Water
- Extra cage for recovery

Procedure:

1. Turn on the computer and heating pad.
2. Set Image Depth to 13, focus depth to the default setting, B-mode. If necessary, press invert.

3. Angle the machine and stages so that there is room to move up, down, left, right, forward, and backwards. Probe should be fixed above the stage.
4. Touch the stage to make sure it is warming. The stage should be at around 40°C from the table, leaning towards you. This angle can/should be adjusted, but the angle is crucial to success.
5. Place animal in the isoflurane chamber wait until animal is fully anesthetized. Pipet/mix cells during this time.
6. Take animal and place on stage with the nose in the nose cone (with isoflurane). Tape animal's limbs gently to the metal pads on the stage. Do not overextend limbs as this causes the position of the heart to change; in addition, over extension of limbs can lead to nerve damage in mice.
7. Massage Nair onto mouse's chest. Wait 1 min. Wipe off with gauze, then again with gauze with water. Make sure mouse is shaven and dry before next step.
8. Apply ultrasound gel (about ¼ cup) to the animal's chest, as it will melt down quickly. Apply continuously to avoid bubbles.
9. Lower the probe onto animal's chest area. Make sure that the probe is in the right place.

    Mistake #1: probe is too close to the animal and is compressing the ribcage and heart area. Pull back.

    Mistake #2: probe must be midline.
10. Load syringe (usually for cell line, 100,000 cells in 100µl of PBS). Make sure there are no bubbles.
11. From left to right, you should see the ribcage → left ventricle → right ventricle.

12. Steady your hand by resting wrist on stage. Needle will not show up on ultrasound unless lined up exactly. Move very slightly until you can see the needle on the ultrasound.
13. Penetrate skin and heart with needle. You should see the needle in the left ventricle on the ultrasound. Inject. You can see some white “sparkles” when you are injecting into the heart.
    a. Then pull back up on the needle very slightly; if you draw back and get a little bit of blood, it probably means you were in the right place. If using Evans blue dye to practice, the mouse will become blue.
    b. If you entered the heart, you have one shot. Repeated attempts could lead to tumor in heart.
    c. If successful, mice recover quickly. If there is air embolus, mouse will die immediately.
14. Keep your needle steady after penetrating heart, until you have fully injected the cells and have pulled out.
15. Make sure you inject at a proper depth; even if the angle and location is correct, if the needle is at the incorrect depth, you may end up injecting into the heart wall rather than the left ventricle.
16. Clean off ultrasound gel from animal and allow animal to recovery in heated recovery cage.
17. Monitor animals according to your protocol.

3.8 DISCUSSION

Here, we describe detailed protocols for using rats to model breast cancer metastasis with a transplantation system. There are a number of advantages to using rat hosts rather than mouse hosts to model breast cancer dissemination. These include similarities between rat and human mammary development as well as the large amount of blood and tissues that can be collected from rats compared to mice. For example, mice are too small and have too little blood volume to efficiently study circulating tumor cells (CTCs). However, there are few rat breast cancer models, and existing models are less well characterized. For this reason, in Yamamoto et al. 2023, we xeno-transplanted mouse mammary tumor cells into the mammary fat pad of immunocompromised rat hosts and collected 10 times more CTCs than from mice[212].

However, there are many considerations necessary to adapt a mouse protocol to rat protocols. Thus, we have described detailed protocols here for using rats to model breast cancer metastasis.

We also recommend considering the following questions before switching to a rat transplantation model to study breast cancer metastasis:

1. **Will it be beneficial for you to use rats for your project?**

   As mentioned above, using a rat model will generate more tissue, blood, and CTCs than with a mouse model. However, since rats cost more than mice, especially for immunocompromised strains, it should be carefully considered whether using a rat model will save effort and cost. If the project requires large amount of tissue, blood,

CTCs or requires serial bleeds, it may be beneficial to use rats. However, if the project requires immunocompetent hosts or genetic models, rats may not be the best choice. Since rats are larger and therefore requires higher drug dose, they also may not be the best choice when performing experiments with expensive drugs.

2. **Do you have the necessary housing and equipment?**

   It is essential to make sure that the vivarium you have access to can appropriately house rats. In addition to larger cages and other housing needs, you may also need larger isoflurane chambers and nose cones.

3. **Will you have the skills necessary for the type of rat handling you need?**

   Handling mice and rats are not the same. Rats are significantly larger and stronger. Therefore, scruffing a rat for tumor measurements or IP injections requires two hands; this means you will need two handlers in order to measure tumors or perform injections. There is also an option to use rodent restraint cones (Braintree Scientific DC200), but mammary tumor measurements are difficult with this method. Larger restraints are needed for tail vein injections or the rat can be put under anesthesia as long as rats are not put under anesthesia too frequently.

4. **Is your IACUC protocol approved for this?**

   All rodent procedures and experiments must be approved by and performed in accordance to the institution-approved IACUC protocols and AAALAS guidelines and ethical regulations.

In summary, the transplantation method detailed here provides step-by-step instructions on how to perform transplantation of cells into the mammary fat pad of rats and

intracardiac injection rats. In addition, the methods here describe collection and downstream processing methods for blood and tissue. These methods are valuable to efficiently study rare events in the process of breast cancer metastasis such as tumor cell dissemination.

3.9 CHAPTER 3 FIGURES

Figure 1

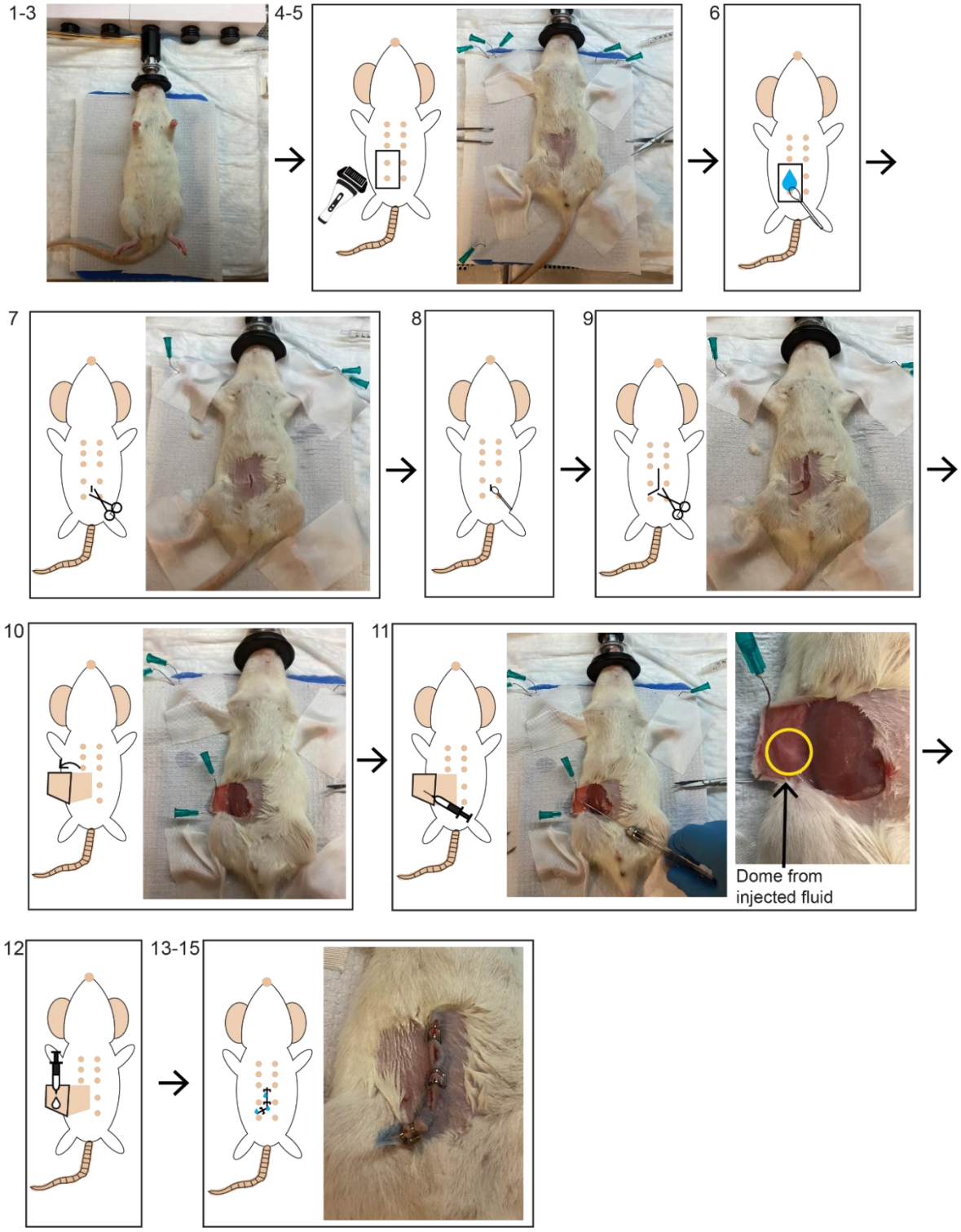

Figure 1: Orthotopic transplant protocol for rats

Figure 2

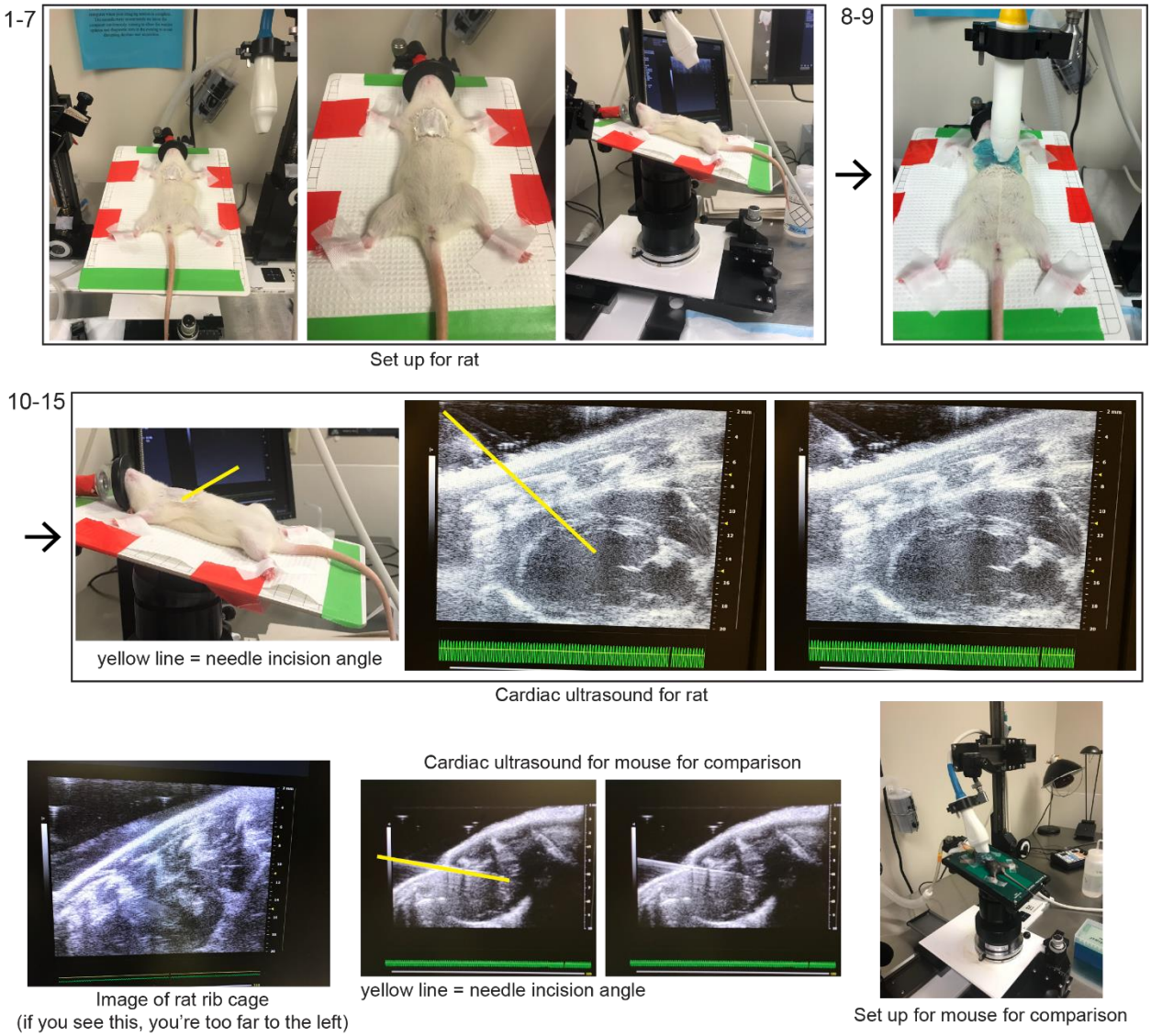

Figure 2: Intracardiac injection protocol for rats

Chapter 4. CONCLUSIONS & FUTURE DIRECTIONS

4.1 SUMMARY OF DOCTORAL WORK

Metastasis, spreading of tumor cells to other tissues, is a major cause of death for cancer patients. A key step in metastasis is the dissemination of tumor cells into systemic circulation. Therefore, a long-standing question in the field is where tumor cells disseminate from. There is abundant research on tumor cell dissemination from the tumor-stromal border, or the edges of the tumor, where tumor cells can singly or collectively invade into local tissues and blood vessels. Counterintuitively, many tumor microenvironment conditions such as hypoxia, nutrient deficiency, recruitment of immune cells, and leaky blood vessels correlated with increased metastasis and poor patient prognosis are most prevalent in the tumor core. One hypothesis that reconcile these observations is that tumor dissemination can also occur from the tumor core.

To study tumor dissemination in the context of breast cancer, I set out to collect and study circulating tumor cells (CTCs), in vivo. I soon realized that mouse models are far too small and have too little blood volume to study CTCs efficiently. However, there are very few rat breast cancer models, and existing models are less well characterized. For this reason, I developed a xenograft model where I transplanted mouse mammary tumor cells into the mammary fat pad of immunocompromised rat hosts and collected 10 times more single CTCs and CTC clusters than from mice. This new model created an unprecedented opportunity to interrogate the mechanism and dynamics of tumor cell dissemination.

The first question I asked with this model was “what is the temporal dynamics of CTC dissemination?” I discovered that tumor dissemination was temporally correlated with the emergence of necrosis in the tumor interior. These findings were corroborated by longitudinal study of CTC abundance and tissue necrosis markers in blood plasma from patients with metastatic breast cancer. Further, I observed that large, dilated blood vessels were located in the peri-necrotic regions (next to necrosis) of the tumor and that their increase was concurrent with the initiation of intratumoral necrosis and increase in CTC abundance.

Due to the large tumor size in this rat model, I was able to macrodissect the necrotic core of the tumor and separate it from the viable tumor rim. As an additional advantage of this mouse-to-rat xenograft model, we were able to computationally deconvolute mouse (tumor)-derived transcripts from rat (host stroma) derived transcripts in a bulk RNA-seq experiment. We identified angiopoietin-like 7 (Angptl7) as a tumor-specific factor localized to the peri-necrotic zone. Functional in vivo studies knocking down Angptl7 showed that Angptl7 loss normalizes central necrosis, peri-necrotic dilated vessels, metastasis, and reduces circulating tumor cell counts to nearly zero. Mechanistically, Angptl7 promotes vascular permeability and supports vascular remodeling in the peri-necrotic zone.

Taken together, I found that breast tumors actively produce factors controlling central necrosis formation and metastatic dissemination from the tumor core **(Figure 1, Graphical Abstract**). Tumor dissemination events are localized spatially to dilated peri-necrotic vessels in the tumor interior and is functionally dependent on the expression of

a factor, Angptl7, produced by peri-necrotic tumor cells. These findings from my thesis work in breast cancer models provide strong evidence that the factors in the peri-necrotic zone in the center of the tumor regulate tumor cell dissemination and suggest that tumor dissemination originates from the tumor core. My results inform a new perspective on the mechanism of tumor dissemination and reveal a potential therapeutic target to disrupt it.

4.2 GRAPHICAL RESEARCH ABSTRACT

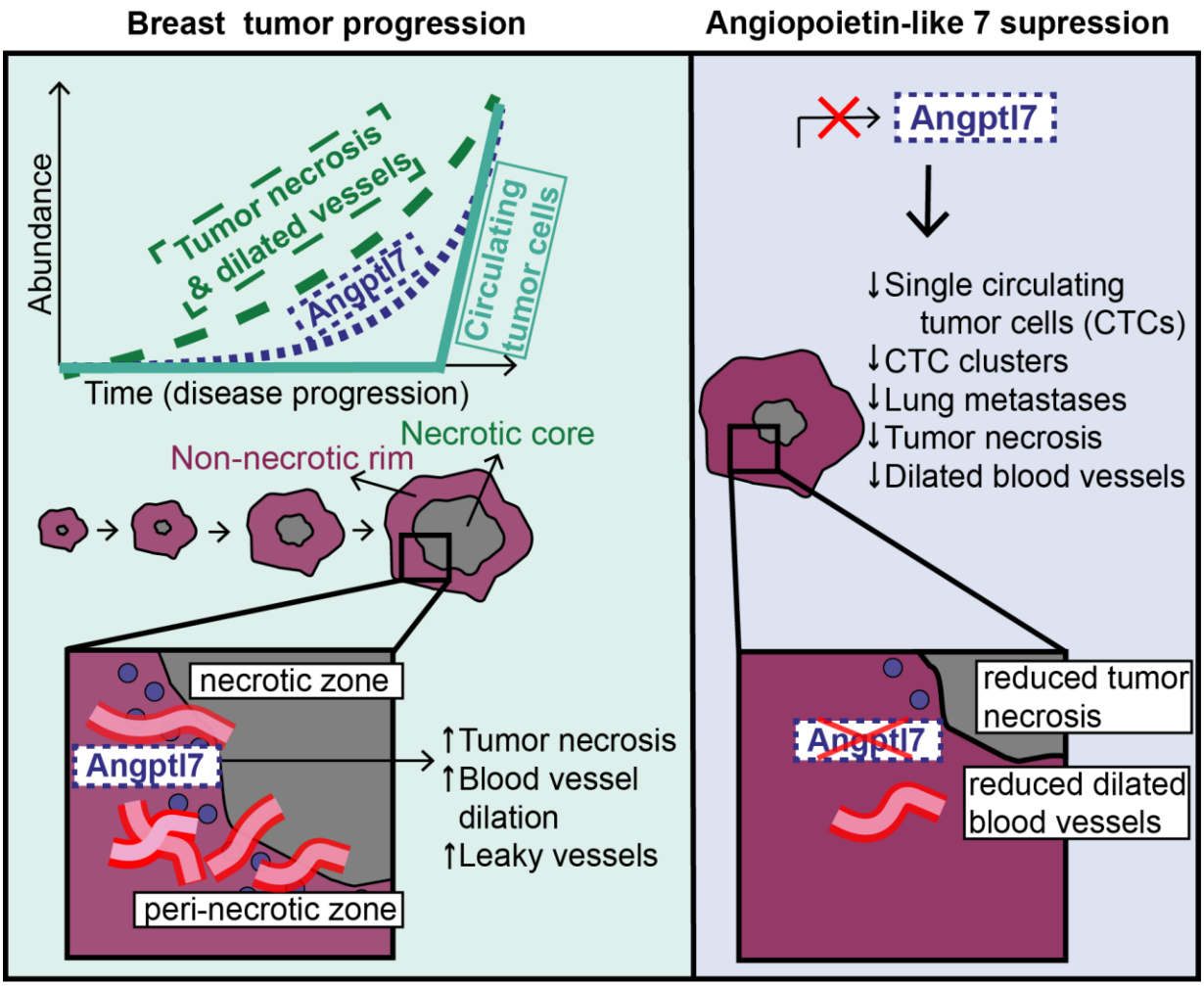

Chapter 4 Figure 1: Graphical Research Abstract

In a triple negative breast cancer model, in during normal tumor progression, circulating tumor cell (CTC) abundance increases acutely, late in disease progression. Concurrent with the increase in single CTCs and CTC clusters, central tumor necrosis, dilated blood vessels, and angiopoietin-like 7 (Angptl7) expression increases. When Angptl7 is suppressed, single CTCs, CTC clusters, lung metastases, tumor necrosis, and dilated blood vessels all dramatically decrease.

4.3 Remaining Questions and Future Directions

What induces Angptl7 expression?

In my dissertation work, I have shown that expression of a tumor-derived peri-necrotic secreted protein, Angptl7, regulates intratumoral necrosis, CTC dissemination, and metastasis. However, it is not known what induces Angptl7 expression in the first place. It is curious that Angptl7 is not highly expressed in 4T1 cells, a mouse triple negative breast cancer cell line, in vitro. In fact, Angptl7 is largely indetectable in vitro. This is true whether the cells are cultured 2D or 3D. However, when transplanted into mice or rats and tumors are allowed to grow out in vivo, peri-necrotic regions of 4T1 tumors have very high expression of Angptl7 which increases concurrently with tumor necrosis and circulating tumor cell (CTC) abundance. Therefore, it is likely that there are some features of in vivo tumors not present in in vitro culture that induce Angptl7 expression. Whether these features that induce Angptl7 expression in vivo is hypoxia, metabolic changes, tumor size, or a combination of several of these is unclear. Even outside of the context of breast cancer metastasis, what induces Angptl7 is not known. Understanding what induces and regulates the expression of Angptl7 is a critical step for using anti-Angptl7 therapy to prevent or stop breast cancer metastasis.

What is the mechanism of action of Angptl7?

Although my dissertation work has shown that Angptl7 regulates tumor necrosis and leakiness of blood vessels, there is still a need to understand a more specific mechanism of action in the context of breast cancer metastasis. Determining cognate receptors for

Angptl7 in this context and downstream mechanism of action is an important future direction of my thesis work.

Are there targetable features of metabolism in the tumor necrotic core?

Altered metabolism is one possibility of what could induce Angptl7 expression and central tumor necrosis. In addition, there could be directly targetable features of metabolism in the tumor necrotic core for treating metastatic breast cancer. Analysis of difference in metabolites in the tumor necrotic core compared to the viable rim as well as changes in metabolites over tumor progression could shed light on novel targets to treat breast cancer with large regions of necrosis.

Where do tumor cells disseminate from?

In my thesis work, I have shown that the emergence of intratumoral necrosis temporally coincides with the increase in circulating tumor cell (CTC) dissemination, peri-necrotic expression of Angptl7, and dilated blood vessels in the peri-necrotic region. I have also shown that Angptl7, a tumor-derived, peri-necrotic secreted factor regulates tumor necrosis, CTC dissemination, metastasis, and blood vessel morphology and leakiness. These data show that the tumor interior contributes to and regulates tumor cell dissemination. I have also shown that there are intravasated emboli in dilated blood vessels in the peri-necrotic region of breast tumors. However, these data are only suggestive of tumor cells disseminating from the tumor interior. Intravital imaging with mice or rats with endogenously labeled blood vessels and whole tumor imaging using

light sheet microscopy of optically cleared tumors would add great value in identifying where tumor cells disseminate from.

Do single CTCs and CTC clusters disseminate with the same mechanism?

Furthermore, our lab has always been interested in collective metastasis and the differences between collective metastasis and single cell metastasis. It remains a future direction to determine whether the mechanism and route of tumor emboli and single tumors are similar.

Can we develop a therapeutic antibody against Angptl7?

I have shown that Angptl7 is therapeutic target for patients with metastatic breast cancer. It is a major future direction of the lab to develop therapeutics antibodies against ANGPTL7. In order to do this, we have generated Angptl7 antibody candidates using hybridomas. The next step is to develop a high throughput functional screening method to identify function-blocking antibody candidates to proceed with in vivo validation.

Will combining anti-Angptl7 therapy and chemotherapy prevent metastasis?

There are many traditional chemotherapy agents such as taxol which shrink tumor size but induce tumor necrosis and metastasis. It is possible that combining anti-Angptl7 therapy with chemotherapies could shrink tumor size while preventing or reducing metastasis. A future direction is to first combine paclitaxel or other chemotherapy with shRNA suppression of Angptl7 in mice. When we identify promising anti-Angptl7 antibodies, we can them combine antibody suppression of Angptl7 with chemotherapies.

How do we stratify patients who may benefit from anti-Angptl7 therapy?

As seen in my thesis work, there are some metastatic breast cancer patient-derived xenograft (PDX) models that express high amounts of *Angptl7*, but many do not. In my studies, I found that triple negative breast cancer PDX models with high percentage of necrosis in the tumor tended to have high *Angptl7* expression. However, this data needs to be expanded further with more PDX models as well as primary patient samples. Identifying trends in Angptl7 expression in patient tumor samples and PDX models could help to identify patients who may benefit from anti-Angptl7 therapy.

Chapter 5. REFERENCES:

1. Yamamoto A, Doak AE, Cheung KJ. Orchestration of Collective Migration and Metastasis by Tumor Cell Clusters. *https://doi.org/101146/annurev-pathmechdis-031521-023557*. 2023;18(1):2022. doi:10.1146/ANNUREV-PATHMECHDIS-031521-023557
2. Wrenn E, Huang Y, Cheung K. Collective metastasis: coordinating the multicellular voyage. *Clin Exp Metastasis*. 2021;38(4):373-399. doi:10.1007/S10585-021-10111-0
3. Mittal V. Epithelial Mesenchymal Transition in Tumor Metastasis. *Annu Rev Pathol*. 2018;13:395-412. doi:10.1146/ANNUREV-PATHOL-020117-043854
4. Lambert AW, Pattabiraman DR, Weinberg RA. Emerging Biological Principles of Metastasis. *Cell*. 2017;168(4):670-691. doi:10.1016/J.CELL.2016.11.037
5. Massagué J, Ganesh K. Metastasis-Initiating Cells and Ecosystems. *Cancer Discov*. 2021;11(4):971-994. doi:10.1158/2159-8290.CD-21-0010
6. Liotta LA, Saidel MG, Kleinerman J. The significance of hematogenous tumor cell clumps in the metastatic process. *Cancer Res*. 1976;36(3):889-894. Accessed October 6, 2019. http://www.ncbi.nlm.nih.gov/pubmed/1253177
7. Fidler IJ. The relationship of embolic homogeneity, number, size and viability to the incidence of experimental metastasis. *Eur J Cancer*. 1973;9(3):223-227. doi:10.1016/S0014-2964(73)80022-2
8. Friedl P, Mayor R. Tuning Collective Cell Migration by Cell-Cell Junction Regulation. *Cold Spring Harb Perspect Biol*. 2017;9(4). doi:10.1101/CSHPERSPECT.A029199
9. Hou JM, Krebs MG, Lancashire L, et al. Clinical significance and molecular characteristics of circulating tumor cells and circulating tumor microemboli in patients with small-cell lung cancer. *J Clin Oncol*. 2012;30(5):525-532. doi:10.1200/JCO.2010.33.3716
10. Long E, Ilie M, Bence C, et al. High expression of TRF2, SOX10, and CD10 in circulating tumor microemboli detected in metastatic melanoma patients. A potential impact for the assessment of disease aggressiveness. *Cancer Med*. 2016;5(6):1022. doi:10.1002/CAM4.661
11. Wang C, Mu Z, Chervoneva I, et al. Longitudinally collected CTCs and CTC-clusters and clinical outcomes of metastatic breast cancer. *Breast Cancer Res Treat*. 2017;161(1):83-94. doi:10.1007/S10549-016-4026-2
12. Mu Z, Wang C, Ye Z, et al. Prospective assessment of the prognostic value of circulating tumor cells and their clusters in patients with advanced-stage breast cancer. *Breast Cancer Res Treat*. 2015;154(3):563-571. doi:10.1007/S10549-015-3636-4
13. Larsson AM, Jansson S, Bendahl PO, et al. Longitudinal enumeration and cluster evaluation of circulating tumor cells improve prognostication for patients with newly diagnosed metastatic breast cancer in a prospective observational trial. *Breast Cancer Res*. 2018;20(1). doi:10.1186/S13058-018-0976-0
14. Carlsson A, Kuhn P, Luttgen MS, et al. Paired High-Content Analysis of Prostate Cancer Cells in Bone Marrow and Blood Characterizes Increased Androgen

Receptor Expression in Tumor Cell Clusters. *Clin Cancer Res*. 2017;23(7):1722-1732. doi:10.1158/1078-0432.CCR-16-1355

15. Alix-Panabières C, Pantel K. Clinical Applications of Circulating Tumor Cells and Circulating Tumor DNA as Liquid Biopsy. *Cancer Discov*. 2016;6(5):479-491. doi:10.1158/2159-8290.CD-15-1483
16. de Bono JS, Scher HI, Montgomery RB, et al. Circulating tumor cells predict survival benefit from treatment in metastatic castration-resistant prostate cancer. *Clin Cancer Res*. 2008;14(19):6302-6309. doi:10.1158/1078-0432.CCR-08-0872
17. Cristofanilli M, Pierga JY, Reuben J, et al. The clinical use of circulating tumor cells (CTCs) enumeration for staging of metastatic breast cancer (MBC): International expert consensus paper. *Crit Rev Oncol Hematol*. 2019;134:39-45. doi:10.1016/J.CRITREVONC.2018.12.004
18. Jansson S, Bendahl PO, Larsson AM, Aaltonen KE, Rydén L. Prognostic impact of circulating tumor cell apoptosis and clusters in serial blood samples from patients with metastatic breast cancer in a prospective observational cohort. *BMC Cancer*. 2016;16(1). doi:10.1186/S12885-016-2406-Y
19. Paoletti C, Miao J, Dolce EM, et al. Circulating Tumor Cell Clusters in Patients with Metastatic Breast Cancer: a SWOG S0500 Translational Medicine Study. *Clin Cancer Res*. 2019;25(20):6089-6097. doi:10.1158/1078-0432.CCR-19-0208
20. Costa C, Muinelo-Romay L, Cebey-López V, et al. Analysis of a Real-World Cohort of Metastatic Breast Cancer Patients Shows Circulating Tumor Cell Clusters (CTC-clusters) as Predictors of Patient Outcomes. *Cancers (Basel)*. 2020;12(5):1111. doi:10.3390/CANCERS12051111
21. Divella R, Daniele A, Abbate I, et al. The presence of clustered circulating tumor cells (CTCs) and circulating cytokines define an aggressive phenotype in metastatic colorectal cancer. *Cancer Causes Control*. 2014;25(11):1531-1541. doi:10.1007/S10552-014-0457-4
22. Zheng L, Zou K, Yang C, Chen F, Guo T, Xiong B. Inflammation-based indexes and clinicopathologic features are strong predictive values of preoperative circulating tumor cell detection in gastric cancer patients. *Clin Transl Oncol*. 2017;19(9):1125-1132. doi:10.1007/S12094-017-1649-7
23. Lee M, Kim EJ, Cho Y, et al. Predictive value of circulating tumor cells (CTCs) captured by microfluidic device in patients with epithelial ovarian cancer. *Gynecol Oncol*. 2017;145(2):361-365. doi:10.1016/J.YGYNO.2017.02.042
24. Chang MC, Chang YT, Chen JY, et al. Clinical Significance of Circulating Tumor Microemboli as a Prognostic Marker in Patients with Pancreatic Ductal Adenocarcinoma. *Clin Chem*. 2016;62(3):505-513. doi:10.1373/CLINCHEM.2015.248260
25. Okegawa T, Ninomiya N, Masuda K, Nakamura Y, Tambo M, Nutahara K. AR-V7 in circulating tumor cells cluster as a predictive biomarker of abiraterone acetate and enzalutamide treatment in castration-resistant prostate cancer patients. *Prostate*. 2018;78(8):576-582. doi:10.1002/PROS.23501
26. Cho EH, Wendel M, Luttgen M, et al. Characterization of circulating tumor cell aggregates identified in patients with epithelial tumors. *Phys Biol*. 2012;9(1). doi:10.1088/1478-3975/9/1/016001

27. Sarioglu AF, Aceto N, Kojic N, et al. A microfluidic device for label-free, physical capture of circulating tumor cell clusters. *Nat Methods*. 2015;12(7):685-691. doi:10.1038/NMETH.3404
28. Aceto N, Bardia A, Miyamoto DT, et al. Circulating tumor cell clusters are oligoclonal precursors of breast cancer metastasis. *Cell*. 2014;158(5):1110-1122. doi:10.1016/J.CELL.2014.07.013
29. Hosokawa M, Kenmotsu H, Koh Y, et al. Size-Based Isolation of Circulating Tumor Cells in Lung Cancer Patients Using a Microcavity Array System. *PLoS One*. 2013;8(6):e67466. doi:10.1371/JOURNAL.PONE.0067466
30. Crosbie PAJ, Shah R, Krysiak P, et al. Circulating Tumor Cells Detected in the Tumor-Draining Pulmonary Vein Are Associated with Disease Recurrence after Surgical Resection of NSCLC. *J Thorac Oncol*. 2016;11(10):1793-1797. doi:10.1016/J.JTHO.2016.06.017
31. Murlidhar V, Reddy RM, Fouladdel S, et al. Poor Prognosis Indicated by Venous Circulating Tumor Cell Clusters in Early-Stage Lung Cancers. *Cancer Res*. 2017;77(18):5194-5206. doi:10.1158/0008-5472.CAN-16-2072
32. Krol I, Schwab FD, Carbone R, et al. Detection of clustered circulating tumour cells in early breast cancer. *British Journal of Cancer 2021 125:1*. 2021;125(1):23-27. doi:10.1038/s41416-021-01327-8
33. Blau CA, Ramirez AB, Blau S, et al. A Distributed Network for Intensive Longitudinal Monitoring in Metastatic Triple-Negative Breast Cancer. *J Natl Compr Canc Netw*. 2016;14(1):8-17. doi:10.6004/JNCCN.2016.0003
34. Li Z, Wu Y, Yates ME, et al. Hotspot ESR1 Mutations Are Multimodal and Contextual Modulators of Breast Cancer Metastasis. *Cancer Res*. 2022;82(7):1321-1339. doi:10.1158/0008-5472.CAN-21-2576
35. Diamantopoulou Z, Castro-Giner F, Schwab FD, et al. The metastatic spread of breast cancer accelerates during sleep. *Nature*. 2022;607(7917):156-162. doi:10.1038/S41586-022-04875-Y
36. Zeinali M, Lee M, Nadhan A, et al. High-Throughput Label-Free Isolation of Heterogeneous Circulating Tumor Cells and CTC Clusters from Non-Small-Cell Lung Cancer Patients. *Cancers (Basel)*. 2020;12(1). doi:10.3390/CANCERS12010127
37. Hamza B, Miller AB, Meier L, et al. Measuring kinetics and metastatic propensity of CTCs by blood exchange between mice. *Nat Commun*. 2021;12(1). doi:10.1038/S41467-021-25917-5
38. Gao W, Yuan H, Jing F, et al. Analysis of circulating tumor cells from lung cancer patients with multiple biomarkers using high-performance size-based microfluidic chip. *Oncotarget*. 2017;8(8):12917. doi:10.18632/ONCOTARGET.14203
39. Szczerba BM, Castro-Giner F, Vetter M, et al. Neutrophils escort circulating tumour cells to enable cell cycle progression. *Nature*. 2019;566(7745):553-557. doi:10.1038/S41586-019-0915-Y
40. Rushton AJ, Nteliopoulos G, Shaw JA, Coombes RC. A Review of Circulating Tumour Cell Enrichment Technologies. *Cancers (Basel)*. 2021;13(5):1-33. doi:10.3390/CANCERS13050970
41. Cohen EN, Jayachandran G, Hardy MR, Venkata Subramanian AM, Meng X, Reuben JM. Antigen-agnostic microfluidics-based circulating tumor cell

enrichment and downstream molecular characterization. *PLoS One*. 2020;15(10):e0241123. doi:10.1371/JOURNAL.PONE.0241123

42. Kaldjian EP, Ramirez AB, Sun Y, et al. The RareCyte® platform for next-generation analysis of circulating tumor cells. *Cytometry*. 2018;93(12):1220. doi:10.1002/CYTO.A.23619
43. Liotta LA, Kleinerman J, Saldel GM. The significance of hematogenous tumor cell clumps in the metastatic process - PubMed. Cancer Research. Published 1976. Accessed December 27, 2022. https://pubmed.ncbi.nlm.nih.gov/1253177/
44. Cheung KJ, Padmanaban V, Silvestri V, et al. Polyclonal breast cancer metastases arise from collective dissemination of keratin 14-expressing tumor cell clusters. *Proc Natl Acad Sci U S A*. 2016;113(7):E854-E863. doi:10.1073/PNAS.1508541113
45. Maddipati R, Stanger BZ. Pancreatic Cancer Metastases Harbor Evidence of Polyclonality. *Cancer Discov*. 2015;5(10):1086-1097. doi:10.1158/2159-8290.CD-15-0120
46. Zajac O, Raingeaud J, Libanje F, et al. Tumour spheres with inverted polarity drive the formation of peritoneal metastases in patients with hypermethylated colorectal carcinomas. *Nat Cell Biol*. 2018;20(3):296-306. doi:10.1038/S41556-017-0027-6
47. Allen TA, Asad D, Amu E, et al. Circulating tumor cells exit circulation while maintaining multicellularity, augmenting metastatic potential. *J Cell Sci*. 2019;132(17). doi:10.1242/JCS.231563/VIDEO-8
48. Liu X, Taftaf R, Kawaguchi M, et al. Homophilic CD44 Interactions Mediate Tumor Cell Aggregation and Polyclonal Metastasis in Patient-Derived Breast Cancer Models. *Cancer Discov*. 2019;9(1):96-113. doi:10.1158/2159-8290.CD-18-0065
49. Wrenn ED, Yamamoto A, Moore BM, et al. Regulation of Collective Metastasis by Nanolumenal Signaling. *Cell*. 2020;183(2):395-410.e19. doi:10.1016/J.CELL.2020.08.045
50. Cheung KJ, Padmanaban V, Silvestri V, et al. Polyclonal breast cancer metastases arise from collective dissemination of keratin 14-expressing tumor cell clusters. *Proceedings of the National Academy of Sciences*. Published online 2016. doi:10.1073/pnas.1508541113
51. Maddipati R, Stanger BZ. Pancreatic cancer metastases harbor evidence of polyclonality. *Cancer Discov*. 2015;5(10):1086-1097. doi:10.1158/2159-8290.CD-15-0120
52. Reeves MQ, Kandyba E, Harris S, del Rosario R, Balmain A. Multicolour lineage tracing reveals clonal dynamics of squamous carcinoma evolution from initiation to metastasis. *Nat Cell Biol*. 2018;20(6):699-709. doi:10.1038/S41556-018-0109-0
53. Echeverria G v., Powell E, Seth S, et al. High-resolution clonal mapping of multi-organ metastasis in triple negative breast cancer. *Nat Commun*. 2018;9(1). doi:10.1038/S41467-018-07406-4
54. Lo HC, Xu Z, Kim IS, et al. Resistance to natural killer cell immunosurveillance confers a selective advantage to polyclonal metastasis. *Nat Cancer*. 2020;1(7):709-722. doi:10.1038/S43018-020-0068-9

55. Berthelet J, Wimmer VC, Whitfield HJ, et al. The site of breast cancer metastases dictates their clonal composition and reversible transcriptomic profile. *Sci Adv*. 2021;7(28). doi:10.1126/SCIADV.ABF4408
56. Campbell NR, Rao A, Hunter M v., et al. Cooperation between melanoma cell states promotes metastasis through heterotypic cluster formation. *Dev Cell*. 2021;56(20):2808-2825.e10. doi:10.1016/J.DEVCEL.2021.08.018
57. Tiede S, Kalathur RKR, Lüönd F, et al. Multi-color clonal tracking reveals intra-stage proliferative heterogeneity during mammary tumor progression. *Oncogene*. 2021;40(1):12-27. doi:10.1038/S41388-020-01508-4
58. al Habyan S, Kalos C, Szymborski J, McCaffrey L. Multicellular detachment generates metastatic spheroids during intra-abdominal dissemination in epithelial ovarian cancer. *Oncogene*. 2018;37(37):5127-5135. doi:10.1038/S41388-018-0317-X
59. Kok SY, Oshima H, Takahashi K, et al. Malignant subclone drives metastasis of genetically and phenotypically heterogenous cell clusters through fibrotic niche generation. *Nature Communications 2021 12:1*. 2021;12(1):1-14. doi:10.1038/s41467-021-21160-0
60. Bhang HEC, Ruddy DA, Radhakrishna VK, et al. Studying clonal dynamics in response to cancer therapy using high-complexity barcoding. *Nature Medicine 2015 21:5*. 2015;21(5):440-448. doi:10.1038/nm.3841
61. Zafar H, Lin C, Bar-Joseph Z. Single-cell lineage tracing by integrating CRISPR-Cas9 mutations with transcriptomic data. *Nature Communications 2020 11:1*. 2020;11(1):1-14. doi:10.1038/s41467-020-16821-5
62. Follain G, Herrmann D, Harlepp S, et al. Fluids and their mechanics in tumour transit: shaping metastasis. *Nat Rev Cancer*. 2020;20(2):107-124. doi:10.1038/S41568-019-0221-X
63. Strilic B, Offermanns S. Intravascular Survival and Extravasation of Tumor Cells. *Cancer Cell*. 2017;32(3):282-293. doi:10.1016/J.CCELL.2017.07.001
64. Labuschagne CF, Cheung EC, Blagih J, Domart MC, Vousden KH. Cell Clustering Promotes a Metabolic Switch that Supports Metastatic Colonization. *Cell Metab*. 2019;30(4):720-734.e5. doi:10.1016/J.CMET.2019.07.014
65. Schafer ZT, Grassian AR, Song L, et al. Antioxidant and oncogene rescue of metabolic defects caused by loss of matrix attachment. *Nature*. 2009;461(7260):109-113. doi:10.1038/NATURE08268
66. Ubellacker JM, Tasdogan A, Ramesh V, et al. Lymph protects metastasizing melanoma cells from ferroptosis. *Nature*. 2020;585(7823):113-118. doi:10.1038/S41586-020-2623-Z
67. Brown CW, Amante JJ, Mercurio AM. Cell clustering mediated by the adhesion protein PVRL4 is necessary for α6β4 integrin-promoted ferroptosis resistance in matrix-detached cells. *J Biol Chem*. 2018;293(33):12741-12748. doi:10.1074/JBC.RA118.003017
68. Palumbo JS, Talmage KE, Massari J v., et al. Tumor cell-associated tissue factor and circulating hemostatic factors cooperate to increase metastatic potential through natural killer cell-dependent and-independent mechanisms. *Blood*. 2007;110(1):133-141. doi:10.1182/BLOOD-2007-01-065995

69. Chan IS, Ewald AJ. The changing role of natural killer cells in cancer metastasis. *J Clin Invest*. 2022;132(6). doi:10.1172/JCI143762
70. Follain G, Osmani N, Azevedo AS, et al. Hemodynamic Forces Tune the Arrest, Adhesion, and Extravasation of Circulating Tumor Cells. *Dev Cell*. 2018;45(1):33-52.e12. doi:10.1016/J.DEVCEL.2018.02.015
71. Marrella A, Fedi A, Varani G, et al. High blood flow shear stress values are associated with circulating tumor cells cluster disaggregation in a multi-channel microfluidic device. *PLoS One*. 2021;16(1):e0245536. doi:10.1371/JOURNAL.PONE.0245536
72. Li K, Wu R, Zhou M, Tong H, Luo KQ. Desmosomal proteins of DSC2 and PKP1 promote cancer cells survival and metastasis by increasing cluster formation in circulatory system. *Sci Adv*. 2021;7(40):7265-7294. doi:10.1126/SCIADV.ABG7265
73. Padmanaban V, Krol I, Suhail Y, et al. E-cadherin is required for metastasis in multiple models of breast cancer. *Nature*. 2019;573(7774):439-444. doi:10.1038/S41586-019-1526-3
74. Gkountela S, Castro-Giner F, Szczerba BM, et al. Circulating Tumor Cell Clustering Shapes DNA Methylation to Enable Metastasis Seeding. *Cell*. 2019;176(1-2):98-112.e14. doi:10.1016/J.CELL.2018.11.046
75. Huntington ND, Cursons J, Rautela J. The cancer-natural killer cell immunity cycle. *Nat Rev Cancer*. 2020;20(8):437-454. doi:10.1038/S41568-020-0272-Z
76. Dianat-Moghadam H, Mahari A, Heidarifard M, et al. NK cells-directed therapies target circulating tumor cells and metastasis. *Cancer Lett*. 2021;497:41-53. doi:10.1016/J.CANLET.2020.09.021
77. Janiszewska M, Tabassum DP, Castaño Z, et al. Subclonal cooperation drives metastasis by modulating local and systemic immune microenvironments. *Nat Cell Biol*. 2019;21(7):879-888. doi:10.1038/S41556-019-0346-X
78. Karthikeyan S, Waters IG, Dennison L, et al. Hierarchical tumor heterogeneity mediated by cell contact between distinct genetic subclones. *J Clin Invest*. 2021;131(6). doi:10.1172/JCI143557
79. Naffar-Abu Amara S, Kuiken HJ, Selfors LM, et al. Transient commensal clonal interactions can drive tumor metastasis. *Nature Communications 2020 11:1*. 2020;11(1):1-17. doi:10.1038/s41467-020-19584-1
80. Chang PH, Chen MC, Tsai YP, et al. Interplay between desmoglein2 and hypoxia controls metastasis in breast cancer. *Proc Natl Acad Sci U S A*. 2021;118(3). doi:10.1073/PNAS.2014408118
81. Ilina O, Gritsenko PG, Syga S, et al. Cell-cell adhesion and 3D matrix confinement determine jamming transitions in breast cancer invasion. *Nat Cell Biol*. 2020;22(9):1103-1115. doi:10.1038/S41556-020-0552-6
82. Pavlova NN, Pallasch C, Elia AEH, et al. A role for PVRL4-driven cell-cell interactions in tumorigenesis. *Elife*. 2013;2(2). doi:10.7554/ELIFE.00358
83. Aasen T, Mesnil M, Naus CC, Lampe PD, Laird DW. Gap junctions and cancer: communicating for 50 years. *Nat Rev Cancer*. 2016;16(12):775-788. doi:10.1038/NRC.2016.105

84. Higginbotham JN, Demory Beckler M, Gephart JD, et al. Amphiregulin exosomes increase cancer cell invasion. *Curr Biol*. 2011;21(9):779-786. doi:10.1016/J.CUB.2011.03.043
85. Roh-Johnson M, Shah AN, Stonick JA, et al. Macrophage-dependent cytoplasmic transfer during melanoma invasion in vivo. *Dev Cell*. 2017;43(5):549. doi:10.1016/J.DEVCEL.2017.11.003
86. Maeshiro M, Shinriki S, Liu R, et al. Colonization of distant organs by tumor cells generating circulating homotypic clusters adaptive to fluid shear stress. *Sci Rep*. 2021;11(1). doi:10.1038/S41598-021-85743-Z
87. Dang HX, Krasnick BA, White BS, et al. The clonal evolution of metastatic colorectal cancer. *Sci Adv*. 2020;6(24):9691-9701. doi:10.1126/SCIADV.AAY9691
88. Yu M, Bardia A, Wittner BS, et al. Circulating breast tumor cells exhibit dynamic changes in epithelial and mesenchymal composition. *Science*. 2013;339(6119):580-584. doi:10.1126/SCIENCE.1228522
89. Egeblad M, de Visser KE. Sticking together helps cancer to spread. *Nature*. 2019;566(7745):459-460. doi:10.1038/D41586-019-00341-4
90. Sprouse ML, Welte T, Boral D, et al. PMN-MDSCs Enhance CTC Metastatic Properties through Reciprocal Interactions via ROS/Notch/Nodal Signaling. *Int J Mol Sci*. 2019;20(8). doi:10.3390/IJMS20081916
91. Duda DG, Duyverman AMMJ, Kohno M, et al. Malignant cells facilitate lung metastasis by bringing their own soil. *Proc Natl Acad Sci U S A*. 2010;107(50):21677-21682. doi:10.1073/PNAS.1016234107
92. Ortiz-Otero N, Clinch AB, Hope J, Wang W, Reinhart-King CA, King MR. Cancer associated fibroblasts confer shear resistance to circulating tumor cells during prostate cancer metastatic progression. *Oncotarget*. 2020;11(12):1037-1050. doi:10.18632/ONCOTARGET.27510
93. Labelle M, Begum S, Hynes RO. Direct signaling between platelets and cancer cells induces an epithelial-mesenchymal-like transition and promotes metastasis. *Cancer Cell*. 2011;20(5):576-590. doi:10.1016/J.CCR.2011.09.009
94. Haemmerle M, Taylor ML, Gutschner T, et al. Platelets reduce anoikis and promote metastasis by activating YAP1 signaling. *Nature Communications 2017 8:1*. 2017;8(1):1-15. doi:10.1038/s41467-017-00411-z
95. Egan K, Cooke N, Kenny D. Living in shear: platelets protect cancer cells from shear induced damage. *Clin Exp Metastasis*. 2014;31(6):697-704. doi:10.1007/S10585-014-9660-7
96. Schumacher D, Strilic B, Sivaraj KK, Wettschureck N, Offermanns S. Platelet-derived nucleotides promote tumor-cell transendothelial migration and metastasis via P2Y2 receptor. *Cancer Cell*. 2013;24(1):130-137. doi:10.1016/J.CCR.2013.05.008
97. Jiang X, Wong KHK, Khankhel AH, et al. Microfluidic isolation of platelet-covered circulating tumor cells. *Lab Chip*. 2017;17(20):3498-3503. doi:10.1039/C7LC00654C
98. Katt ME, Wong AD, Searson PC. Dissemination from a Solid Tumor: Examining the Multiple Parallel Pathways. *Trends Cancer*. 2018;4(1):20-37. doi:10.1016/J.TRECAN.2017.12.002

99. Folarin AA, Konerding MA, Timonen J, Nagl S, Pedley RB. Three-dimensional analysis of tumour vascular corrosion casts using stereoimaging and micro-computed tomography. *Microvasc Res*. 2010;80(1):89-98. doi:10.1016/J.MVR.2010.03.007
100. Yang X, Zhang Y, Hosaka K, et al. VEGF-B promotes cancer metastasis through a VEGF-A-independent mechanism and serves as a marker of poor prognosis for cancer patients. *Proc Natl Acad Sci U S A*. 2015;112(22):E2900-E2909. doi:10.1073/PNAS.1503500112
101. Sugino T, Kusakabe T, Hoshi N, et al. An Invasion-Independent Pathway of Blood-Borne Metastasis : A New Murine Mammary Tumor Model. *Am J Pathol*. 2002;160(6):1973. doi:10.1016/S0002-9440(10)61147-9
102. Chang YS, di Tomaso E, McDonald DM, Jones R, Jain RK, Munn LL. Mosaic blood vessels in tumors: frequency of cancer cells in contact with flowing blood. *Proc Natl Acad Sci U S A*. 2000;97(26):14608-14613. doi:10.1073/PNAS.97.26.14608
103. Silvestri VL, Henriet E, Linville RM, Wong AD, Searson PC, Ewald AJ. A Tissue-Engineered 3D Microvessel Model Reveals the Dynamics of Mosaic Vessel Formation in Breast Cancer. *Cancer Res*. 2020;80(19):4288-4301. doi:10.1158/0008-5472.CAN-19-1564
104. Deryugina EI, Kiosses WB. Intratumoral Cancer Cell Intravasation Can Occur Independent of Invasion into the Adjacent Stroma. *Cell Rep*. 2017;19(3):601-616. doi:10.1016/J.CELREP.2017.03.064
105. Donato C, Kunz L, Castro-Giner F, et al. Hypoxia Triggers the Intravasation of Clustered Circulating Tumor Cells. *Cell Rep*. 2020;32(10). doi:10.1016/J.CELREP.2020.108105
106. Linde N, Casanova-Acebes M, Sosa MS, et al. Macrophages orchestrate breast cancer early dissemination and metastasis. *Nature Communications 2017 9:1*. 2018;9(1):1-14. doi:10.1038/s41467-017-02481-5
107. Harper KL, Sosa MS, Entenberg D, et al. Mechanism of early dissemination and metastasis in Her2+ mammary cancer. *Nature*. 2016;540(7634):588-592. doi:10.1038/NATURE20609
108. Harney AS, Arwert EN, Entenberg D, et al. Real-Time Imaging Reveals Local, Transient Vascular Permeability, and Tumor Cell Intravasation Stimulated by TIE2hi Macrophage-Derived VEGFA. *Cancer Discov*. 2015;5(9):932-943. doi:10.1158/2159-8290.CD-15-0012
109. Roh-Johnson M, Bravo-Cordero JJ, Patsialou A, et al. Macrophage contact induces RhoA GTPase signaling to trigger tumor cell intravasation. *Oncogene*. 2014;33(33):4203-4212. doi:10.1038/ONC.2013.377
110. Au SH, Storey BD, Moore JC, et al. Clusters of circulating tumor cells traverse capillary-sized vessels. *Proc Natl Acad Sci U S A*. 2016;113(18):4947-4952. doi:10.1073/PNAS.1524448113/SUPPL_FILE/PNAS.1524448113.SM17.MOV
111. Filho OM, Viale G, Stein S, et al. Impact of HER2 Heterogeneity on Treatment Response of Early-Stage HER2-Positive Breast Cancer: Phase II Neoadjuvant Clinical Trial of T-DM1 Combined with Pertuzumab. *Cancer Discov*. 2021;11(10):2474-2487. doi:10.1158/2159-8290.CD-20-1557

112. Seligson JM, Patron AM, Berger MJ, Harvey RD, Seligson ND. Sacituzumab Govitecan-hziy: An Antibody-Drug Conjugate for the Treatment of Refractory, Metastatic, Triple-Negative Breast Cancer. *Ann Pharmacother*. 2021;55(7):921-931. doi:10.1177/1060028020966548
113. Rosenberg JE, O'Donnell PH, Balar A v., et al. Pivotal Trial of Enfortumab Vedotin in Urothelial Carcinoma After Platinum and Anti-Programmed Death 1/Programmed Death Ligand 1 Therapy. *J Clin Oncol*. 2019;37(29):2592-2600. doi:10.1200/JCO.19.01140
114. Ganesh K, Massagué J. Targeting metastatic cancer. *Nature Medicine 2021 27:1*. 2021;27(1):34-44. doi:10.1038/s41591-020-01195-4
115. Kang Y, Pantel K. Tumor cell dissemination: emerging biological insights from animal models and cancer patients. *Cancer Cell*. 2013;23(5):573-581. doi:10.1016/J.CCR.2013.04.017
116. Sznurkowska MK, Aceto N. The gate to metastasis: key players in cancer cell intravasation. *FEBS J*. 2022;289(15). doi:10.1111/FEBS.16046
117. Lambert AW, Pattabiraman DR, Weinberg RA. EMERGING BIOLOGICAL PRINCIPLES OF METASTASIS. *Cell*. 2017;168(4):670. doi:10.1016/J.CELL.2016.11.037
118. Friedl P, Wolf K. Tumour-cell invasion and migration: diversity and escape mechanisms. *Nature Reviews Cancer 2003 3:5*. 2003;3(5):362-374. doi:10.1038/nrc1075
119. Carmona-Fontaine C, Deforet M, Akkari L, Thompson CB, Joyce JA, Xavier JB. Metabolic origins of spatial organization in the tumor microenvironment. *Proc Natl Acad Sci U S A*. 2017;114(11):2934-2939. doi:10.1073/PNAS.1700600114/SUPPL_FILE/PNAS.1700600114.SM02.MP4
120. Gatenby RA, Gillies RJ. A microenvironmental model of carcinogenesis. *Nature Reviews Cancer 2007 8:1*. 2008;8(1):56-61. doi:10.1038/nrc2255
121. Donato C, Kunz L, Castro-Giner F, et al. Hypoxia Triggers the Intravasation of Clustered Circulating Tumor Cells. *Cell Rep*. 2020;32(10):108105. doi:10.1016/J.CELREP.2020.108105
122. Rankin EB, Giaccia AJ. Hypoxic control of metastasis. *Science (1979)*. 2016;352(6282):175-180. doi:10.1126/SCIENCE.AAF4405/ASSET/26D7F3EF-5490-40BF-B676-1F0BB707568F/ASSETS/GRAPHIC/352_175_F3.JPEG
123. Gillies RJ, Brown JS, Anderson ARA, Gatenby RA. Eco-evolutionary causes and consequences of temporal changes in intratumoural blood flow. *Nature Reviews Cancer 2018 18:9*. 2018;18(9):576-585. doi:10.1038/s41568-018-0030-7
124. Nia HT, Munn LL, Jain RK. Physical traits of cancer. *Science (1979)*. 2020;370(6516). doi:10.1126/SCIENCE.AAZ0868/ASSET/5D0A72D9-30DE-4D81-96F5-8D7E0B0B58B2/ASSETS/GRAPHIC/370_AAZ0868_F3.JPEG
125. Chang YS, di Tomaso E, McDonald DM, Jones R, Jain RK, Munn LL. Mosaic blood vessels in tumors: Frequency of cancer cells in contact with flowing blood. *Proc Natl Acad Sci U S A*. 2000;97(26):14608. doi:10.1073/PNAS.97.26.14608
126. Katt ME, Wong AD, Searson PC. Dissemination from a Solid Tumor: Examining the Multiple Parallel Pathways. *Trends Cancer*. 2018;4(1):20-37. doi:10.1016/J.TRECAN.2017.12.002

127. Staneva R, Marjou F el, Barbazan J, et al. Cancer cells in the tumor core exhibit spatially coordinated migration patterns. *J Cell Sci*. 2019;132(6). doi:10.1242/JCS.220277/VIDEO-3
128. Deryugina EI, Kiosses WB. Intratumoral Cancer Cell Intravasation can occur Independent of Invasion into the Adjacent Stroma. *Cell Rep*. 2017;19(3):601. doi:10.1016/J.CELREP.2017.03.064
129. Fisher ER, Sass R, Fisher B. Pathologic findings from the national surgical adjuvant project for breast cancers (protocol no. 4) X. Discriminants for tenth year treatment failure. *Cancer*. 1984;53(3):712-723. doi:10.1002/1097-0142(19840201)53:3+<712::AID-CNCR2820531320>3.0.CO;2-I
130. Jimenez RE, Wallis T, Visscher DW. Centrally necrotizing carcinomas of the breast: a distinct histologic subtype with aggressive clinical behavior. *Am J Surg Pathol*. 2001;25(3):331-337. doi:10.1097/00000478-200103000-00007
131. Leek RD, Landers RJ, Harris AL, Lewis CE. Necrosis correlates with high vascular density and focal macrophage infiltration in invasive carcinoma of the breast. *Br J Cancer*. 1999;79(5-6):991. doi:10.1038/SJ.BJC.6690158
132. Bredholt G, Mannelqvist M, Stefansson IM, et al. Tumor necrosis is an important hallmark of aggressive endometrial cancer and associates with hypoxia, angiogenesis and inflammation responses. *Oncotarget*. 2015;6(37):39676-39691. doi:10.18632/ONCOTARGET.5344
133. Zhang L, Zha Z, Qu W, et al. Tumor necrosis as a prognostic variable for the clinical outcome in patients with renal cell carcinoma: A systematic review and meta-analysis. *BMC Cancer*. 2018;18(1):1-13. doi:10.1186/S12885-018-4773-Z/FIGURES/3
134. Livasy CA, Karaca G, Nanda R, et al. Phenotypic evaluation of the basal-like subtype of invasive breast carcinoma. *Mod Pathol*. 2006;19(2):264-271. doi:10.1038/MODPATHOL.3800528
135. Foulkes WD, Smith IE, Reis-Filho JS. Triple-Negative Breast Cancer. *https://doi.org/101056/NEJMra1001389*. 2010;363(20):1938-1948. doi:10.1056/NEJMRA1001389
136. Lee G, Yoon S, Ahn B, Kim HR, Jang SJ, Hwang HS. Blood Vessel Invasion Predicts Postoperative Survival Outcomes and Systemic Recurrence Regardless of Location or Blood Vessel Type in Patients with Lung Adenocarcinoma. *Ann Surg Oncol*. 2021;28(12):7279-7290. doi:10.1245/S10434-021-10122-X/TABLES/4
137. Engellau J, Bendahl PO, Persson A, et al. Improved prognostication in soft tissue sarcoma: independent information from vascular invasion, necrosis, growth pattern, and immunostaining using whole-tumor sections and tissue microarrays. *Hum Pathol*. 2005;36(9):994-1002. doi:10.1016/J.HUMPATH.2005.07.008
138. Mohammed RAA, Martin SG, Mahmmod AM, et al. Objective assessment of lymphatic and blood vascular invasion in lymph node-negative breast carcinoma: findings from a large case series with long-term follow-up. *J Pathol*. 2011;223(3):358-365. doi:10.1002/PATH.2810
139. Nitta H, Allard MA, Sebagh M, et al. Prognostic Value and Prediction of Extratumoral Microvascular Invasion for Hepatocellular Carcinoma. *Ann Surg Oncol*. 2019;26(8):2568-2576. doi:10.1245/S10434-019-07365-0/FIGURES/2

140. Zhao Y, Fu X, Lopez JI, et al. Selection of metastasis competent subclones in the tumour interior. *Nat Ecol Evol*. 2021;5(7):1033. doi:10.1038/S41559-021-01456-6
141. Osmani N, Goetz JG. Multiscale Imaging of Metastasis in Zebrafish. *Trends Cancer*. 2019;5(12):766-778. doi:10.1016/J.TRECAN.2019.10.003
142. Karreman MA, Mercier L, Schieber NL, et al. Fast and precise targeting of single tumor cells in vivo by multimodal correlative microscopy. *J Cell Sci*. 2016;129(2):444-456. doi:10.1242/JCS.181842/-/DC1
143. Wyckoff JB, Wang Y, Lin EY, et al. Direct Visualization of Macrophage-Assisted Tumor Cell Intravasation in Mammary Tumors. *Cancer Res*. 2007;67(6):2649-2656. doi:10.1158/0008-5472.CAN-06-1823
144. Roh-Johnson M, Bravo-Cordero JJ, Patsialou A, et al. Macrophage contact induces RhoA GTPase signaling to trigger tumor cell intravasation. *Oncogene*. 2014;33(33):4203. doi:10.1038/ONC.2013.377
145. Campbell NR, Rao A, Hunter M v., et al. Cooperation between melanoma cell states promotes metastasis through heterotypic cluster formation. *Dev Cell*. 2021;56(20):2808-2825.e10. doi:10.1016/J.DEVCEL.2021.08.018
146. Hamza B, Miller AB, Meier L, et al. Measuring kinetics and metastatic propensity of CTCs by blood exchange between mice. *Nat Commun*. 2021;12(1). doi:10.1038/S41467-021-25917-5
147. Noto FK, Sangodkar J, Adedeji BT, et al. The SRG rat, a Sprague-Dawley Rag2/Il2rg double-knockout validated for human tumor oncology studies. *PLoS One*. 2020;15(10):e0240169. doi:10.1371/JOURNAL.PONE.0240169
148. Morisada T, Kubota Y, Urano T, Suda T, Oike Y. Angiopoietins and Angiopoietin-Like Proteins in Angiogenesis. *http://dx.doi.org.offcampus.lib.washington.edu/101080/10623320600697989*. 2009;13(2):71-79. doi:10.1080/10623320600697989
149. Dewey FE, Gusarova V, Dunbar RL, et al. Genetic and Pharmacologic Inactivation of ANGPTL3 and Cardiovascular Disease. *New England Journal of Medicine*. 2017;377(3):211-221. doi:10.1056/NEJMOA1612790/SUPPL_FILE/NEJMOA1612790_DISCLOSURES.PDF
150. Graham MJ, Lee RG, Brandt TA, et al. Cardiovascular and Metabolic Effects of ANGPTL3 Antisense Oligonucleotides . *New England Journal of Medicine*. 2017;377(3):222-232. doi:10.1056/NEJMOA1701329/SUPPL_FILE/NEJMOA1701329_DISCLOSURES.PDF
151. Gur-Cohen S, Yang H, Baksh SC, et al. Stem cell-driven lymphatic remodeling coordinates tissue regeneration. *Science (1979)*. 2019;366(6470):1218-1225. doi:10.1126/SCIENCE.AAY4509/SUPPL_FILE/AAY4509S9.MP4
152. Zhu P, Tan MJ, Huang RL, et al. Angiopoietin-like 4 Protein Elevates the Prosurvival Intracellular O2−:H2O2 Ratio and Confers Anoikis Resistance to Tumors. *Cancer Cell*. 2011;19(3):401-415. doi:10.1016/J.CCR.2011.01.018
153. Santulli G. Angiopoietin-Like Proteins: A Comprehensive Look. *Front Endocrinol (Lausanne)*. 2014;5(JAN). doi:10.3389/FENDO.2014.00004

154. Padua D, Zhang XHF, Wang Q, et al. TGFβ Primes Breast Tumors for Lung Metastasis Seeding through Angiopoietin-like 4. *Cell*. 2008;133(1):66-77. doi:10.1016/J.CELL.2008.01.046
155. Zhang CC, Kaba M, Ge G, et al. Angiopoietin-like proteins stimulate ex vivo expansion of hematopoietic stem cells. *Nature Medicine 2006 12:2*. 2006;12(2):240-245. doi:10.1038/nm1342
156. Kuchtey J, Källberg ME, Gelatt KN, Rinkoski T, Komàromy AM, Kuchtey RW. Angiopoietin-like 7 Secretion Is Induced by Glaucoma Stimuli and Its Concentration Is Elevated in Glaucomatous Aqueous Humor. *Invest Ophthalmol Vis Sci*. 2008;49(8):3438. doi:10.1167/IOVS.07-1347
157. Tanigawa Y, Wainberg M, Karjalainen J, et al. Rare protein-altering variants in ANGPTL7 lower intraocular pressure and protect against glaucoma. *PLoS Genet*. 2020;16(5):e1008682. doi:10.1371/JOURNAL.PGEN.1008682
158. Peek R, Kammerer RA, Frank S, Otte-Höller I, Westphal JR. The Angiopoietin-like Factor Cornea-derived Transcript 6 Is a Putative Morphogen for Human Cornea. *Journal of Biological Chemistry*. 2002;277(1):686-693. doi:10.1074/JBC.M105746200
159. Toyono T, Usui T, Yokoo S, et al. Angiopoietin-like 7 is an anti-angiogenic protein required to prevent vascularization of the cornea. *PLoS One*. 2015;10(1). doi:10.1371/JOURNAL.PONE.0116838
160. Praveen K, Patel GC, Gurski L, et al. ANGPTL7, a therapeutic target for increased intraocular pressure and glaucoma. *Communications Biology 2022 5:1*. 2022;5(1):1-15. doi:10.1038/s42003-022-03932-6
161. Carmeliet P, Jain RK. Angiogenesis in cancer and other diseases. *Nature 2000 407:6801*. 2000;407(6801):249-257. doi:10.1038/35025220
162. Tavora B, Mederer T, Wessel KJ, et al. Tumoural activation of TLR3–SLIT2 axis in endothelium drives metastasis. *Nature 2020 586:7828*. 2020;586(7828):299-304. doi:10.1038/s41586-020-2774-y
163. de Martino M, Hoetzenecker K, Ankersmit HJ, et al. Serum 20S proteasome is elevated in patients with renal cell carcinoma and associated with poor prognosis. *British Journal of Cancer 2012 106:5*. 2012;106(5):904-908. doi:10.1038/bjc.2012.20
164. Lavabre-Bertrand T, Henry L, Carillo S, et al. Plasma Proteasome Level Is a Potential Marker in Patients with Solid Tumors and Hemopoietic Malignancies. Published online 2001. doi:10.1002/1097-0142
165. Lyssiotis CA, Kimmelman AC. Metabolic Interactions in the Tumor Microenvironment. *Trends Cell Biol*. 2017;27(11):863-875. doi:10.1016/J.TCB.2017.06.003
166. Thomlinson RH. Hypoxia and tumours. *J Clin Pathol Suppl (R Coll Pathol)*. 1977;11(S3-11):105. doi:10.1136/JCP.S3-11.1.105
167. Beerling E, Seinstra D, de Wit E, et al. Plasticity between Epithelial and Mesenchymal States Unlinks EMT from Metastasis-Enhancing Stem Cell Capacity. *Cell Rep*. 2016;14(10):2281-2288. doi:10.1016/J.CELREP.2016.02.034
168. Harney AS, Arwert EN, Entenberg D, et al. Real-Time Imaging Reveals Local, Transient Vascular Permeability, and Tumor Cell Intravasation Stimulated by

TIE2hi Macrophage-Derived VEGFA. *Cancer Discov*. 2015;5(9):932-943. doi:10.1158/2159-8290.CD-15-0012
169. Silvestri VL, Henriet E, Linville RM, Wong AD, Searson PC, Ewald AJ. A Tissue-Engineered 3D Microvessel Model Reveals the Dynamics of Mosaic Vessel Formation in Breast Cancer. *Cancer Res*. 2020;80(19):4288-4301. doi:10.1158/0008-5472.CAN-19-1564
170. Wagenblast E, Soto M, Gutiérrez-Ángel S, et al. A model of breast cancer heterogeneity reveals vascular mimicry as a driver of metastasis. *Nature 2015 520:7547*. 2015;520(7547):358-362. doi:10.1038/nature14403
171. Maniotis AJ, Folberg R, Hess A, et al. Vascular channel formation by human melanoma cells in vivo and in vitro: vasculogenic mimicry. *Am J Pathol*. 1999;155(3):739-752. doi:10.1016/S0002-9440(10)65173-5
172. Cheung KJ, Gabrielson E, Werb Z, Ewald AJ. Collective invasion in breast cancer requires a conserved basal epithelial program. *Cell*. 2013;155(7):1639-1651. doi:10.1016/J.CELL.2013.11.029
173. Cheung KJ, Padmanaban V, Silvestri V, et al. Polyclonal breast cancer metastases arise from collective dissemination of keratin 14-expressing tumor cell clusters. *Proc Natl Acad Sci U S A*. 2016;113(7):E854-E863. doi:10.1073/PNAS.1508541113
174. Gkountela S, Castro-Giner F, Szczerba BM, et al. Circulating Tumor Cell Clustering Shapes DNA Methylation to Enable Metastasis Seeding. *Cell*. 2019;176(1-2):98-112.e14. doi:10.1016/j.cell.2018.11.046
175. Liu X, Taftaf R, Kawaguchi M, et al. Homophilic CD44 Interactions Mediate Tumor Cell Aggregation and Polyclonal Metastasis in Patient-Derived Breast Cancer Models. *Cancer Discov*. 2019;9(1):96-113. doi:10.1158/2159-8290.CD-18-0065
176. Bakker GJ, Weischer S, Ortas JF, et al. Intravital deep-tumor single-beam 3-photon, 4-photon, and harmonic microscopy. *Elife*. 2022;11. doi:10.7554/ELIFE.63776
177. Scheele CLGJ, Herrmann D, Yamashita E, et al. Multiphoton intravital microscopy of rodents. *Nature Reviews Methods Primers 2022 2:1*. 2022;2(1):1-26. doi:10.1038/s43586-022-00168-w
178. Gaggioli C, Hooper S, Hidalgo-Carcedo C, et al. Fibroblast-led collective invasion of carcinoma cells with differing roles for RhoGTPases in leading and following cells. *Nat Cell Biol*. 2007;9(12):1392-1400. doi:10.1038/NCB1658
179. Wrenn ED, Yamamoto A, Moore BM, et al. Regulation of Collective Metastasis by Nanolumenal Signaling. *Cell*. 2020;183(2):395. doi:10.1016/J.CELL.2020.08.045
180. Hu Z, Curtis C. Looking backward in time to define the chronology of metastasis. *Nature Communications 2020 11:1*. 2020;11(1):1-4. doi:10.1038/s41467-020-16995-y
181. Klein CA. Cancer progression and the invisible phase of metastatic colonization. *Nat Rev Cancer*. 2020;20(11):681-694. doi:10.1038/S41568-020-00300-6
182. Heimann R, Hellman S. Clinical progression of breast cancer malignant behavior: what to expect and when to expect it. *J Clin Oncol*. 2000;18(3):591-599. doi:10.1200/JCO.2000.18.3.591

183. Minn AJ, Gupta GP, Padua D, et al. Lung metastasis genes couple breast tumor size and metastatic spread. *Proc Natl Acad Sci U S A*. 2007;104(16):6740. doi:10.1073/PNAS.0701138104
184. Narod SA, Iqbal J, Giannakeas V, Sopik V, Sun P. Breast Cancer Mortality After a Diagnosis of Ductal Carcinoma In Situ. *JAMA Oncol*. 2015;1(7):888-896. doi:10.1001/JAMAONCOL.2015.2510
185. Carbone C, Piro G, Merz V, et al. Angiopoietin-Like Proteins in Angiogenesis, Inflammation and Cancer. *Int J Mol Sci*. 2018;19(2). doi:10.3390/IJMS19020431
186. Kaldjian EP, Ramirez AB, Sun Y, et al. The RareCyte® platform for next-generation analysis of circulating tumor cells. *Cytometry*. 2018;93(12):1220. doi:10.1002/CYTO.A.23619
187. Wingrove E, Liu ZZ, Patel KD, Kluger HM, Chiang VL, Nguyen Correspondence DX. Transcriptomic Hallmarks of Tumor Plasticity and Stromal Interactions in Brain Metastasis. *Cell Rep*. 2019;27. doi:10.1016/j.celrep.2019.03.085
188. Liao Y, Smyth GK, Shi W. featureCounts: an efficient general purpose program for assigning sequence reads to genomic features. *Bioinformatics*. 2014;30(7):923-930. doi:10.1093/BIOINFORMATICS/BTT656
189. Ritchie ME, Phipson B, Wu D, et al. limma powers differential expression analyses for RNA-sequencing and microarray studies. *Nucleic Acids Res*. 2015;43(7):e47-e47. doi:10.1093/NAR/GKV007
190. Robinson MD, McCarthy DJ, Smyth GK. edgeR: a Bioconductor package for differential expression analysis of digital gene expression data. *Bioinformatics*. 2010;26(1):139-140. doi:10.1093/BIOINFORMATICS/BTP616
191. Smyth GK, Ritchie ME, Law CW, et al. RNA-seq analysis is easy as 1-2-3 with limma, Glimma and edgeR. *F1000Research 2018 5:1408*. 2018;5:1408. doi:10.12688/f1000research.9005.3
192. Law CW, Chen Y, Shi W, Smyth GK. Voom: Precision weights unlock linear model analysis tools for RNA-seq read counts. *Genome Biol*. 2014;15(2):1-17. doi:10.1186/GB-2014-15-2-R29/FIGURES/11
193. Subramanian A, Tamayo P, Mootha VK, et al. Gene set enrichment analysis: A knowledge-based approach for interpreting genome-wide expression profiles. *Proc Natl Acad Sci U S A*. 2005;102(43):15545-15550. doi:10.1073/PNAS.0506580102/SUPPL_FILE/06580FIG7.JPG
194. Oziolor E, Arat S, Martin M. Annotation depth confounds direct comparison of gene expression across species. *BMC Bioinformatics*. 2021;22(1):1-15. doi:10.1186/S12859-021-04414-Y/FIGURES/7
195. Bankhead P, Loughrey MB, Fernández JA, et al. QuPath: Open source software for digital pathology image analysis. *Sci Rep*. 2017;7(1). doi:10.1038/S41598-017-17204-5
196. Schindelin J, Arganda-Carreras I, Frise E, et al. Fiji: an open-source platform for biological-image analysis. *Nature Methods 2012 9:7*. 2012;9(7):676-682. doi:10.1038/nmeth.2019
197. Zhou Y, Zhou B, Pache L, et al. Metascape provides a biologist-oriented resource for the analysis of systems-level datasets. *Nature Communications 2019 10:1*. 2019;10(1):1-10. doi:10.1038/s41467-019-09234-6

198. Dobin A, Davis CA, Schlesinger F, et al. STAR: ultrafast universal RNA-seq aligner. *Bioinformatics*. 2013;29(1):15-21. doi:10.1093/BIOINFORMATICS/BTS635
199. Durinck S, Spellman PT, Birney E, Huber W. Mapping Identifiers for the Integration of Genomic Datasets with the R/Bioconductor package biomaRt. *Nat Protoc*. 2009;4(8):1184. doi:10.1038/NPROT.2009.97
200. Liao Y, Smyth GK, Shi W. The R package Rsubread is easier, faster, cheaper and better for alignment and quantification of RNA sequencing reads. *Nucleic Acids Res*. 2019;47(8):e47. doi:10.1093/NAR/GKZ114
201. Danecek P, Bonfield JK, Liddle J, et al. Twelve years of SAMtools and BCFtools. *Gigascience*. 2021;10(2):1-4. doi:10.1093/GIGASCIENCE/GIAB008
202. Guy CT, Cardiff RD, Muller WJ. Induction of mammary tumors by expression of polyomavirus middle T oncogene: a transgenic mouse model for metastatic disease. *Mol Cell Biol*. 1992;12(3):954-961. doi:10.1128/MCB.12.3.954-961.1992
203. Attalla S, Taifour T, Bui T, Muller W. Insights from transgenic mouse models of PyMT-induced breast cancer: recapitulating human breast cancer progression in vivo. *Oncogene 2020 40:3*. 2020;40(3):475-491. doi:10.1038/s41388-020-01560-0
204. Sflomos G, Schipper K, Koorman T, et al. Atlas of Lobular Breast Cancer Models: Challenges and Strategic Directions. *Cancers (Basel)*. 2021;13(21). doi:10.3390/CANCERS13215396
205. Grasset EM, Dunworth M, Sharma G, et al. Triple-negative breast cancer metastasis involves complex epithelial-mesenchymal transition dynamics and requires vimentin. *Sci Transl Med*. 2022;14(656). doi:10.1126/SCITRANSLMED.ABN7571
206. Deryugina EI, Kiosses WB. Intratumoral Cancer Cell Intravasation Can Occur Independent of Invasion into the Adjacent Stroma. *Cell Rep*. 2017;19(3):601-616. doi:10.1016/J.CELREP.2017.03.064
207. Osmani N, Goetz JG. Multiscale Imaging of Metastasis in Zebrafish. *Trends Cancer*. 2019;5(12):766-778. doi:10.1016/J.TRECAN.2019.10.003
208. Karreman MA, Mercier L, Schieber NL, et al. Fast and precise targeting of single tumor cells in vivo by multimodal correlative microscopy. *J Cell Sci*. 2016;129(2):444-456. doi:10.1242/JCS.181842
209. Roh-Johnson M, Bravo-Cordero JJ, Patsialou A, et al. Macrophage contact induces RhoA GTPase signaling to trigger tumor cell intravasation. *Oncogene*. 2014;33(33):4203-4212. doi:10.1038/ONC.2013.377
210. Campbell NR, Rao A, Hunter M v., et al. Cooperation between melanoma cell states promotes metastasis through heterotypic cluster formation. *Dev Cell*. 2021;56(20):2808-2825.e10. doi:10.1016/J.DEVCEL.2021.08.018
211. Hamza B, Miller AB, Meier L, et al. Measuring kinetics and metastatic propensity of CTCs by blood exchange between mice. *Nature Communications 2021 12:1*. 2021;12(1):1-11. doi:10.1038/s41467-021-25917-5
212. Yamamoto A, Huang Y, Krajina BA, et al. Metastasis from the tumor interior and necrotic core formation are regulated by breast cancer-derived angiopoietin-like 7. *Proceedings of the National Academy of Sciences*. 2023;120(10):e2214888120. doi:10.1073/PNAS.2214888120

213. Treuting PM, Dintzis SM, Montine KS. Comparative anatomy and histology : a mouse, rat and human atlas. :552.
214. Bu W, Li Y. Intraductal Injection of Lentivirus Vectors for Stably Introducing Genes into Rat Mammary Epithelial Cells in Vivo. *J Mammary Gland Biol Neoplasia*. 2020;25(4):389-396. doi:10.1007/S10911-020-09469-W
215. Souto EP, Dobrolecki LE, Villanueva H, Sikora AG, Lewis MT. In Vivo Modeling of Human Breast Cancer Using Cell Line and Patient-Derived Xenografts. *Journal of Mammary Gland Biology and Neoplasia 2022 27:2*. 2022;27(2):211-230. doi:10.1007/S10911-022-09520-Y
216. Noto FK, Sangodkar J, Adedeji BT, et al. The SRG rat, a Sprague-Dawley Rag2/Il2rg double-knockout validated for human tumor oncology studies. *PLoS One*. 2020;15(10):e0240169. doi:10.1371/JOURNAL.PONE.0240169
217. Cheung KJ, Gabrielson E, Werb Z, Ewald AJ. Collective invasion in breast cancer requires a conserved basal epithelial program. *Cell*. 2013;155(7):1639-1651. doi:10.1016/J.CELL.2013.11.029

CURRICULUM VITAE

Ami Yamamoto

Education

2017-CURRENT
Ph.D. in Molecular & Cellular Biology (MCB) • University of Washington, Seattle
GPA 3.87

MAY 2015
B.S. in Genetics, Cell Biology & Development • Summa Cum Laude • University of Minnesota, Twin Cities
GPA 3.72

Research Experience

2017-CURRENT
PhD Candidate- University of Washington, Molecular & Cellular Biology (MCB) Program
Fred Hutchinson Cancer Research Center- Public Health Sciences Division
Adviser: Kevin Cheung (PI)
Project: Peri-necrotic proteins regulate circulating tumor cell dissemination and metastasis

- Developed a rat transplantation model to more efficiently study circulating tumor cells in breast cancer
- Applied mouse to rat xenograft model for RNA-seq deconvolution, differentiating transcripts derived by tumor vs host stroma.
- Revealed necrosis in the primary tumor & peri-necrotic Angptl7 expression as regulators of circulating tumor cell dissemination, tumor metastasis, and dilated blood vessels.
- Identified a Angptl7 as a therapeutic target to suppress breast cancer metastasis
- Set up high throughput antibody screening to identify Angptl7 antibodies with robust functional effect
- Mentored several technicians and students

2015-2017
Lab Technician
University of Minnesota, Twin Cities
Adviser: Rita Perlingeiro (PI)

- Contributed to 6 publications advancing the field of pluripotent stem cell therapies for muscular dystrophy

2012-2015
Undergraduate Research Assistant
University of Minnesota, Twin Cities
Adviser: Melissa Gardner (PI)
- Utilized TIRF microscopy to study the effects of plus-end binding protein Bim1 on microtubule dynamic and successful cell division, contributing as second author in a Current Biology publication.
- Applied molecular biology techniques to study the microtubule lumen entry for the α-tubulin acetyltransferase enzyme, contributing as second author for a PNAS publication.

2013
Lupus Foundation of Minnesota Fellow
University of Minnesota, Twin Cities
Adviser: Erik Peterson (PI)
- Applied cellular biology, molecular biology, and immunology techniques to study the immunological effects of the LypW variant of PTPn22 for SLE (systemic lupus erythematosus) patients, contributing to a publication.

Other Work Experience

2022-CURRENT
Commercialization Intern
Life Science Washington Institute (LSWI)
- Assist in the development, execution, and management of programs, services, and events supporting life science entrepreneurs & start-ups via educational, economic, and other resources crucial for their success.
- Assisted the WIN Mentoring Program, ensuring high-quality mentorship of 26 early-stage entrepreneurs.
- Assisted with Venture Investment & Partnering (VIP) Forums, bringing investors & strategic partners (eg: MERCK, BMS, Otsuka) to Seattle and connecting partners with Washington-based companies.
- Performed analysis and assembled the 2022 WA Life Science Investor Report.

Publications

Yamamoto A, Huang Y, Krajina BA, McBirney M, Doak AE, Qu S, Wang CL, Haffner MC, Cheung KJ. Metastasis from the tumor interior and necrotic core formation are regulated by breast cancer-derived angiopoietin-like 7. *PNAS*, 120(10), e2214888120. https://doi.org/10.1073/pnas.2214888120

Yamamoto A, Doak AE, Cheung KJ. Orchestration of Collective Migration and Metastasis by Tumor Cell Clusters. (2023). Annu Rev Pathol, 18:231-256. doi: https://doi.org/10.1146/annurev-pathmechdis-031521-023557

Wrenn ED, **Yamamoto A**, Moore BM, Huang Y, McBirney M, Thomas AJ, Greenwood E, Rabena YF, Rahbar H, Partridge SC, & Cheung KJ. (2020). Regulation of Collective Metastasis by Nanolumenal Signaling. Cell, 183(2), 395–410.e19. https://doi.org/10.1016/j.cell.2020.08.045

Incitti T, Magli A, Jenkins A, Lin K, **Yamamoto A**, Perlingeiro RCR. (2020). Pluripotent stem cell-derived skeletal muscle fibers preferentially express myosin heavy-chain isoforms associated with slow and oxidative muscles. Skeletal muscle, 10(1), 17. https://doi.org/10.1186/s13395-020-00234-5

Mondragon-Gonzalez R, Azzag K, Selvaraj S, **Yamamoto A**, Perlingeiro RCR. (2019). Transplantation studies reveal internuclear transfer of toxic RNA in engrafted muscles of myotonic dystrophy 1 mice. EBioMedicine, 47, 553–562. https://doi.org/10.1016/j.ebiom.2019.08.031

Incitti T, Magli A, Jenkins A, Lin K, **Yamamoto A**, Perlingeiro RCR. (2020). Pluripotent stem cell-derived skeletal muscle fibers preferentially express myosin heavy-chain isoforms associated with slow and oxidative muscles. Skeletal muscle, 10(1), 17. https://doi.org/10.1186/s13395-020-00234-5

Kim J, Oliveira VKP, **Yamamoto A**, Perlingeiro RCR. (2017). Generation of skeletal myogenic progenitors from human pluripotent stem cells using non-viral delivery of minicircle DNA. Stem cell research, 23, 87–94. https://doi.org/10.1016/j.scr.2017.07.013

Magli A, Incitti T, Kiley J, Swanson SA, Darabi R, Rinaldi F, Selvaraj S, **Yamamoto A**, Tolar J, Yuan C, Stewart R, Thomson JA, Perlingeiro RCR. (2017). PAX7 Targets, CD54, Integrin α9β1, and SDC2, Allow Isolation of Human ESC/iPSC-Derived Myogenic Progenitors. Cell reports, 19(13), 2867–2877. https://doi.org/10.1016/j.celrep.2017.06.005

Dourado KMC, Baik J, Oliveira VKP, Beltrame M, **Yamamoto A**, Theuer CP, Figueiredo CAV, Verneris MR, Perlingeiro RCR. (2017). Endoglin: a novel target for therapeutic intervention in acute leukemias revealed in xenograft mouse models. Blood, 129(18), 2526–2536. https://doi.org/10.1182/blood-2017-01-763581

Coombes CE, **Yamamoto A**, McClellan M, Reid TA, Plooster M, Luxton GW, Alper J, Howard J & Gardner MK. Mechanism of microtubule lumen entry for the α-tubulin acetyltransferase enzyme αTAT1. (2016). Mechanism of microtubule lumen entry for the α-tubulin acetyltransferase enzyme αTAT1. Proceedings of the National Academy of Sciences of the United States of America, 113(46), E7176–E7184. https://doi.org/10.1073/pnas.1605397113

Wang Y, Ewart D, **Yamamoto A**, Baechler EC, Fazeli P, & Peterson EJ. (2015). PTPN22 Variant R620W Is Associated With Reduced Toll-like Receptor 7-Induced Type I Interferon in Systemic Lupus Erythematosus. Arthritis & rheumatology (Hoboken, N.J.), 67(9), 2403–2414. https://doi.org/10.1002/art.39211

Coombes CE, **Yamamoto A,** Kenzie MR, Odde DJ, & Gardner MK. Evolving tip structures can explain age-dependent microtubule catastrophe. (2013). Current biology:CB, 23(14), 1342–1348. https://doi.org/10.1016/j.cub.2013.05.059

Select Leadership & Diversity, Equity & Inclusion Experience

Hutch United Co-chair & Outreach Chair (Fred Hutchinson Cancer Center) (2018-Current)

- Planned and executed 20+ networking, mentoring, career panel, panel discussion, social, and informational events to promote the success and well-being of historically excluded or underrepresented scientists at Fred Hutch.
- Liaison for the Seattle Central College Math, Engineering, Science Achievement (MESA) Program
- Lead organizer for annual STEM Paths Innovation Network (SPIN) Girls (King County program for girls of color 8-10th grade to explore STEM careers) visit to Fred Hutch

Lead lab-wide Diversity, Equity & Inclusion (DEI) Journal club (2020-current)

- Initiated, planned, facilitated, and championed DEI journal club for the Cheung Lab every 2 months during lab meeting.

Cellular & Molecular Biology Training Grant Retreat Planning Committee Lead (2019-2020)

- Organized the annual retreat including student presentations, keynote, and alumni career panel. Coordinated the shift from in-person to virtual retreat in light of the pandemic, taking advantage of the virtual format to invite non-local alumni for the career panel.

MCB Steering Committee Elected Student Representative (2018-2020)

- Elected student representative in the MCB steering committee attended by MCB directors, former directors, department heads of affiliated programs, and MCB staff.

MCB recruitment leader (2018-2021)

- Organize MCB recruitment. Significant organization, delegation, leadership, and communication skills are required.

MCB Crosslinker co-founder & co-director (2017-2019)

- Student-led, professional networking opportunity for graduate students, post-docs, and faculty. Organized opportunities for trainees to receive mentorship from faculty outside of their field.

Funding

Ruth L. Kirschstein National Research Service Award (NRSA) Individual Predoctoral Fellowship (F31) (1F31CA260932-01A1) (March 2022-Current)

Cellular and Molecular Biology Training Grant (T32 GM007270) (Sept 2018-Sept 2020)

Selected Technical Skills

Preclinical/in vivo models (mouse & rat) • 2D cell culture • 3D organoid culture • Tumor organoid systems • Immunofluorescence • Immunohistochemistry • Confocal microscopy • Western blotting • qPCR • Image analysis (IMARIS, ImageJ, QuPath) • Basic histology • Assay development

---

Other Skills & Competencies

Excellent communication skills • Attention to detail • Project management • Scientific communication • Leadership • Team player • Strong time management skills • Ability to learn skills quickly • Mentorship • Public Speaking • Scientific presentations • Scientific communication (with non-scientists) • Educational outreach • Multitasking • Problem solving • Translational research • Breast cancer • Cancer metastasis • Facilitation of diversity, equity, and inclusion conversations • Native-level Japanese